Exploration of Radiative Thermal Transport at the Nanoscale Using High-Resolution Calorimetry

by

Dakotah Thompson

A dissertation submitted in partial fulfillment
of the requirements for the degree of
Doctor of Philosophy
(Mechanical Engineering)
in the University of Michigan
2018

Doctoral Committee:

Professor Edgar Meyhofer, Co-Chair
Professor Pramod Sangi Reddy, Co-Chair
Associate Professor Vikram Gavini
Professor John Schotland

Dakotah Thompson

dakotaht@umich.edu

ORCID iD: 0000-0002-1779-5669

Dedication

To Mom and Dad.

Acknowledgements

I feel like I have had the ideal PhD experience in a lot of ways, and the two people who made that happen for me are my co-advisors Pramod Reddy and Edgar Meyhofer. Edgar, I will always be inspired by your bookshelf and the amount of knowledge you have been able to acquire over a lifetime. It seems like some people can actually know "a lot about a lot". Pramod, I was drawn to your group back in 2012 because your intelligence and your kindness were so apparent, and it has been a pleasure learning from you over the years. I have learned so much about nanofabrication, experimentation, and physics during my PhD because you both expected a lot out of me and pushed me to be better. You also fought hard for me when the initial reviews came back less than positive, and have served as great career mentors. In the end, I know that you care a lot about this research and about me as a person too. And for that, I just want to say thank you.

I also owe so much to the collaborators in my lab, who were instrumental to all of the work I was ever a part of. I'd first like to acknowledge Seid Sadat, who taught me nanofabrication and how to perform experiments. Thank you for being my mentor Seid, and I hope I didn't give you too much of a headache during my first years in the group! I also have to thank Bai Song, who performed the experiments in Ch. 2. Bai, you were a great collaborator and were very generous with me with regards to authorship, so thank you! I am also deeply indebted to Linxiao Zhu, who performed the computations in Ch. 3 and 4. Linxiao, without you I truly would not have been able to publish. You were such a great collaborator who also taught me a lot about electromagnetism and computation. I'd also like to thank my labmates Kyeongtae Kim,

Wonho Jeong, Woochul Lee, Yashar Ganjeh, Longji Cui, Rohith Mittapally, Ruijiao Miao, and Kun Wang, who all directly collaborated with me at some point or other. Finally, I have to especially thank my labmate Anthony Fiorino. Anthony, you were my closest collaborator and went through every step of the PhD process with me. Thanks for your hard work and for all of the laughs!

I am also grateful to many people not in my lab who nonetheless contributed to my success as a graduate student. To start, the staff members at the Lurie Nanofabrication Facility have been a huge help to me over the years. I'd like to especially thank Pilar Herrera-Fierro, Nadine Wang, Brian Armstrong, Terre Briggs, Matt Oonk, Tony Sebastian, and Tom Latowski – it was a pleasure working with you. I also want to show appreciation for my committee members, Professor Vikram Gavini and Professor John Schotland, whose questions during my dissertation proposal exam forced me to think more deeply. Finally, I want to extend a big thanks to Professor Juan Carlos Cuevas and Victor Fernandez-Hurtado for their helpful discussions of near-field heat transfer, as well as their specific contributions to the extreme near-field work and sphere-plate work, which are not presented in this dissertation.

I've loved living in Ann Arbor for the past six years, and there are so many good people I have gotten to know here that have made the experience special. Johanna and Jenna – you were my original friends here and I'll always appreciate you. John, Justin, Alex, Yev, Joel, Narayanan, Chuky, Tony, Alek, Dave, Kyle, Ilya – I'm so happy that I got to know you and thank you for all the fun times!

Finally, I have to thank a few people that were supporting me long before I first drove up to Ann Arbor. To Professor Baratunde Cola – you taught me heat transfer when I was an undergraduate student at Georgia Tech and then gave me the opportunity to do research. Thank

you for being such a great mentor and friend! To Blake and Matt – thank you for the long phone conversations and book recommendations. To my brother and sister, Tyler and Sierra – thank you for all the adventures and I can't wait for the new ones yet to come. To my mom and dad, Carol and John – thank you for your love, which fills me with light and warmth.

Table of Contents

List of Figures

List of Appendices

Abstract

Understanding radiative thermal transport is vitally important in a host of scientific fields, from climate science to astrophysics, and is critical for enabling technological advances in energy conversion and thermal management. However, the fundamental framework we use today to describe thermal radiation and radiative heat transfer (RHT), developed over a century ago by Max Planck, is not generally correct and may break down completely at the nanoscale. Despite the importance of understanding the limits of Planck's laws, there has been a dearth of experimental studies exploring radiative thermal transport at sub-micron and nanometer length scales, primarily due to numerous technical challenges. This dissertation summarizes detailed experimental work, enabled by picowatt-resolution, resistance thermometry-based calorimetry, that probes anomalous radiative thermal transport that arises due to two distinct nanoscale size effects.

The first size effect manifests when the gap between the surfaces of bodies exchanging thermal radiation is significantly smaller than the peak thermal wavelength (~10 μm at room temperature). Longstanding predictions based on the framework of fluctuational electrodynamics (FED) have suggested that RHT in this 'near-field' regime can exceed Planck's blackbody limit by orders-of-magnitude due to the presence of evanescent surface waves, though measurements validating these predictions have remained elusive. In Ch. 2, I present experimental work that quantitatively measures the radiative thermal conductance between two parallel plates as the gap

separation between them is systematically varied from 10 μm to <100 nm, revealing 100- fold enhancements in RHT at the smallest gaps.

The second size effect manifests when the physical dimensions of the bodies exchanging thermal radiation are smaller than the peak thermal wavelength. As opposed to the 'near-field' effect described above, this previously unidentified size effect can lead to enhancements of RHT above the blackbody limit when the bodies are in the 'far-field'. In Ch. 3, I present experimental work that probes the far-field RHT between two coplanar nano-membranes with sub-wavelength thickness, demonstrating that Planck's blackbody limit can be exceeded even in the far-field by more than two orders of magnitude. These observations were found to agree well with state-of-the-art calculations based on the FED framework.

Based on these insights, I present in Ch. 4 a novel scheme to actively gate the radiative heat current between two nanostructures in the far-field via evanescent interactions with a third structure in close proximity. Such a gating scheme is completely unexpected based on a naïve understanding of Planck's laws, and may bear upon the design of infrared spectroscopy tools as well as thermal absorbers for energy conversion applications.

In aggregate, this dissertation addresses a few key scientific and technical questions: To what extent can Planck's blackbody limit be exceeded at the nanoscale? How can sub-micron and nanometer length scales be practically accessed to verify FED predictions? In what ways can the nanoscale size effects discussed above be leveraged to achieve unprecedented control of thermal radiation and radiative thermal transport? Further, the calorimetric techniques developed in this dissertation will enable detailed examinations of interesting phenomena in radiative thermal transport that remain unexplored.

Chapter 1 Exploring Nanoscale Radiative Thermal Transport with High-Resolution Calorimetry

1.1 Introduction to Planck's Law of Thermal Radiation

It has been known since the 1800s that a body at a finite temperature emits electromagnetic radiation with an intensity that depends considerably on the temperature of the body [1-4]. Early attempts to describe the nature of this thermal radiation relied on analyzing the "blackbody", an ideal body for which the intensity of the thermal radiation it emits depends *only* on its temperature, which can be closely approximated by a hollow cavity where radiation can escape from the cavity through a small hole [5]. Accurately modelling the spectral intensity of blackbody radiation thus requires finding the electromagnetic energy density within the hollow cavity, which begins by solving Maxwell's equations for the electric and magnetic fields that are in thermal equilibrium with the walls of the cavity. An appropriate choice of boundary conditions as well as the use of Fourier analysis for the vector potential greatly simplifies the problem, revealing that the radiation field in the cavity behaves like a collection of simple harmonic oscillators, which are referred to historically as "radiation oscillators". The energy of the radiation field in a narrow frequency range can then be simply given by Eq. (1-1):

$$U(\nu)d\nu = \bar{E}\delta N \tag{1-1}$$

where $U(\nu)d\nu$ is the energy in the frequency range between ν and $\nu + d\nu$, δN is the number of radiation oscillators in that frequency range, and $\bar{E}$ is the mean energy possessed by the oscillators. Despite the apparent simplicity of this expression, early attempts to solve Eq. (1-1)

for the spectral energy density within the cavity using classical statistical mechanics to derive $\bar{E}$ produced a model that completely failed to explain empirical observations [5].

In 1901, Max Planck amended the above treatment by assuming that the energy of each radiation oscillator was quantized, not only leading to a model that exactly fit empirical observations, but also establishing the field of quantum mechanics [6, 7]. Planck's expression for the energy density within the cavity, today known as Planck's law, is given by Eq. (1-2):

$$u(\nu) = U(\nu)/V = \frac{8\pi}{c^3}\frac{h\nu^3}{\exp(h\nu/k_B T)-1} \tag{1-2}$$

where h is the universal Planck constant, k_B is the Boltzmann constant, T is the absolute temperature, c is the speed of light in vacuum, and V is the volume of the cavity. In addition to describing the spectral intensity of thermal radiation emitted from an ideal blackbody at equilibrium, given by $I_{BB}(\nu) = u(\nu)\times c/4\pi$, Planck's law accurately captures the characteristically incoherent nature of thermal radiation from any hot body, which is known empirically to be spectrally broadband, unpolarized, and diffusely propagating in all directions from its surface [8]. After plotting I_{BB}, shown in Figure 1-1 as a function of wavelength, it is also clear that the blackbody spectrum is peaked at a characteristic wavelength λ_{Th} that depends on the temperature T as $\lambda_{Th}T = 2898\mu m\cdot K$, which is consistent with earlier predictions of Gustav Wien [8]. Further, starting from Planck's law, and using concepts from ray optics, one can derive the Stefan-Boltzmann law which gives the total radiative heat transfer (RHT) between blackbodies [8], which is presented succinctly for two blackbodies in Eq. (1-3):

$$Q_{1-2} = A_1 F_{1-2}\sigma(T_1^4 - T_2^4) \tag{1-3}$$

where the subscripts *1* and *2* correspond to body *1* and *2* respectively, A is the surface area of the body, T is the temperature of the body, σ is the Stephan-Boltzmann constant, and F is a

geometric view factor accounting for the fraction of radiation emitted by body *1* that is incident on body *2*. Together, Planck's law and the Stefan-Boltzmann law represent two fundamental limits: the spectral intensity of radiation emitted from any real surface cannot exceed the blackbody spectrum, and, as a direct consequence, the Stefan-Boltzmann law represents the maximum total radiative heat transfer between any bodies at different temperatures.

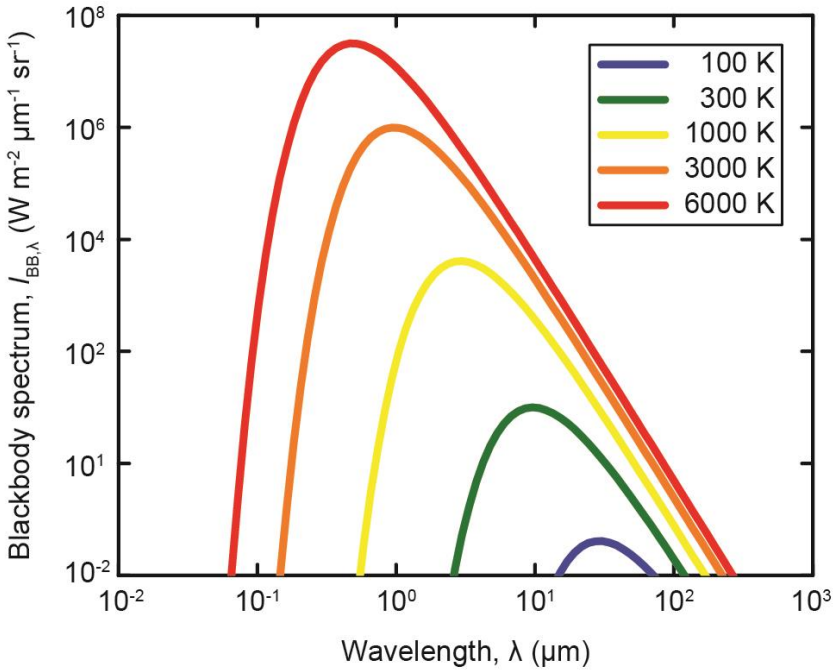

Figure 1-1. Spectral intensity of thermal radiation emitted from a blackbody at five different temperatures. Note that, for ambient temperature ~300 K, the blackbody spectrum is peaked at a wavelength ~10 μm.

However, Planck's law is not without its limitations, which can be understood by revisiting Eq. (1-1). Typical derivations of δN in Eq. (1-1) assume that the hollow cavity is very large, allowing many electromagnetic waves with a given frequency to fit inside [5]. As a result of this assumption, the number of radiation oscillators in reciprocal space can be represented by a continuous density function. Planck himself uses this same assumption, which he acknowledges in his book on the subject [9]:

We are therefore obliged to introduce right at the start a certain restriction with respect to the size of the parts of space to be considered. Throughout the following discussion it will be assumed that the linear dimensions of all parts of space considered, as well as the radii of curvature of all surfaces under consideration, are large compared with the wave lengths of the rays considered…To sum up: We distinguish once for all between two kinds of lengths of entirely different orders of magnitude – dimensions of bodies and wave lengths.

To summarize, Planck's law operates under the assumption that 1) The size of the bodies, and 2) the distance between bodies is large compared to the characteristic wavelength of thermal radiation λ_{Th}, which is ~10 μm at room temperature. If either of these assumptions is violated, then Planck's law and the Stefan-Boltzmann law are no longer valid. Because both of these assumptions were considered to be well-founded in typical engineering applications and in everyday experience for most of the 20th century, Planck's law became the de facto framework for understanding radiative thermal transport.

1.2 Development and Predictions of Fluctuational Electrodynamics

In the 1950s, Sergei Rytov developed an alternative framework termed fluctuational electrodynamics (FED) to describe thermal radiation [10, 11]. As described in a subsequent adaptation by Polder and Van Hove [12], this FED framework models the electromagnetic energy flux from a body by solving for the macroscopic Maxwell's equations that include thermally fluctuating microcurrents in the body as source terms responsible for the thermal radiation. The correlation of these thermally induced current sources $j_\alpha(\vec{r},\omega)$ is related to the local temperature T and dielectric function of the material comprising the body $\varepsilon(\vec{r},\omega)=\varepsilon'(\vec{r},\omega)+i\varepsilon''(\vec{r},\omega)$ through the fluctuation dissipation theorem (FDT) [13, 14] as shown in Eq. (1-4):

$$\left\langle j_\alpha^*(\vec{r},\omega)\, j_\beta(\vec{r},\omega)\right\rangle = \frac{4}{\pi}\omega\Theta(\omega,T)\delta(\vec{r}-\vec{r}\,')\delta(\omega-\omega')\varepsilon''(\vec{r},\omega)\delta_{\alpha\beta} \tag{1-4}$$

where $\vec{r}$ denotes the spatial position, α and β denote different spatial directions, and $\Theta(\omega,T)$ specifies the mean thermal energy for a given mode with frequency ω, which is presented in Eq. (1-5) below:

$$\Theta(\omega,T) = \frac{\hbar\omega}{\exp(\hbar\omega / k_B T) - 1} \tag{1-5}$$

Here $\hbar$ is the reduced Planck constant and k_B is the Boltzmann constant. As indicated by the Dirac delta $\delta(\vec{r}-\vec{r}\,')$ in Eq. (1-5), the original treatment of FED assumes only that the fluctuating currents are spatially independent. Such an assumption is valid as long as the mean free path (mfp) of charge carriers in the body is sufficiently smaller than the wavelengths of the electromagnetic fields, and that all relevant spatial dimensions of the system are much larger than this mean free path as well. This assumption of a small mfp is indeed valid for most materials, as the mfp of free electrons in even the most conducting metals is typically below 50 nm [15].

When comparing the derivation of Planck's law to the derivation of FED for describing thermal radiation, it becomes clear that FED is more general. Planck's law can only be considered valid for modelling systems that are spatially much larger than λ_{Th} (~10 µm at room temperature), limiting the size of the systems that can be accurately modelled to the sub-mm range and above. In contrast, FED appears to be valid for modelling systems that are even in the sub-micron and nanometer regime, so long as the lateral dimensions of the system are large compared to the relevant mean free paths of charge carriers.

Although the advanced numerical methods [16-18] that would be required to fully implement FED were lacking during the time of its development, it was found in the decades that

followed that thermal radiation and radiative heat transfer for systems with simple geometries could be described analytically using FED [12, 19-21]. Notably, FED was implemented to investigate the radiative heat transfer between two parallel, planar semi-infinite bodies separated by a vacuum gap smaller than λ_{Th} [12]. This analysis was prompted in part by observations of unexpectedly poor insulating performance of multifoil radiation shields at cryogenic temperatures, which were used in space applications [22-24]. In this 'near-field' regime, evanescent modes supported at the surfaces of bodies were found to tunnel across the miniscule gap separating the bodies, resulting in a dramatic enhancement in the radiative heat flux compared to the blackbody limit that depends strongly on the gap separation [25]. In fact, orders-of-magnitude enhancements in RHT between two planar surfaces, above the Stefan-Boltzmann limit, were predicted for gaps less than 100 nm at room temperature [26, 27]. This near-field radiative heat transfer (NFRHT) was also found to be polarized and spectrally coherent due to the coupling of resonant surface modes like surface phonon polaritons or surface plasmon polaritons, which are supported in polar dielectrics and metals, respectively [27-30].

Additionally, it was found that FED could be used to model, in a straightforward way, the spectral emissive power from small spheres with diameters comparable to or smaller λ_{Th}. In agreement with predictions of the Mie theory concerned with the scattering from small spheres [31], FED predicted that the emissive power of a sub-wavelength sphere into free-space can, in principle, exceed the blackbody limit for a particular wavelength [32]. Following the advent of advanced computational techniques, FED was used to model the thermal emission from small bodies with more complex geometries, with predictions of enhanced coherency of thermal emission and absorption [33-35]. As one example, it was predicted from FED and observed

experimentally that the thermal emission from thin wires with sub-wavelength diameters can be highly polarized [36].

Together, the ‘near-field’ effect, where gap separations between bodies are less than the peak thermal wavelength, and the ‘small-body’ effect, where the physical dimensions of a body are smaller than the peak thermal wavelength, represent two distinct size effects where Planck’s law is violated at the nanoscale. Two broad and interrelated trends have piqued the general interest in these nanoscale size effects in recent decades. The first trend being that computational resources have advanced considerably since the 1950s, so that today FED can be used to model nanoscale thermal radiation and heat transfer in a range of complex geometrical and material systems. The second trend is that nanotechnology as a whole has developed, so that nanometer/sub-micron devices and materials are now routinely used in a range of scientific fields and for numerous technological applications.

The potential to tailor the properties of nanoscale radiative thermal transport by leveraging these nanoscale size effects, especially the near-field effect, has been rigorously investigated in recent years. Dramatic enhancements in NFRHT between polar dielectrics, within a narrow spectral band, is one tantalizing theoretical prediction [37]. More recently, it has been shown computationally that additional enhancement and spectral tuning of NFRHT can be achieved through the design of novel structures and materials (nanostructured surfaces [38-41], thin-films [42, 43], 2D materials [44-47], phase change materials [48-50]), as well as by actively applying electric and magnetic fields [51-55]. These novel predictions have stimulated many proposals for technological development. Energy conversion [56-59] (especially near-field enhanced thermophotovoltaic (TPV) energy conversion [44, 47, 60-70]), modulation and rectification of heat flow [71-79], heat assisted magnetic recording (HAMR) [80-82], and high-

resolution nanolithography [83-88] are all applications that can be enabled or improved with NFRHT.

1.3 Quantifying Heat Flow at the Micro and Nanoscale

These interesting theoretical predictions and proposals have largely defied experimental validation for decades due to the lack of the appropriate experimental tools. Quantitatively measuring heat flows at these small length scales requires the use of a heat flow calorimeter with high sensitivity, since the thermal signals to be measured generally scale with the physical size of the system under study.

A conceptual schematic of a heat flow calorimeter is shown in Figure 1-2. The calorimeter device itself can be modelled, using a simple lumped parameter model, as a structure that is coupled to the surrounding environment by a weak thermal link with thermal conductance G_{Th}. An unknown heat input to the calorimeter Q_{Th} produces a corresponding temperature change ΔT of the device. If G_{Th} is well characterized and an appropriate sensor exists to detect temperature changes, the heat input to the calorimeter is quantified from Eq. (1-6):

$$Q_{Th} = G_{Th} \times \Delta T \tag{1-6}$$

Based on this equation, designing a calorimeter with excellent heat flow resolution requires a low thermal conductance G_{Th} and very sensitive thermometry. The development of heat flow calorimeters with extremely low G_{Th} has benefited greatly from the advent of microfabrication technology. Typically, these microfabricated calorimeters are comprised of a thin-film structure made from a dielectric that is suspended by long support beams that are affixed to a silicon substrate. Placement of this structure in a high-vacuum environment eliminates conduction

through air, and thermal conductances less than 100 nW K^{-1} have been achieved at room temperature [89-95].

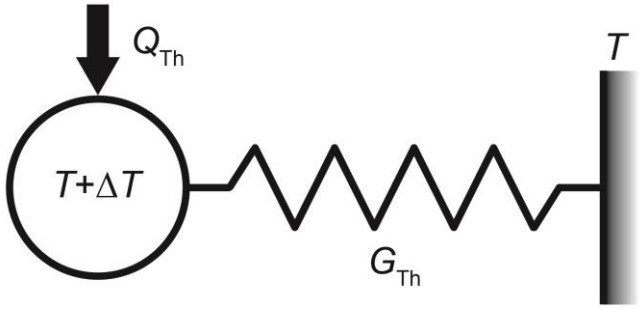

Figure 1-2. Schematic of a heat flow calorimeter. The calorimeter structure, modelled as a lumped thermal mass, is thermally isolated from the surrounding environment at temperature T. The degree of thermal isolation is characterized by the thermal conductance G_{Th}. A heat input Q_{Th} to the calorimeter produces a temperature rise ΔT.

A resistance thermometer, a sensor comprised of a material whose electrical resistance changes with temperature, can be integrated into these suspended structures to sensitively detect temperature changes. Platinum, whose resistance R changes linearly with temperature T over a wide range, has a temperature coefficient of resistance (TCR) ~2×10^{-3} K^{-1} at room temperature, where $TCR = (dR/dT)\times R^{-1}$. Such a platinum resistance thermometer (PRT) has been used recently to detect modulated temperature changes with a resolution of ~30 μK at room temperature using a phase locked-loop scheme [93, 96, 97]. By integrating a PRT (temperature resolution ~ 30 μK) into the suspended structure described above (thermal conductance ~100 nW K^{-1}), a resistance thermometry-based heat flow calorimeter with single-digit picowatt resolution can be fabricated. Because of its high sensitivity and ease of use for nanoscale thermal transport studies, I rely heavily on this tool to undertake the experimental work detailed in this dissertation.

1.4 Structure of This Dissertation

The fluctuational electrodynamics formalism has predicted anomalous radiative thermal transport in nanoscale systems that violates the predictions of Planck's law. However, these interesting predictions have yet to be rigorously explored, and there remains a host of questions in the field of nanoscale radiative thermal transport that have yet to be answered. The overarching questions I hope to address in this dissertation are summarized below:

1) To what extent can Planck's blackbody limit be exceeded at the nanoscale?
2) Can the sub-micron and nanometer length scales actually be accessed experimentally, in order to verify predictions from FED and to demonstrate novel technological applications?
3) How can the two nanoscale size effects described above, 'near-field' and 'small-body' effect, be specifically leveraged in order to achieve unprecedented control of thermal radiation and radiative heat transfer?

The following chapters detail my efforts over the past six years of graduate school to address some of these questions. Some chapters have been adapted from peer-reviewed and published manuscripts, reformatted so as to be visually consistent throughout this document.

In Chapter 2 [98], I present an experimental approach to probe NFRHT between parallel, planar surfaces. Prior to this work, efforts to probe NFRHT across nanoscale gaps relied on tip-plate or sphere-plate geometries, which, though less challenging to realize experimentally, provided data that was more difficult to compare with theory and did not allow huge enhancements in RHT to be observed. This work represents the first ever measurement of NFRHT between parallel plates separated by gaps less than 100 nm, illustrating that RHT can exceed the blackbody limit by two orders-of-magnitude.

In Chapter 3 [99], I experimentally quantify the far-field radiative heat transfer (FFRHT) between structures with sub-wavelength dimensions. Despite the fundamental importance, there were no prior works examining RHT between nanostructures separated by large distances. This work provides the first ever evidence that FFRHT can exceed the blackbody limit, even by orders-of-magnitude depending on the specific shape and dimensions of the nanostructures.

In Chapter 4 [100], I demonstrate a novel scheme to actively gate the radiative heat current between two sub wavelength-sized structures in the far-field via the mutual interaction with a third structure that is evanescently coupled to the first two. This study reveals that heat currents can be gated by over an order-of-magnitude using this scheme, which is unexpected based on a naïve understanding of Planck's law. The insights from this work can inform the design of high-speed thermal modulation schemes, and have important ramifications for the design of thermal absorbers and emitters used in energy harvesting applications

In Chapter 5, I provide an overview of this research work and discuss some interesting directions I believe that this field of study can take. I also discuss some ongoing work that I was unable to finish during my PhD, but which I nonetheless hope to continue due to the potential importance for novel technological and scientific advancements.

Chapter 2 Radiative Heat Conductances between Dielectric and Metallic Plates with Nanoscale Gaps

Reproduced with permission from reference [98]:

Bai Song*, Dakotah Thompson*, Anthony Fiorino, Yashar Ganjeh, Pramod Reddy and Edgar Meyhofer, *Nature Nanotechnology* 11, 509-514, (2016).

2.1 Abstract

Recent experiments [30, 42, 101, 102] have demonstrated that radiative heat transfer between objects separated by nanometre-scale gaps considerably exceeds the predictions of far-field radiation theories [9]. Exploiting this near-field enhancement is of great interest for emerging technologies such as near-field thermophotovoltaics and nano-lithography [25, 37, 63, 64, 67, 68, 103, 104] because of the expected increases in efficiency, power conversion or resolution in these applications [25, 67]. Past measurements, however, were performed using tip-plate or sphere-plate configurations and failed to realize the orders of magnitude increases in radiative heat currents predicted from near-field radiative heat transfer theory [12, 37]. Here, we report 100- to 1,000-fold enhancements (at room temperature) in the radiative conductance between parallel-planar surfaces at gap sizes below 100 nm, in agreement with the predictions of near-field theories [12, 37]. Our measurements were performed in vacuum gaps between prototypical materials (SiO_2–SiO_2, Au–Au, SiO_2–Au and Au–Si) using two microdevices and a custom-built nanopositioning platform [105], which allows precise control

over a broad range of gap sizes (from <100 nm to 10 μm). Our experimental set-up will enable systematic studies of a variety of near-field-based thermal phenomena [53, 71, 77], with important implications for thermophotovoltaic applications [46, 67, 69], that have been predicted but have defied experimental verification.

2.2 Introduction

Experimentally probing nanoscale radiative heat transfer between parallel planes is essential for achieving dramatic enhancements in radiative heat currents (or equivalently large conductances) and for studying nanoscale heat radiation from novel materials and device structures [46, 53, 67, 69, 71, 77]. Previous experimental efforts [106-108] have been limited to gaps of ~1 μm and in one case [109] to ~400 nm, and reported few-fold enhancements in radiative conductances, limited by angular alignment difficulties, surface curvatures and particulate contaminations. More recently, an experiment [110] using ~500-nm-thick nanobeams also obtained similar enhancements in conductance compared to the far-field.

2.3 Experiments, Results and Analysis

To enable direct, systematic measurements of radiative heat currents between two parallel-planar surfaces separated by a nanoscale vacuum gap we fabricated Si-based microdevices that feature thermally isolated flat regions with characteristic dimensions of ~48 μm and are coated with a desired dielectric (SiO_2) or metal (Au). Figure 2-1a, b presents scanning electron microscope (SEM) images of these novel devices, which are called the receiver and emitter, respectively. The emitter device (Figure 2-1b) features a 20-μm-tall, 48 μm × 48 μm Si mesa fabricated via a high-aspect-ratio etching process. The elevation of the mesa ensures that only its top surface (emitter active area, false-coloured in Figure 2-1b) forms nanoscale gaps with the receiver, while the rest of the device remains in the far-field.

Both devices feature integrated resistance heater-thermometers that enable us to heat the emitter and measure temperature changes in the receiver. Characterization via atomic force microscopy (Figure 2-1e, f) and dark-field optical microscopy (Figure 2-1d) confirmed that the devices are extremely flat and free of large particles, a critical condition for performing the desired nanoscale radiative heat transfer measurements in parallel-planar devices. The largest deviation from planarity is seen in the receiver device, which is ~30 nm over a 40 μm × 40 μm region (Figure 2-1f). Further particles, if any, were <40 nm in diameter on both devices.

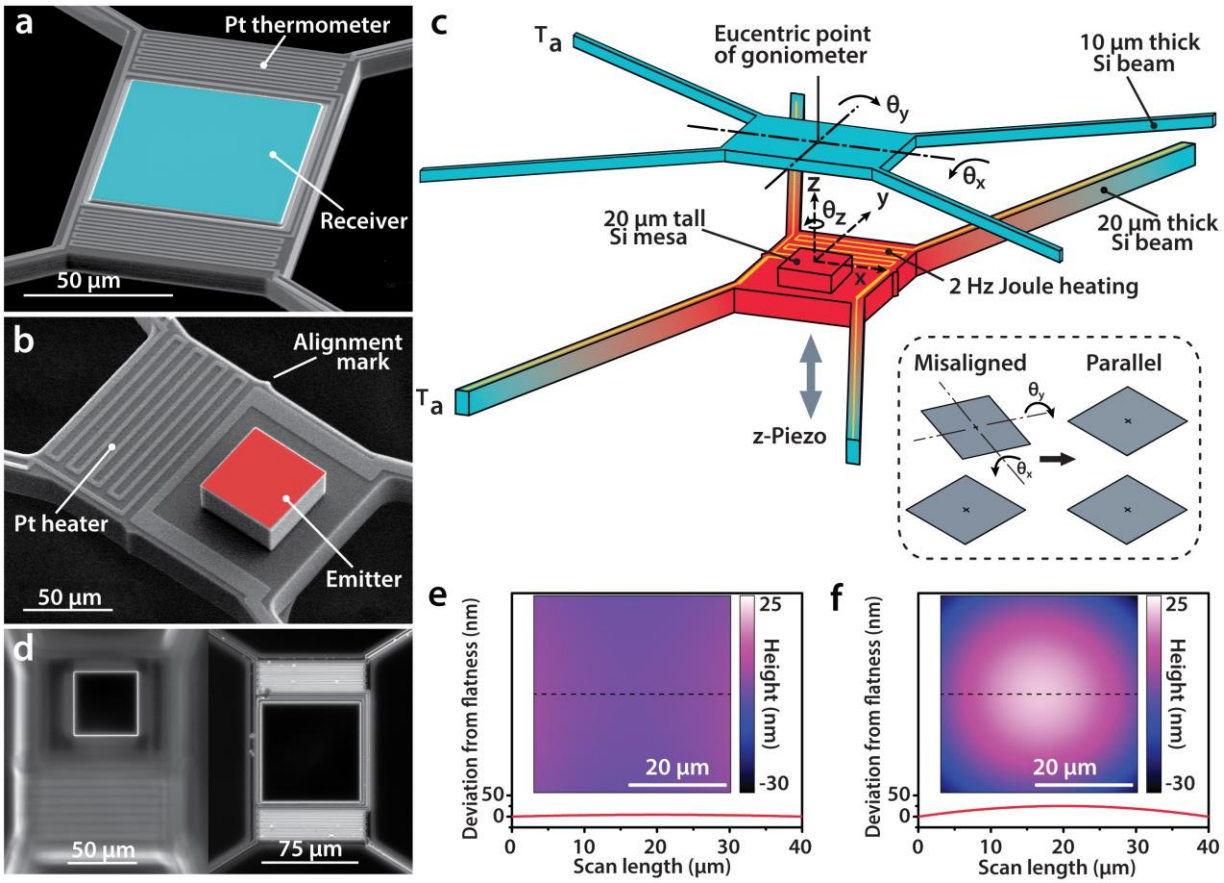

Figure 2-1. Microdevices for probing near-field radiation between parallel-planar surfaces. (a) Scanning electron microscope (SEM) image of the receiver device, which features a 80 µm × 80 µm region coated with a desired dielectric/metallic film (false-coloured in blue). (b) SEM image of the emitter, which features a 48 µm × 48 µm mesa-shaped region coated with SiO_2 or Au (top of mesa false-coloured in red). Both emitter and receiver devices are suspended by long and narrow Si beams to achieve excellent thermal isolation. (c) Schematic showing the orientation of the emitter and receiver devices with respect to each other. The relative alignment of the emitter and receiver (inset) can be controlled using a custom-built nanopositioner that enables lateral and angular control (θ_z) of the emitter as well as angular control (θ_x, θ_y) of the receiver about the x, y and z axes. (d) Optical images showing the emitter and receiver devices. (e) Line profile of the active region of the emitter showing the negligible deviation from planarity along the dashed line of the inset. Inset: topography obtained using atomic force microscopy. (f) As in e, but for the receiver. Small deviations from planarity of ~30–40 nm over a 40 µm × 40 µm region can be seen (dashed line aligned with the centre line parallel to the x axis of the receiver).

For radiative heat transfer measurements we parallelized and laterally aligned the emitter and receiver devices with respect to one another. To achieve this we made use of a custom-built nanopositioning platform developed in our laboratory (ref. [105], see Methods). The degrees of

freedom provided by the nanopositioner are shown in Figure 2-1c and enabled translation of the emitter along the *x*, *y* and *z* directions and rotation about the *z* axis (θ_z), while the receiver could be rotated about the *x* and *y* axes (θ_x, θ_y). Manipulating the devices with the nanopositioner while visualizing the devices under an optical microscope enabled parallelization to within 100–200 nm deviation over the 48 μm × 48 μm overlap region of the emitter and receiver devices (see Methods). Subsequently, the emitter, which was laterally displaced from the receiver during the initial parallelization (Figure 2-2b), was shifted laterally and placed vertically directly beneath (~10 μm) the receiver device (Figure 2-1a). Finally, a high vacuum (1 μtorr) with minimal mechanical vibrations was created with an ion pump (see Appendix A.1 Nanopositioner and Measurement Environment) to attenuate any contributions to heat transfer from air conduction to negligible levels.

To characterize the radiative heat transfer from the emitter to the receiver we modulated the temperature of the emitter sinusoidally at 2 Hz with an amplitude of $\Delta T_{Emit} = 2$ K, using the integrated Pt heater. The emitter device was then displaced towards the receiver (Figure 2-2d) with nanometre-precision control using a piezoelectric actuator while we simultaneously recorded the amplitude of the sinusoidal (2 Hz) temperature oscillations of the receiver (ΔT_{Rec}) with a Pt temperature sensor integrated onto the receiver device. The gap (*d*)-dependent radiative conductance $G_{Rad}(d)$ between the emitter and receiver (Figure 2-2a presents a thermal resistance network) is given by

$$G_{Rad}(d) = G_{Rec} \times \Delta T_{Rec}(d) / (\Delta T_{Emit} - \Delta T_{Rec}(d)) \qquad (2\text{-}1)$$

where G_{Rec} is the thermal conductance between the isolated region of the receiver and the Si substrate to which it is connected by thin and long beams, which was characterized to be 94.6 μW K^{-1}.

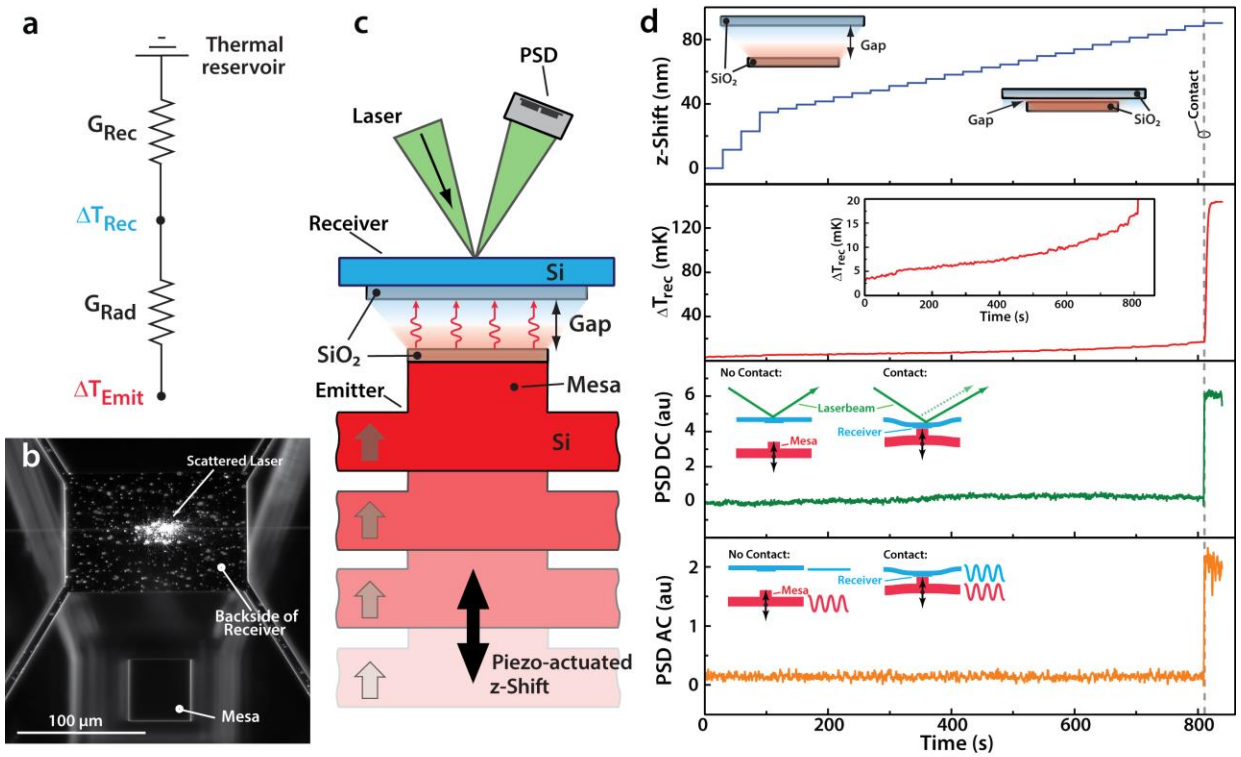

Figure 2-2. Measurement of near-field radiative heat transfer between parallel-planar surfaces. (a) Thermal resistance network identifying the primary heat transfer pathways. $\Delta T_{Emit} = 2$ K is the amplitude of the temperature oscillations of the emitter, G_{Rec} and G_{Rad} are the thermal conductances of the receiver and the vacuum gap, respectively. (b) Optical image showing the parallelized emitter and receiver devices (laterally displaced for visualization). The laser spot incident on the backside of the receiver device can also be seen. (c) Schematic showing both the displacement of the parallelized emitter device towards the receiver device and near-field radiative heat transfer between them. The laser beam and the position sensitive detector (PSD) used to detect contact are also shown. (d) Top panel: stepwise displacement of the emitter towards the receiver by a feedback-controlled piezoelectric actuator. Left and right insets illustrate the gap between the SiO_2 surfaces of the emitter and receiver at the beginning and just before contact, respectively. Second panel: recorded temperature rise of the receiver. Third panel: detection of contact as observed from the unmodulated signal from the PSD. The inset of the third panel describes the change in the reflected laser beam when the emitter and receiver snap into contact with each other (the dashed line in the right inset shows the position of the laser beam before snap-in). Bottom panel: detection of contact via the modulated PSD signal. The inset illustrates the modulation of the position of the receiver after contact.

We first probed the radiative heat transfer between emitter and receiver devices coated with a 2-μm-thick layer of SiO_2, which at nanoscale gaps provides an excellent approximation to bulk SiO_2 as the film thickness is much larger than the gap size [42]. The top panel of Figure 2-2d shows the displacement of the emitter towards the receiver, which starts with coarser steps (10 nm) and continues in finer steps (2 nm) close to contact. The second panel depicts ΔT_{Rec}, which steadily increases before contact is made. Throughout the approach, the optical signals (Figure 2-2b–d) that track the mechanical contact between the emitter and receiver (see Methods) do not change until contact is established (bottom two panels in Figure 2-2d). Contact is indicated by a simultaneous jump in both the optical signals and the temperature signal, the latter arising due to an increase in thermal conductance associated with heat conduction upon contact.

The gap-dependent radiative conductance for SiO_2–SiO_2 surfaces (Figure 2-3a, green squares) increases dramatically before contact is established. We found that the maximum measured near-field conductance could be enhanced systematically by tipping and tilting the receiver with respect to the emitter to further improve parallelism. Figure 2-3a shows the improvement that is achieved with such systematic optimization. It is also apparent that the conductance exceeds the blackbody limit, reaching a value of 1 μW K^{-1} just before contact. We estimate from the known angular resolution of our nanopositioner [105] that this optimization approach reduces any deviations from parallelism to be a few nanometres across the 48 μm × 48 μm regions over which the emitter and receiver devices have near-field interactions (see Methods).

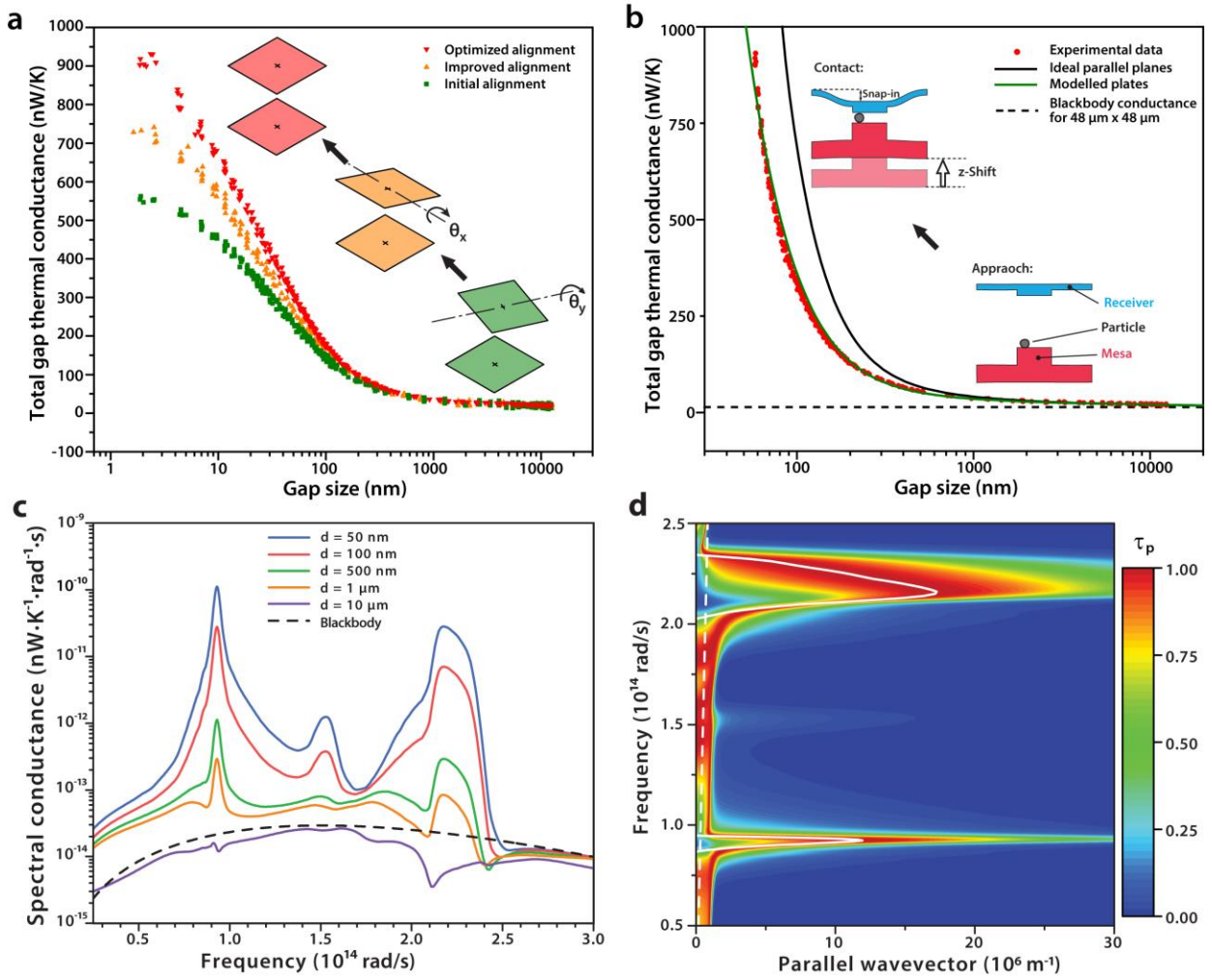

Figure 2-3. Optimization of parallelization and demonstration of enhanced heat conductances in sub-100 nm gaps between SiO_2 surfaces. (a) Observed enhancement in radiative heat transfer on optimization of the parallelism by angular tilts θ_x, θ_y along the x and y axes, respectively. Insets: approach followed to improve alignment. (b) Comparison of the experimentally measured radiative thermal conductance (displaced by 55 nm) with computational data. Black solid line: computed conductance for ideal parallel planes. Green line: computed conductance that accounts for small deviations in planarity. Dashed line: radiative conductance between two 48 μm × 48 μm planar blackbody surfaces with a view factor of unity. Insets: the minimum achievable gap size is limited by the presence of nanoscale particles and snap-in (insets not drawn to scale and proportion to help visualization). Data are from eight different measurements. (c) Computed spectral heat conductance between 2-μm-thick films deposited on Si for various gap sizes. The spectral conductance between blackbodies is also shown for comparison. (d) Computed transmission for TM modes (τ_p in equation (2-2)) that dominate radiative heat transfer is shown along with the dispersion for surface phonon polaritons (SPhPs) at a gap size of 50 nm (dashed line: dispersion of light in vacuum). It can be seen that the transmission is very large in the region where the dispersion curve (white solid line) of SPhPs overlaps with the transmission plot, clearly indicating the role of SPhPs in enhancing radiative heat transfer.

To compare the experimental results with theory we first computed the thermal conductance per unit area $h_{Rad}(d)$ for the SiO_2 thin-film coated plates using the expression [111, 112]

$$h_{Rad}(d) = \int_0^\infty \frac{d\omega}{4\pi^2} \frac{\partial \Theta(\omega, T)}{\partial T} \int_0^\infty dk k \left[\tau_s(\omega, k, d) + \tau_p(\omega, k, d) \right] \tag{2-2}$$

where T is the temperature, ω is the radiation frequency, k is the magnitude of the wavevector component parallel to the thin-film layer, d is the gap size, and τ_s and τ_p are the transmission probabilities for transverse electric (TE) and transverse magnetic (TM) modes, respectively, which depend on the Fresnel coefficients of the interfaces (see Methods). Next, we computed the radiative thermal conductance from $G_{Rad}(d) = h_{Rad}(d) \times A_{device}$, where A_{device} is the area of the mesa (48 μm × 48 μm). The computed total conductance for ideal, parallel SiO_2surfaces is shown as the black line in Figure 2-3b. To more accurately estimate the thermal conductance in our devices, which feature small deviations from planarity (~30 nm over the 48 μm × 48 μm active device region, Figure 2-1), we employed the Derjaguin approximation [30, 42, 101, 104] (see Appendix A.3 Derjaguin Approximation) and computed the near-field conductance between the planar emitter and the receiver. The computed total conductance after accounting for curvature of the receiver is shown in green in Figure 2-3b. Note that we have also accounted for the relatively small gap size-dependent far-field contributions from other regions of the devices via finite element simulations.

Before performing systematic comparisons of the experimental and computational results, it is necessary to account for the presence of small particles of up to 30–40 nm in size, which are present on the microfabricated emitter and receiver devices. In addition, the smallest gap size at which measurements can be performed is also limited by snap-in, which is ~20 nm in

size (Figure 2-2c, third panel from the top, inset of Figure 2-3b). We also ruled out that thermally driven deflections of the emitter and receiver significantly affect gap sizes. We followed well-established approaches [30, 42, 101] to account for these factors and concluded that the smallest gap size in our measurements is limited to ~50–60 nm (~40 nm due to particles + ~20 nm due to snap-in). To reflect this achieved (minimum) gap size, the measured conductance data in Figure 2-3b and Figure 2-4a, c were displaced by 55, 60 and 55 nm, respectively.

It can be readily seen (Figure 2-3b) that the measured conductances for SiO_2 are in excellent agreement with the computed conductances. Furthermore, it can be seen that the total conductance of the interacting area (48 μm × 48 μm) of the emitter and receiver increases ~100-fold compared to the total far-field conductance, assuming an emissivity of 0.84 for bulk SiO_2 (ref. [8]). This dramatic enhancement is entirely consistent with theoretical predictions shown in Figure 2-3c, which presents the spectral conductance (see Methods) for SiO_2 surfaces at various gap sizes. Specifically, it can be seen that large enhancements arise from huge contributions to heat transfer from two relatively narrow frequency ranges. As described in previous works [27, 42], these contributions arise from surface phonon polaritons, the signature of which can be seen in the computed transmission plot, which is overlaid on their dispersion relation in Figure 2-3d. It also becomes obvious from this plot that the computed transmission for transverse magnetic (TM) modes, which completely dominate radiative heat transfer, reaches its highest values in regions where surface phonon polaritons are supported.

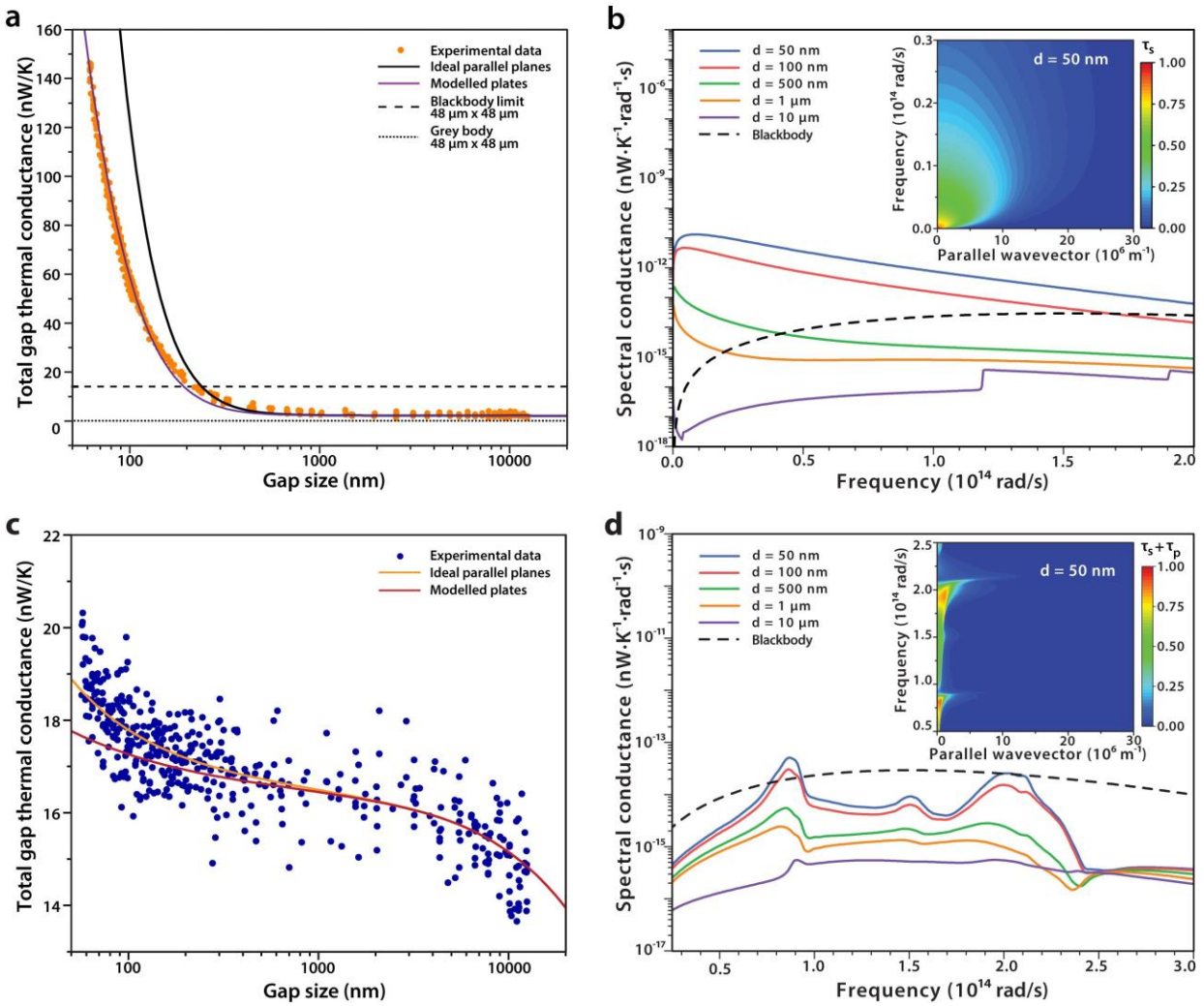

Figure 2-4. Enhanced heat conductances in <100 nm gaps of Au surfaces and near-field radiation between dissimilar surfaces. (a) Comparison of experimentally measured radiative thermal conductance (for Au–Au, displaced by 60 nm) with computational data. Black solid line: computed conductance for ideal parallel planes. Purple line: computed conductance that accounts for small deviations in planarity. Dashed line: radiative conductance between two 48 μm × 48 μm planar black surfaces with a view factor of unity. Dotted line: computed far-field conductance for 48 μm × 48 μm planar Au surfaces with a view factor of unity and the appropriate emissivity for Au (0.02). Data are from nine different measurements. (b) Computed spectral conductance curves (for Au–Au) together with the transmission (at a gap size of 50 nm, inset) for TE modes (τ_s) that dominate radiative heat transfer. (c) Measured thermal conductance for mismatched parallel-planar surfaces (SiO_2–Au), displaced by 55 nm. Data from ten different measurements. The observed enhancements are very small due to a mismatch in the dielectric properties. Solid lines: computed radiative conductance for ideal planes and for planes that feature small deviations from planarity. (d) Computed spectral conductance for SiO_2–Au gaps and the total transmission ($\tau_s + \tau_p$) for TE and TM modes. Note the much smaller heat conductance compared with Au–Au and SiO_2–SiO_2 surfaces.

After demonstrating the large enhancements between SiO_2–SiO_2, we performed experiments in which the emitter and receiver devices were coated with Au. Following the protocol described above, we obtained the radiative conductance for various gap sizes. The conductance (at optimized receiver parallelization) obtained after displacing the measured data by 60 nm (similar to the case outlined for SiO_2) is shown in Figure 2-4a together with the computed thermal conductance. Again, the agreement between theory and experiment is very good. We also obtain an ~1,000-fold enhancement (Figure 2-4a) in radiative conductance compared to the far-field conductance between the interacting areas. Moreover, the obtained nanoscale conductances are also found to be ~10 times larger than the blackbody limit [9], which is particularly impressive for metallic surfaces as they feature a very low emissivity (0.02 for Au) [8]. The computed spectral conductances for Au surfaces are shown in Figure 2-4b, as well as the transmission plot for the transverse electric (TE) modes (inset). As expected [113], the near-field enhancements for Au–Au surfaces feature contributions from a broad range of frequencies and do not have dominant contributions from surface modes.

Finally, to demonstrate the versatility of our experimental platform and to illustrate the critical role played by dielectric resonances in near-field enhancements, we performed radiative heat transfer measurements between SiO_2–Au and Si–Au surfaces. The measured data along with the corresponding calculated near-field conductance (after offsetting the data by 55 nm) are shown in Figure 2-4c for SiO_2–Au surfaces. For the case of surfaces with mismatched dielectric properties the radiative enhancements are much lower than those for surfaces with matched dielectric properties. These measurements are indeed consistent with computed spectral conductance curves (Figure 2-4d) and transmission (inset of Figure 2-4d) for SiO_2–Au surfaces,

which confirm that near-field radiative heat transfer for SiO_2–Au surfaces is orders-of-magnitude lower than that for SiO_2–SiO_2 or Au–Au surfaces.

2.4 Conclusion

We have reported 100- to 1,000-fold near-field enhancements above the far-field limit of thermal radiative conductances by systematically probing near-field radiative heat transfer over a large range of nanoscale gaps between planar surfaces. Our experimental approach makes possible non-contact modulation of thermal conductance and radiative cooling, which may both prove critical for novel thermal management strategies. Perhaps more importantly, we expect that this work will stimulate a number of detailed experimental investigations of intriguing near-field radiation-based theoretical proposals [46, 53, 67-69, 71, 77] for thermal management and energy conversion that have defied experimental analysis.

2.5 Methods

Procedure to parallelize the emitter and receiver devices: Parallelization was accomplished using a custom-built nanopositioner and an integrated reflected light microscope (Zeiss Axiotech Vario) with a shallow depth of field (2 μm) and long working distance (9 mm) objective (Zeiss LD EC Epiplan-Neofluar 50×/0.55 HD). We began by aligning the planar surface of the emitter microchip (10×10 mm^2), into which the emitter device was integrated, to be parallel with the image plane of the microscope. Parallelization started by sequentially translating three laterally separated (8 mm) points on the emitter chip surface to the centre of the field of view using an *x*–*y* linear stage. Subsequently, a tip-tilt mechanism was used to ensure that all three points were contained in the same image plane. As a result, the angular deviation between the emitter's mesa surface (Figure 2-1) and the image plane was guaranteed to be <250 μrad (2 μm/8 mm). Subsequently, a similar approach

was used to tip and tilt the receiver microchip (10×10 mm^2) using a custom-built motorized goniometer. Once both chip surfaces were made parallel to the image plane, the two must also be parallel to one another with small angular deviations (<500 μrad). Therefore, if the active areas of the devices were perfectly parallel to the corresponding chip surfaces, which was not always true (see below), the deviations from parallelism across the active area of the devices were ~30 nm. After this parallelization step, the two microdevices were laterally aligned using a micropositioner and the vacuum gap size was controlled using a piezoelectric actuator with steps as small as 2 nm from 10 μm to sub-100 nm.

As described earlier, the parallelism between the devices was further improved by systematically varying the tip and tilt of the receiver device by small increments (limited to ~20–40 μrad by backlash) until the observed near-field conductance was maximized. This fine alignment, which can in principle decrease deviations from parallelism to ~2 nm (~20–40 μrad × 48 μm), was greatly facilitated by the exceptional angular resolution (20–40 μrad) of our goniometer. The need for such fine angular optimization arose due to the observation that the beams of the emitter and receiver devices, although stiff, were slightly curved due to internal stress, which caused an overall angular deviation of ~20 mrad between the active surface and the chip surface, as measured by confocal laser scanning microscopy.

Detection of contact between emitter and receiver: To accurately detect contact between the emitter and receiver, we sinusoidally (4 kHz) modulated the position of the emitter (3 nm peak to peak) as it was displaced towards the receiver. This modulation was accomplished using a piezoactuator whose displacement was controlled with 2 nm resolution using embedded strain-gauge sensors (SGSs). Deflections of a laser beam reflected from the back of the receiver (Figure 2-2b, c) were monitored using a position sensitive detector (PSD).

Specifically, the output of the PSD was monitored both by a lock-in amplifier (time constant 30 ms) and a data acquisition system. As can be seen from Figure 2-2d, when contact was made, the output of the lock-in amplifier (PSD AC) suddenly increased due to sinusoidal displacements of the receiver. Furthermore, at contact, the unmodulated part of the PSD signal (PSD DC) also increases because of a sudden displacement of the receiver due to snap-in, which occurs when the emitter is close enough to the receiver that residual electrostatic charges cause mechanical instabilities. In our experiments, snap-in was reduced to very small values (~20 nm) due to the large stiffness of our devices and the incorporation of an electrically grounded thin-film wire and plane for the emitter and receiver, respectively. In all our experiments we used a two-stage temperature controller that maintained the temperature at ~298 K and minimized the temperature drift of the nanopositioner to <10 mK over the period of the experiment.

Modelling: The radiative heat transfer between parallel plates was calculated following the formalism of fluctuational electrodynamics (see Appendix A.2 Theoretical Modelling of Near-Field Radiation for details). The effect of the deviation from planarity was accounted for via the Derjaguin approximation, which has been used successfully by us [42] and others [30, 101] in the past. The far-field radiation between the emitter and receiver devices, as well as the gap-dependence of the far-field radiation, was estimated via finite element modelling. The spectral conductance $G_{Rad}(\omega, d)$ plotted in Figure 2-3c and Figure 2-4b, d is related to the spectral heat conductance per unit area

$$h_{Rad}(\omega, d) = \frac{1}{4\pi^2} \frac{\partial\left[\hbar\omega / (e^{\hbar\omega/k_B T} - 1)\right]}{\partial T} \int_0^\infty dk k \left[\tau_s(\omega, k, d) + \tau_p(\omega, k, d)\right] \qquad (2\text{-}3)$$

by

$$G_{Rad}(d) = h_{Rad}(d) \times A_{device} \tag{2-4}$$

where A_{device} is 48 μm × 48 μm.

Chapter 3 Hundred-Fold Enhancement in Far-Field Radiative Heat Transfer Over the Blackbody Limit

Reproduced with permission from reference [99]:

Dakotah Thompson, Linxiao Zhu, Rohith Mittapally, Seid Sadat, Zhen Xing, Patrick McArdle, M. Mumtaz Qazilbash, Pramod Reddy and Edgar Meyhofer, *Nature*, In Press, (2018).

3.1 Abstract

Radiative heat transfer plays a central role in entropy generation and energy transfer on length scales ranging from nanometers to light-years [114]. The blackbody limit [9], as established in the radiative heat transfer theory of Max Planck, provides a convenient metric for quantifying radiative heat transfer rates as it predicts the maximum possible radiative heat transfer rate between macroscopic objects in the far-field. While recent experimental work has verified the feasibility of overcoming the blackbody limit in the near-field [30, 98, 101, 102], heat transfer rates exceeding the blackbody limit in the far-field, i.e. at separations greater than the Wien's wavelength [8], have never been demonstrated. Here we show, using custom fabricated calorimetric nanostructures with embedded thermometers, that radiative heat transfer between planar membranes with sub-wavelength dimensions can exceed the blackbody limit in the far-field by more than two orders of magnitude. The observed heat transfer rates are found to be in good agreement with our calculations. These findings may have a direct impact on a variety of fields where radiative heat transfer plays a major role.

3.2 Introduction

Radiative heat transfer (RHT) plays a key role in diverse processes from controlling the temperature of planetary atmospheres [114] and planetary formation [115] to radiative cooling [116] and thermophotovoltaic energy conversion [117]. Recent studies of near-field RHT [30, 98, 101, 102] have experimentally shown that the RHT between surfaces separated by nanoscale gaps (gaps below the dominant thermal wavelength λ_{Th}, ~10 microns at room temperature) can greatly exceed the fundamental blackbody limit [9] due to evanescent modes which are present in the near-field. Such near-field effects are now being assessed extensively for their potential in energy conversion and thermal management technologies [71, 77]. However, what remains entirely unexplored experimentally, is the feasibility of accomplishing dramatic enhancements in RHT in the far-field (i.e. the region where no evanescent modes are present) when the surfaces are separated by gaps larger than λ_{Th}.

To elaborate, the far-field RHT (FF-RHT) theory of Planck [9], which is based on a "ray" picture, predicts that given two finite sized objects of surface areas A_1 and A_2 (Figure 3-1a), the maximum possible conductance (G_{max}) between these objects in the blackbody limit is given by $G_{max} = 4\sigma T^3 A_1 F_{12} = 4\sigma T^3 A_2 F_{21}$, where F_{12} and F_{21} are geometric view factors that satisfy the reciprocity relationship $A_1 F_{12} = A_2 F_{21}$ (see Figure B-1 or Ref. [8]). Planck himself pointed out that the blackbody limit is not applicable when (1) the gap-size between the objects is less than λ_{Th} or (2) one or more dimensions of the objects are smaller than λ_{Th}. As briefly described above, recent experimental measurements [98] of radiative thermal conductances between planar macroscopic surfaces (or objects) separated by gap-sizes below λ_{Th}, established extraordinary increases in comparison to the expected blackbody limit. Therefore, one may naively expect that the blackbody limit may also be readily overcome for sub-wavelength thickness ($<\lambda_{Th}$) objects in

the far-field. For example, could sub-wavelength diameter spherical particles, which feature sharp resonances in their absorption cross-section, dramatically exceed the blackbody limit? Both, our detailed computational analysis (see Figure B-2) and past computations suggest [32, 118, 119], however, that such exceedances are not anticipated for metallic spheres and very small exceedances (in the range of up to a few-fold) may be expected for dielectric spheres or metallic cylinders. In strong contrast, interesting analytical work [120] performed recently has indicated that, in principle, for sub-wavelength objects, there may be no limit to exceedances in thermal emission and absorption that can be achieved in comparison to the blackbody limit.

Experimental work [121-123] on individual sub-wavelength structures has been largely limited to probing the emission spectra, because quantifying heat output or performing RHT measurements between these structures is very challenging. Notably, a recent experiment [123] that probed emissions from sub-wavelength cylindrical SiO_2 wires revealed that the net radiative rates from these cylinders are actually much smaller than those predicted by the blackbody limit. Taken together, the question of whether the radiative heat transfer between sub-wavelength structures in the far-field can greatly exceed Planck's blackbody limit remains completely unanswered and has never been addressed experimentally.

3.3 Experiments, Results and Analysis

In order to explore if very large enhancements over the blackbody limit can be accomplished we chose to work with thin planar structures (similar to those shown in the bottom of Figure 3-1a), where one of the dimensions (thickness (t)) was chosen to be much smaller than λ_{Th} at room temperature. The planar device geometries selected in this work represent shapes often employed in MEMS/NEMS technologies and for nanoscale conduction studies [124, 125] and are experimentally tractable for quantitative RHT measurements. Specifically, we custom-

fabricated a series of devices featuring two coplanar silicon nitride (SiN) membranes (Figure 3-1c), where *t* was varied from 270 nm to ~11 μm (see Methods and Figure 3-6 for information regarding device fabrication). Each of these membranes is suspended by thin and long beams and features an integrated serpentine Pt-resistor (see inset of Figure 3-1c and Figure 3-1d) that can be employed to either heat a membrane or measure its temperature rise. Further, the separation between the membranes was chosen to be 20 μm to ensure that near-field effects are negligible as λ_{Th} ~10 μm at 300 K (see Figure B-13 where we computationally show that near-field effects are negligible (<0.1% at 300 K)). Our devices, fabricated from SiN, feature internal tensile stresses that ensure that the membranes feature excellent planarity and are coplanar as confirmed by laser scanning confocal microscopy, see Figure 3-1e & Figure 3-1f (additional details in Methods and Figure 3-6).

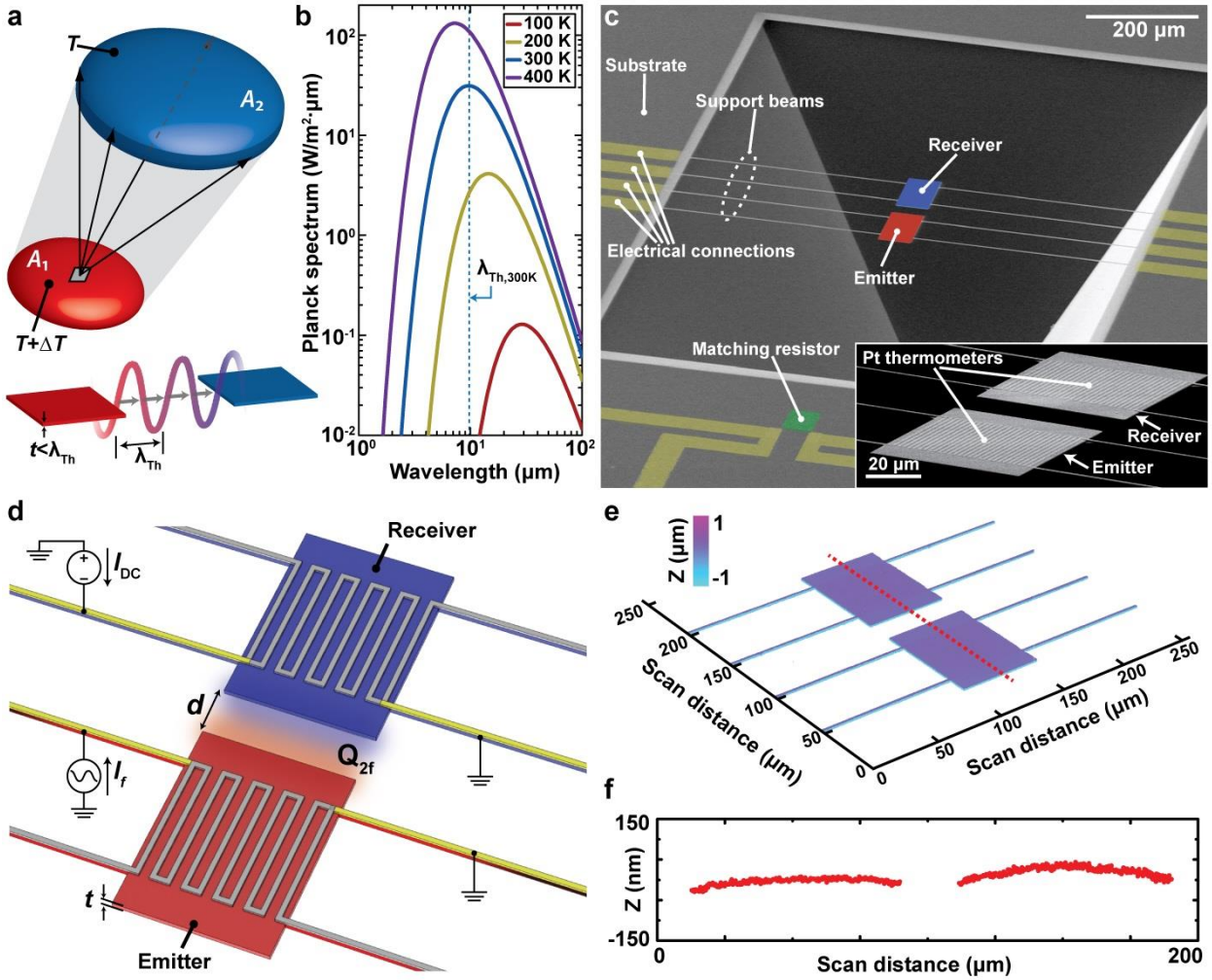

Figure 3-1. Probing radiative heat transfer between sub-wavelength structures. (a) Schematic describing the heat transfer between finite sized objects and sub-wavelength plates/membranes, here λ_{Th} refers to the Wien's wavelength, which is ~10 μm at room temperature (see (b)). Red indicates a hotter temperature ($T + \Delta T$) and blue indicates a colder temperature (T). (c) Nanofabricated experimental platform employed in probing radiative heat transfer. The devices are made from SiN and feature platinum resistance thermometers/heaters. (d) Schematic representation of the nanofabricated devices. One of the membranes, called the emitter, is heated by a passing a sinusoidal current of amplitude I_f and frequency f via the integrated Pt heater, which results in a heat current from the heater to the receiver membrane. The heat current (Q_{2f}) is measured by monitoring the temperature rise of the receiver via the integrated Pt resistance thermometer (by passing a DC current I_{DC}). The thickness of the membranes and the gap size between them are represented by t and d, respectively. (e) Scans of 2 μm-thick nanofabricated devices via a confocal microscope reveal that the membranes have excellent planarity. (f) The profile along the line shown in panel e. It can be seen that any deviations from planarity are <100 nm.

The basic strategy to quantify the RHT between the planar device structures in our measurements is to increase the temperature of one of the membranes by Joule heating via the integrated Pt heater and then measure the temperature rise in the unheated membrane due to RHT from the hot to the cold membrane (see Figure 3-1d). To perform the desired measurements the devices were first placed in vacuum (at room temperature and a vacuum of $<10^{-6}$ torr), which attenuates the parasitic heat conduction between the membranes arising from residual air molecules to negligible levels (see Methods for quantification). Next, one of the planar devices, the emitter, was heated by inputting a sinusoidal current with amplitude I_f at frequency f resulting in temperature oscillations ($\Delta T_{\text{emit, }2f}$) at $2f$, which were measured following protocols that we developed previously [92, 93] (see Methods for a description). The radiative heat flux (Q_{2f}) from the emitter to the second device, called the receiver, results in temperature oscillations of the receiver membrane ($\Delta T_{\text{rec, }2f}$) that we quantified by supplying a DC current (I_{DC}) to the Pt resistor and measuring the voltage fluctuations at $2f$ (see Methods). Results from measurements performed on a 486 nm thick device are shown in Figure 3-2a, where $\Delta T_{\text{rec, }2f}$ is plotted as a function of $\Delta T_{\text{emit, }2f}$. The inset of Figure 3-2a shows the expected temperature field of the emitter device estimated from finite element simulations. It can be seen that the suspended membrane of the emitter has a uniform temperature, while there is a linear temperature drop in the beams.

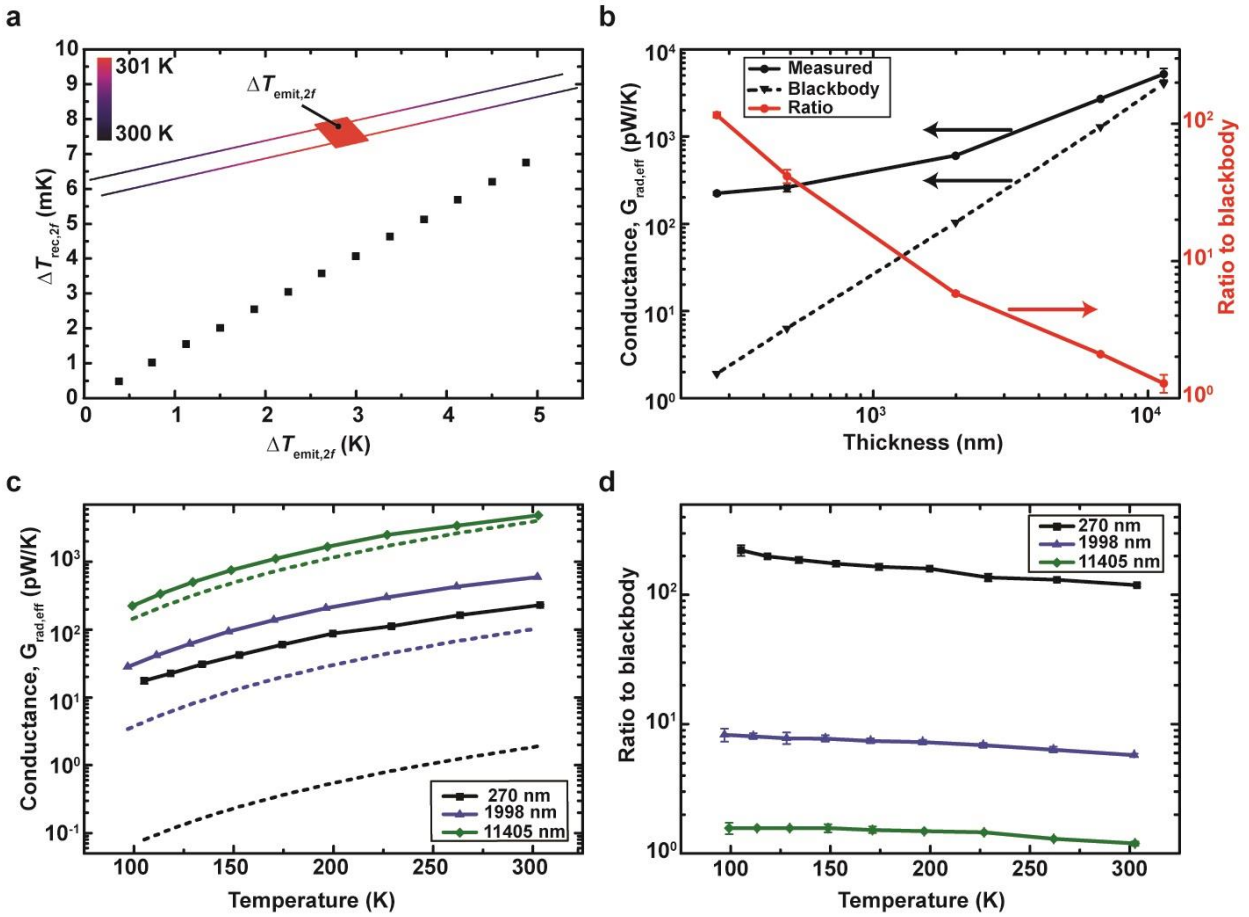

Figure 3-2. Radiative conductance between membranes with sub-wavelength dimensions. (a) Measured temperature rise of the receiver ($\Delta T_{rec,2f}$) due to radiative heat flow from a heated emitter. Error bars (standard deviation, smaller than symbols) were obtained from 50 minute-long raw thermal records (see Methods for details). The inset shows the temperature profile of the emitter ($\Delta T_{emit,2f}$) from finite element simulations. (b) The effective radiative conductance ($G_{rad,eff}$) at room temperature (black dots) for membrane thicknesses from ~11 μm to 270 nm. Errors for $G_{rad,eff}$ (usually smaller than the symbols) were determined from a regression analysis of data as shown in a (see Methods for details). The computed $G_{rad,eff}$ (black triangles, FF-RHT theory with an emissivity of 1 for all objects) is significantly smaller for thin devices and the ratio of the measured to the simulated radiative conductance increases steeply with reduced devices thicknesses (red). (c) Measured $G_{rad,eff}$ as a function of temperature and device thickness. Simulated results (dashed line, FF-RHT theory) are found to dramatically under-predict $G_{rad,eff}$ at all temperatures, particularly for the thinnest devices. Similar data for the 486 nm and 6712 nm-thick devices are shown in Figure 3-3. (d) Ratio of the measured to estimated (FF-RHT) conductance as a function of temperature. For the thinnest devices the measured conductance exceeds predictions by more than 100-fold.

The effective radiative conductance ($G_{rad,\,eff}$) between the emitter and receiver is estimated from, $G_{rad,\,eff} = G_{beams,\,rec} \times (\Delta T_{emit} / \Delta T_{rec} - 1)^{-1}$, where $G_{beams,\,rec}$ is the experimentally determined thermal conductance of the receiver's beams (see Figure 3-8). The measured $G_{rad,\,eff}$ for devices of various thicknesses is shown in Figure 3-2b (black dots). It can be seen that $G_{rad,\,eff}$ decreases monotonically with decreasing thickness of the devices as one would expect from basic FF-RHT theory of Planck [9] (referred to as FF-RHT theory in this work). In order to quantitatively compare the experimentally obtained data with the predictions of FF-RHT theory, we computed $G_{rad,\,eff}$ by performing comprehensive RHT simulations using a finite element method (see Figure B-3 for details of simulations), which completely accounts for the geometric view factors [8] and assumes the emissivity of the devices to be 1 (i.e. the blackbody limit). The measured $G_{rad,\,eff}$ is found to be much larger than the simulated blackbody value (black triangles) for the thinnest devices. Specifically, for membranes with a thickness of 270 nm, the ratio of the measured radiative conductance to the simulated blackbody conductance (red dots) is more than a factor of 100. However, for the thickest device (~11 μm thick) the predictions are in good agreement with the experimental data. The data clearly show that—for sub-wavelength ($t << \lambda_{Th}$) planar structures—the blackbody limit can be readily overcome. In fact, such large enhancements over the blackbody limit have only been reported in the near-field [98, 126] where gap-sizes were reduced to 10s of nanometers, and never in the far-field. We note that we performed several control experiments (see Methods) which unambiguously rule out the possibility that the observed $G_{rad,\,eff}$ is due to other heat transport mechanisms, such as conduction through air or the substrate or spurious electrical signals due to capacitive coupling between the Pt heater and sensor, instead of radiative heat transfer.

To further understand the effect of λ_{Th} on the RHT properties of our devices we performed measurements where the temperature (T) of the devices was systematically decreased from 300 K to 100 K. Since FF-RHT theory predicts that $\lambda_{Th}T$ = 2898 μm•K (Wien's law) the thermal wavelength increases with decreasing temperatures resulting in an even larger contrast between λ_{Th} and the thickness of the devices. The data obtained from these measurements for three different thicknesses (270 nm, 1998 nm and 11405 nm) are shown in Figure 3-2c (data for other thicknesses are presented in Figure 3-3a), which demonstrates that the measured thermal conductance declines monotonically with decreasing temperature. The corresponding simulated FF-RHT thermal conductances (dashed lines) are also shown and are found to be much smaller than the measured conductances for the thinnest devices. The ratio of the measured conductance to the simulated conductance (for the devices of three thickness described earlier) are shown in Figure 3-2d. It is clear from these data that the disagreement between the measured and computed conductances persists at lower temperatures. In fact, for the thickest device it can be seen that the agreement between measurements and simulation is very good at 300 K but at lower temperatures the measured conductances are larger than that predicted by simulations, again highlighting the failure of FF-RHT theory when $\lambda_{Th} >> t$. We note that the contribution of near-field effects is negligible even at 100 K (<2%, see Figure B-13). Taken together, these data raise the important question: Can the 100-fold enhancement in comparison to the blackbody limit be quantitatively explained?

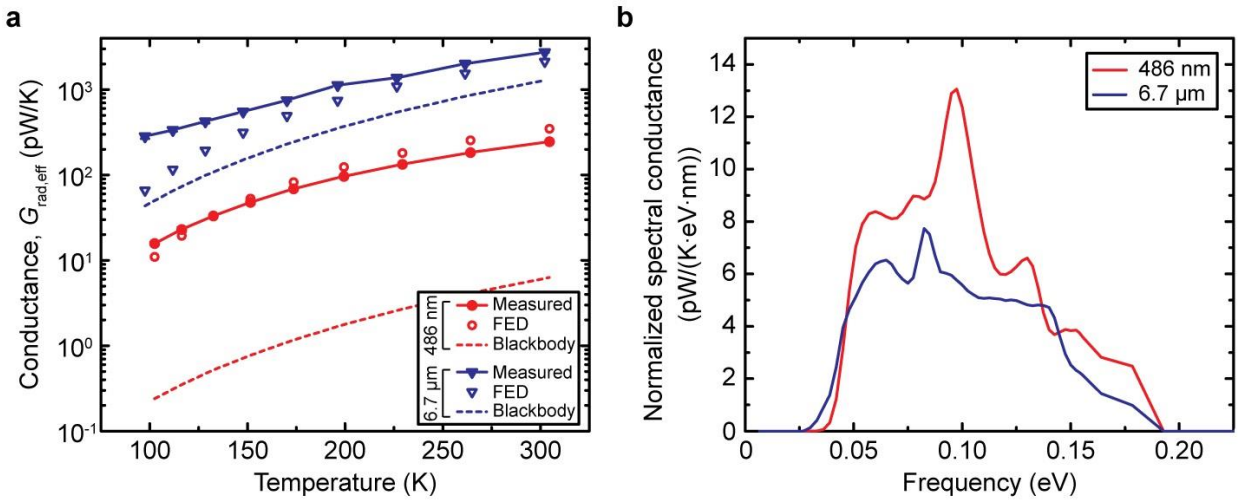

Figure 3-3. Radiative conductance in devices with 486 nm and 6712 nm thick membranes. (a) $G_{rad,eff}$ as a function of temperature for 486 nm thick and 6712 nm thick devices. Experimental measurements (solid symbols) are compared to values calculated via FED (open symbols) and COMSOL-modeled blackbody values (dashed lines). (b) BEM calculation of the normalized spectral radiative conductance at 300 K for 486 nm thick and 6712 nm thick devices. Spectral conductance values are normalized to the thickness of each device.

To address this question we resorted to the framework of fluctuational electrodynamics [11, 12] (FED)—a theory that has been extensively employed in the past to study near-field RHT as it does not rely on the assumptions of FF-RHT theory [9]. In performing our simulations we implemented our FED model using the boundary element method [17, 127] (BEM). Such BEM-based FED models have only been developed recently and enable for the first time an exact analysis of radiation for complex geometries such as our membranes and the support beams. However, the Pt lines were not incorporated into our FED models to keep the computations tractable. For the FED calculations our device geometries were discretized into surface elements as shown, for example, in Figure 3-4a (details of meshing are discussed in Figure B-4) for the BEM mesh employed in simulations of our ~2 μm thick device. Key to performing the desired calculations are the dielectric properties of SiN, which were previously characterized in the literature [128], but, were also measured for our specific films.

The calculated $G_{rad,\,eff}$ from FED simulations are shown in Figure 3-4b, and in contrast to FF-RHT theory based simulations, are in excellent agreement with the measured $G_{rad,\,eff}$ for all thicknesses (all deviations are <30%). To obtain deeper insight into the reasons why thinner devices support much larger conductances than predicted by FF-RHT theory, we computed the spectral heat conductance for each device and normalized it by the thickness of the device. The normalized data are shown in Figure 3-4c (for three thicknesses) and are found to be much larger for the thinnest device than for thicker devices. These deviations arise primarily at frequencies where there is a higher density of guided modes that are confined to the SiN membranes as revealed by the dispersion relation for guided modes in 270 nm thick SiN membranes (see inset Figure 3-4c and Figure B-14 for additional details).

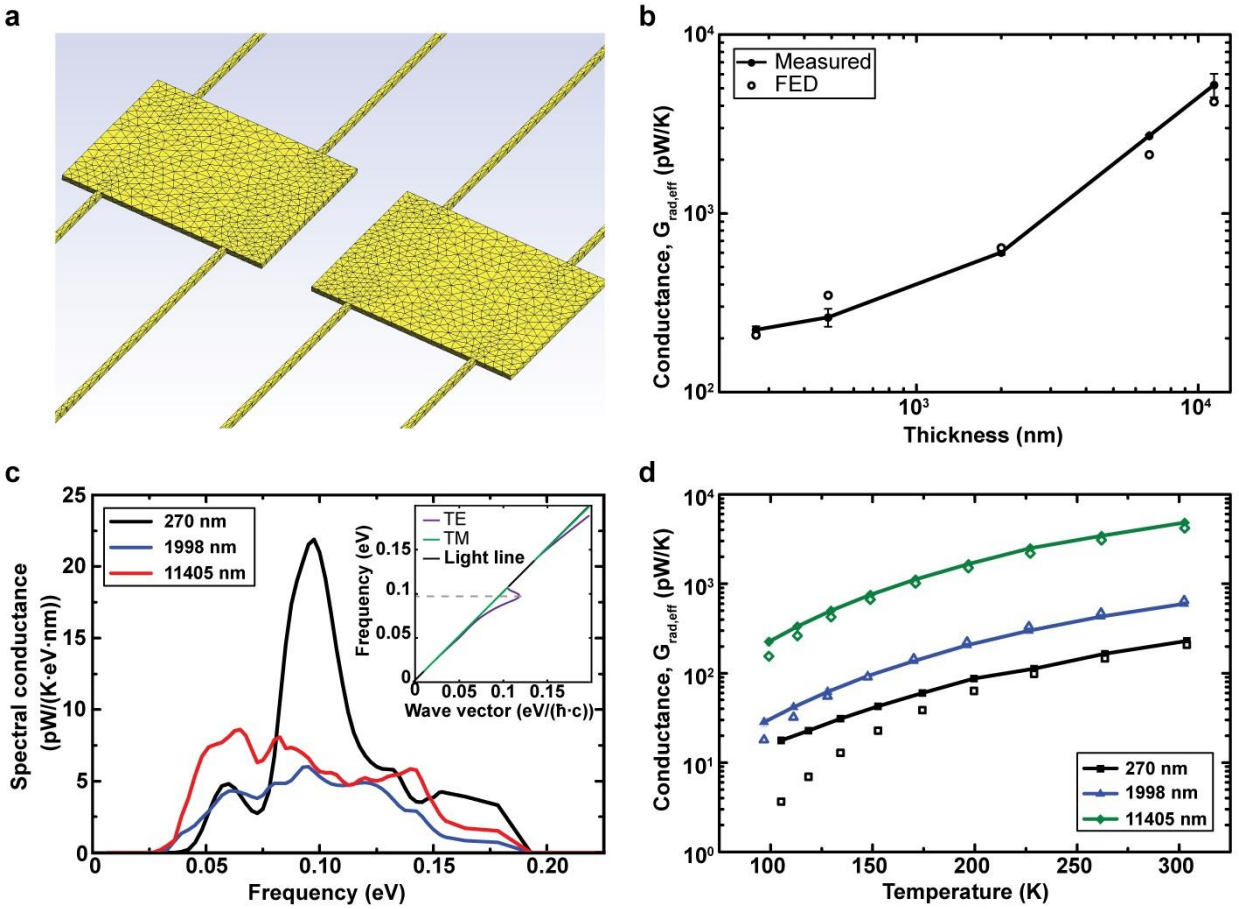

Figure 3-4. Comparison of experimental data with Fluctuational Electrodynamics (FED) based simulations. (a) Schematic depicting the meshing scheme employed in our calculations using a boundary element method (BEM). The exact geometry of the membranes is taken into account. However, the metal lines are excluded to make the computations tractable. (b) Comparison of the measured radiative conductance ($G_{rad,\,eff}$, shown in black solid circles) with $G_{rad,\,eff}$ obtained from FED simulations (black open circles) at room temperature. (c) The spectral heat conductance, normalized to the thickness of the devices, for devices of various thicknesses at room temperature. It can be seen that the spectral heat transfer is dominated by a narrow range of frequencies for the thinnest devices. This narrow band of frequencies corresponds to the range over which the dispersion relation for guided modes becomes highly dispersive, indicating a larger density of states in a small range of frequencies. See inset for the dispersion relation of guided modes in the 270 nm-thick SiN membrane (see Figure B-14 for additional details). Similar data for the 486 nm and 6712 nm thick devices are shown in Figure 3-3. (d) The measured and computed (FED) $G_{rad,\,eff}$ at various temperatures agree well with each other at all temperatures except for some discrepancies at the lowest temperatures (see Figure B-11 and Figure B-12 for a discussion of possible sources of these discrepancies). Error bars (obtained in a similar fashion to that in Figure 3-2c) for the measured data are present, but too small to be seen (see Methods for a description of how error bars were obtained).

Finally, we also performed FED-based calculations of the effective conductance of the devices as a function of device temperature. For all the devices, except the thinnest device, the FED-based computations are found to agree very well with the measured results over all temperatures. For the thinnest device the agreement between FED-based calculations and the measurements is somewhat poor at lower temperatures (100 K – 200 K). While this disagreement was initially puzzling, it can be largely resolved when one considers the contributions from the metallic lines, which were ignored in our FED-based calculations. Specifically, our calculations for metallic lines (see Figure B-11, Figure B-12), consistent with past work [119], show that at low temperatures the contributions of the metallic wires to $G_{\text{rad, eff}}$ can be as large as several pW/K and therefore can dominate RHT between the thinnest devices.

The above discussion shows that, while the unique FF-RHT phenomena observed by us can not be explained with FF-RHT theory [8], they are consistent with the predictions of FED. The experimental data and analysis presented above raise the following questions: Why does FF-RHT theory fail to explain the experimental data? How general are the observed deviations, i.e. can similar enhancements be obtained from other materials and geometries? To address these questions we considered a simplified geometry where we analyzed the RHT for isolated membranes, similar in dimensions to those used in our experiments, but without beams. We first computed the magnitude of the time-averaged Poynting vector (S_{FED}) for membranes of various thicknesses, as a function of the polar angle (θ) for fixed azimuthal angle and distance (60 μm, see Figure 3-5a), at room temperature, by using the electromagnetic solver SCUFF-EM [129]. Next, we computed the heat fluxes (S_{BB}), at the same locations, from FF-RHT theory by treating the membranes as blackbodies. To compare these two heat fluxes we show in Figure 3-5a the Heat Flux Enhancement Ratio (HFER = $S_{\text{FED}}/S_{\text{BB}}$, see Figure B-5 for more details) for

membranes of three thicknesses (others shown in Figure B-8). It can be seen that, for the thinnest membranes, HFER peaks sharply in the in-plane direction, with a value that is more than 10 times larger than the blackbody limit. In contrast, the out-of-plane Poynting flux is significantly attenuated below the blackbody limit. However, this behavior is not observed for the thickest structures, whose emission and absorption characteristics are very similar to those predicted by FF-RHT theory.

Next, we computed the absorption cross-sections (σ_{FED}) using SCUFF-EM, as a function of the polar angle θ' (see Figure 3-5a), and compared them to the absorption cross-sections (σ_{BB}) from FF-RHT theory by treating the membranes as blackbodies (see Figure B-6). The computed Absorption Cross-section Enhancement Ratio (ACER = σ_{FED}/σ_{BB}) is shown in the bottom of Figure 3-5a. It can be seen that ACER has a similar polar angle dependence as HFER. In order to evaluate if the enhancements in HFER and ACER account for the enhanced heat transfer rates we also computed the heat transfer rates (Q_{FED}) between adjacent membranes (20 μm gap) using FED and estimated the enhancement in comparison to the blackbody limit (Q_{BB}) for various membrane thicknesses. We show in Figure 3-5b the ratio of Q_{FED} to Q_{BB}. It can be seen that this ratio is much larger for thinner devices than thicker ones (where the ratio is ~1). Further, we find that the experimentally measured enhancements are similar to those predicted by taking the product of HFER and ACER, thus showing that the observed enhancements in RHT are significantly accounted for by the enhanced absorption cross-section. Additional analysis performed by us on Au membranes (see Figure B-9, Figure B-10) demonstrates that dramatic enhancements can also be obtained by very thin metallic structures, for reasons similar to those described above. We also note that the ~100-fold enhancements in radiative heat transfer relative to FF-RHT theory that were experimentally observed by us persist

as the gap-sizes increase to the millimeter range as confirmed by additional computations and experiments presented in the SI (see Figure B-17 and Figure B-18).

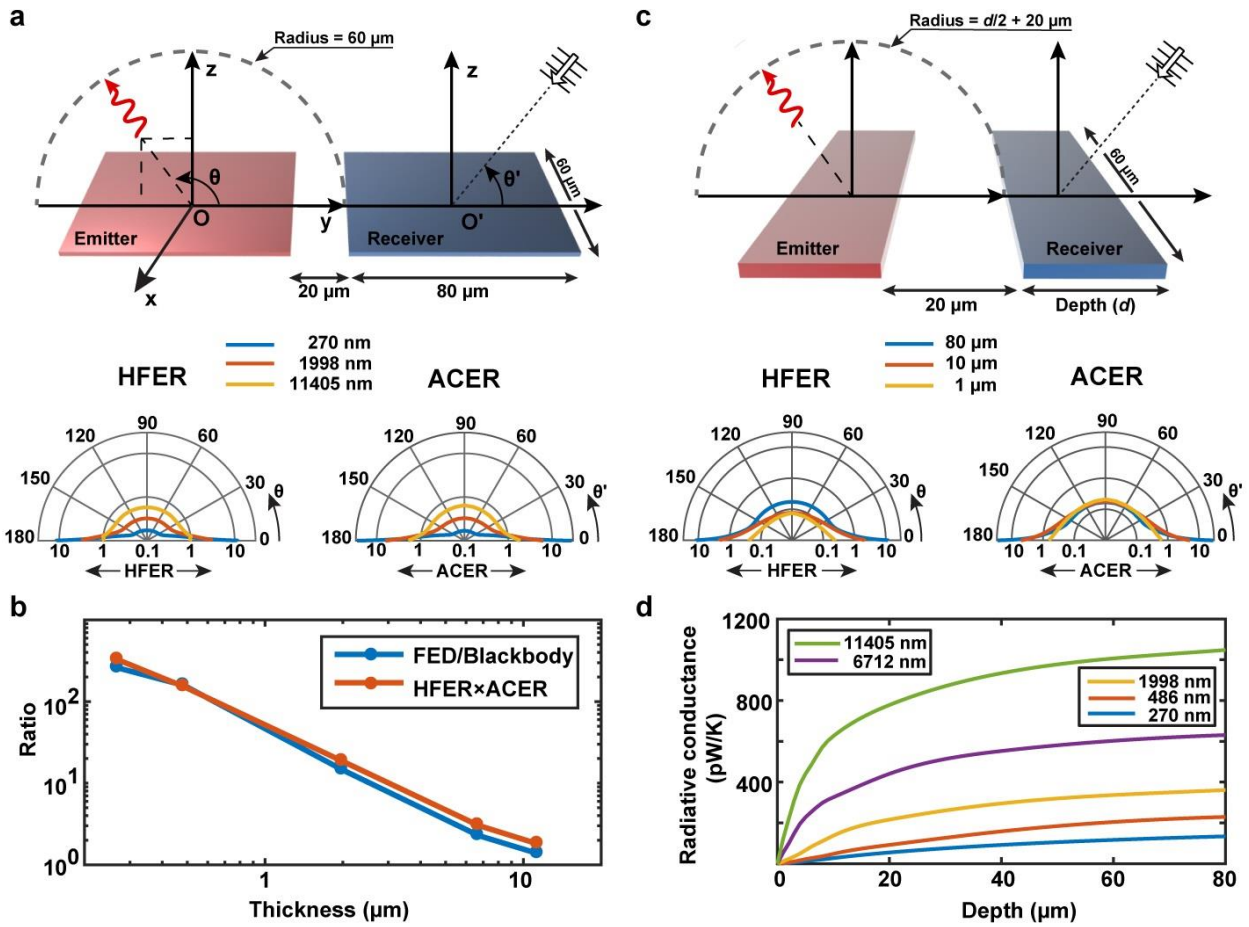

Figure 3-5. Analysis of the observed violations of the blackbody limit. (a) Simplified geometry of membranes (excluding beams) employed in the analysis of the emissions and absorption. The lateral dimensions are kept constant but the thickness of membranes is varied in the calculations. Bottom panel (left) shows the computed Heat Flux Enhancement Ratio (HFER) as a function of the polar angle θ (at a fixed azimuthal angle and a distance of 60 μm from the origin *O*). Computed angle-dependent Absorption Cross-section Enhancement Ratio (ACER) is also shown in the bottom right panel. It can be seen that HFER and ACER are dramatically larger in the in-plane direction for the thinnest devices. Additional calculations of HFER at larger distances are shown in Figure B-7. (b) The ratio of the radiative thermal conductance computed from FED to that of FF-RHT theory is shown along with the product of HFER and ACER. (c) Computed HFER and ACER for 270 nm thick membranes as a function of polar angle, for various depths (*d*) at a fixed distance of *d*/2 + 20 μm from the volumetric center of the membrane. (d) Computed radiative conductance ($G_{rad,\,eff}$) for the configurations considered in panel c. It can be seen that the radiative $G_{rad,\,eff}$ decreases with decreasing depth.

Finally, to understand the dependence of the RHT on the depth of the membranes, we computationally analyzed the HFER and ACER for 270 nm thick, 60 μm wide membranes, while the depth was systematically reduced (Figure 3-5c). The computational results suggest that, as the depth is decreased, HFER and ACER become progressively smaller. We performed FED-based calculations to understand the dependence of radiative conductance on the membrane depth. The obtained results (Figure 3-5d) show that the radiative conductance decreases rapidly with decreasing depth highlighting that the depth plays a critical role in the observed enhancements.

3.4 Conclusion

Our experiments provide the first direct evidence that the blackbody limit can be overcome by orders of magnitude in the far-field. These results represent a significant advance over past experimental work where enhancements compared to the blackbody limit have only been observed in the near-field. Further, our complementary computations provide additional insights into the far-field radiative heat transfer between nanoscale objects in terms of enhanced emissions and absorption cross-sections. This work highlights the potential of employing nano-membranes for enhancing and controlling thermal absorption. Further work on optimizing and enhancing such absorption characteristics may have a dramatic impact on thermal energy capture for thermal to electric energy conversion. Finally, the insights obtained from this work may also bear upon the modelling of planetary atmospheres [130] proto-planetary formation [115] and astrophysical phenomena [131] where thermal radiation plays an important role.

3.5 Methods

Fabrication process for the devices: The fabrication process of the devices is shown in Figure 3-6a. A low-stress silicon nitride (SiN) film, with a nominal stoichiometry given by Si_3N_4

and a thickness (270 nm, 486 nm, 1998 nm), is first deposited onto a silicon wafer that is 500 μm thick (Step 1) via low pressure chemical vapor deposition (LPCVD). A 30 nm-thick Platinum (Pt) film heater-thermometer is then patterned onto the SiN layer using a liftoff process (Step 2). Then, 100 nm thick gold (Au) electrical connections are patterned onto the SiN layer using a similar liftoff process (Step 3). The contour of the suspended membranes and support beams is formed by reactive ion etching (RIE) through the SiN layer on the front side (Step 4). Windows in the SiN layer, located on the back of the wafer, are created by RIE (Step 5), followed by a potassium hydroxide (KOH) etch to create a through-hole in the silicon handle wafer and release the suspended membrane devices (Step 6). In order to create suspended devices with even greater thickness (6712 nm and 11405 nm), the 1998 nm thick devices were symmetrically deposited with 2 – 4 μm thick SiN, via plasma-enhanced chemical vapor deposition (PECVD), on both sides after the release step (Step 7). The thickness of all devices was characterized by spectroscopic reflectometry (resolution ~1 – 2 nm).

Scanning electron microscope (SEM) and optical microscope images of one of the fabricated devices are shown in Figure 3-6b and c, respectively. The suspended membranes are 60 μm × 80 μm in size, and the support beams are each 400 μm long and 2 μm wide (see Figure 3-6).

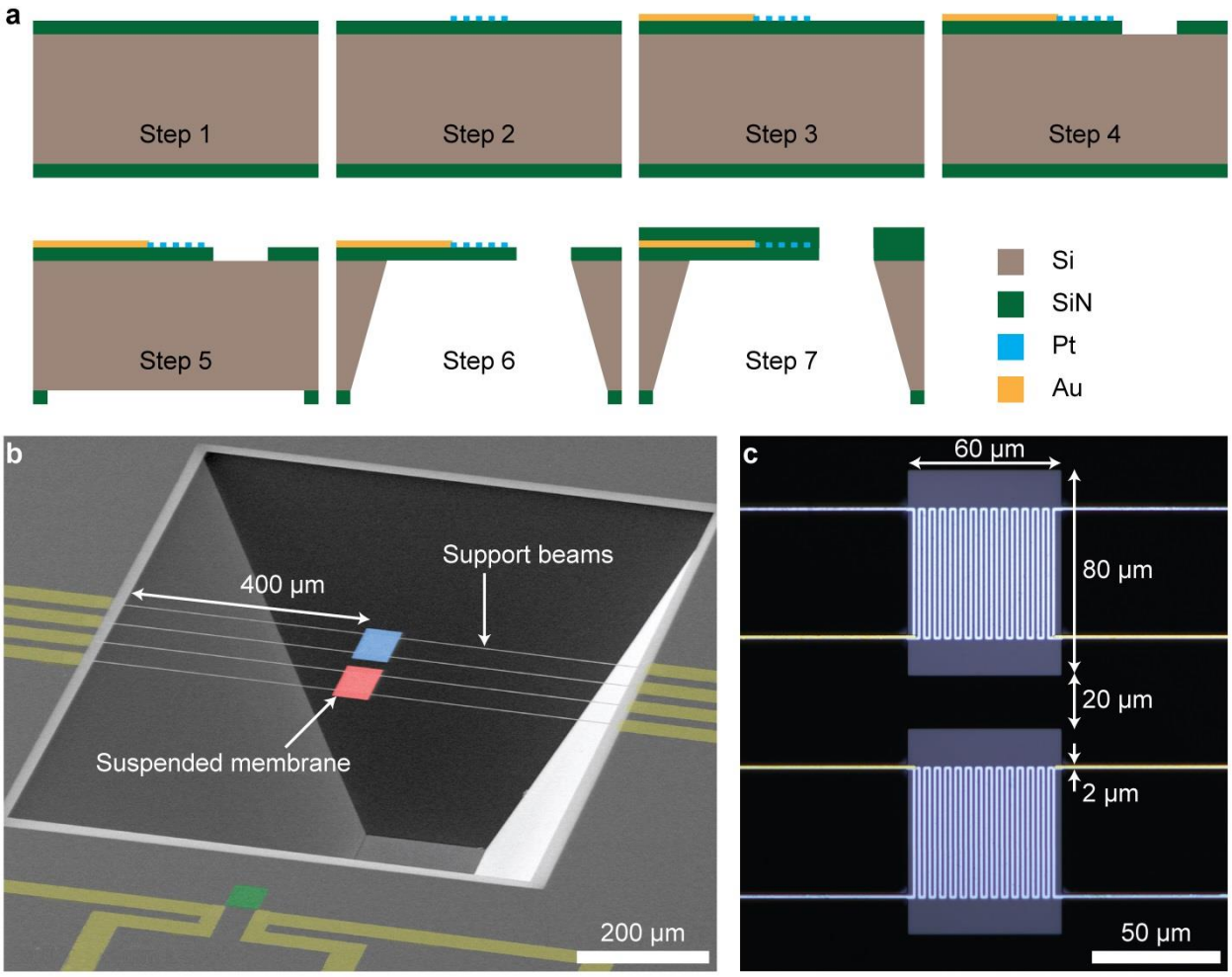

Figure 3-6. Fabrication process for the devices. (a) (1) Deposition of silicon nitride (SiN) layer. (2) Patterning of platinum (Pt) serpentine resistance thermometer. (3) Patterning of gold (Au) leads. (4) Front-side etching of suspended device contour. (5) Etching of window in SiN on backside. (6) Potassium hydroxide (KOH) etching of silicon handle to release suspended devices. (7) Optional deposition of plasma-enhanced chemical vapor deposition (PECVD) SiN onto suspended 1998 nm-thick devices to create even thicker membranes (6712 nm thick, 11405 nm thick). (b) and (c), Scanning electron microscope and optical microscope images, respectively, showing the geometry of the fabricated devices and relevant dimensions. Au wires (yellow) and suspended membranes (red and blue) were pseudo-colored.

Characterization of the flatness and co-planarity of adjacent membranes: Different versions of the devices were fabricated by changing the membrane thicknesses from 270 nm thick to 11.4 µm. To characterize the emitter membrane and receiver membrane flatness, as well as the co-planarity of the membranes, we performed laser scanning confocal microscopy

(LSCM) on each of the devices. LSCM allowed us to quantify small height variations with a resolution of 60 nm in the vertical direction. The height profile along a line traversing the emitter membrane and receiver membrane is shown in Figure 3-7a-d for 270 nm thick, 486 nm thick, 6712 nm thick, and 11405 nm thick membranes, respectively. As shown in Figure 3-7a-b, the flatness deviates by no more than 150 nm over the 80 μm depth dimension for the two thinnest devices. For the two thicker devices shown in Figure 3-7c-d, deviations from flatness can be as large as 400 nm over the 80 μm depth dimension due to film stresses in the additional PECVD SiN layers deposited on these devices (see fabrication description). Compared to the thickness of the membranes, the relative flatness (deviation from planarity/film thickness) of the two thickest devices is better than that of the two thinnest devices. Moreover, as discussed in the Appendix (see Figure B-15, Figure B-16), our analysis shows that small deviations from planarity have negligible impact on the radiative heat transfer (RHT). Therefore, the large exceedances in comparison to basic far-field RHT theory observed by us are not due the small imperfections in our devices.

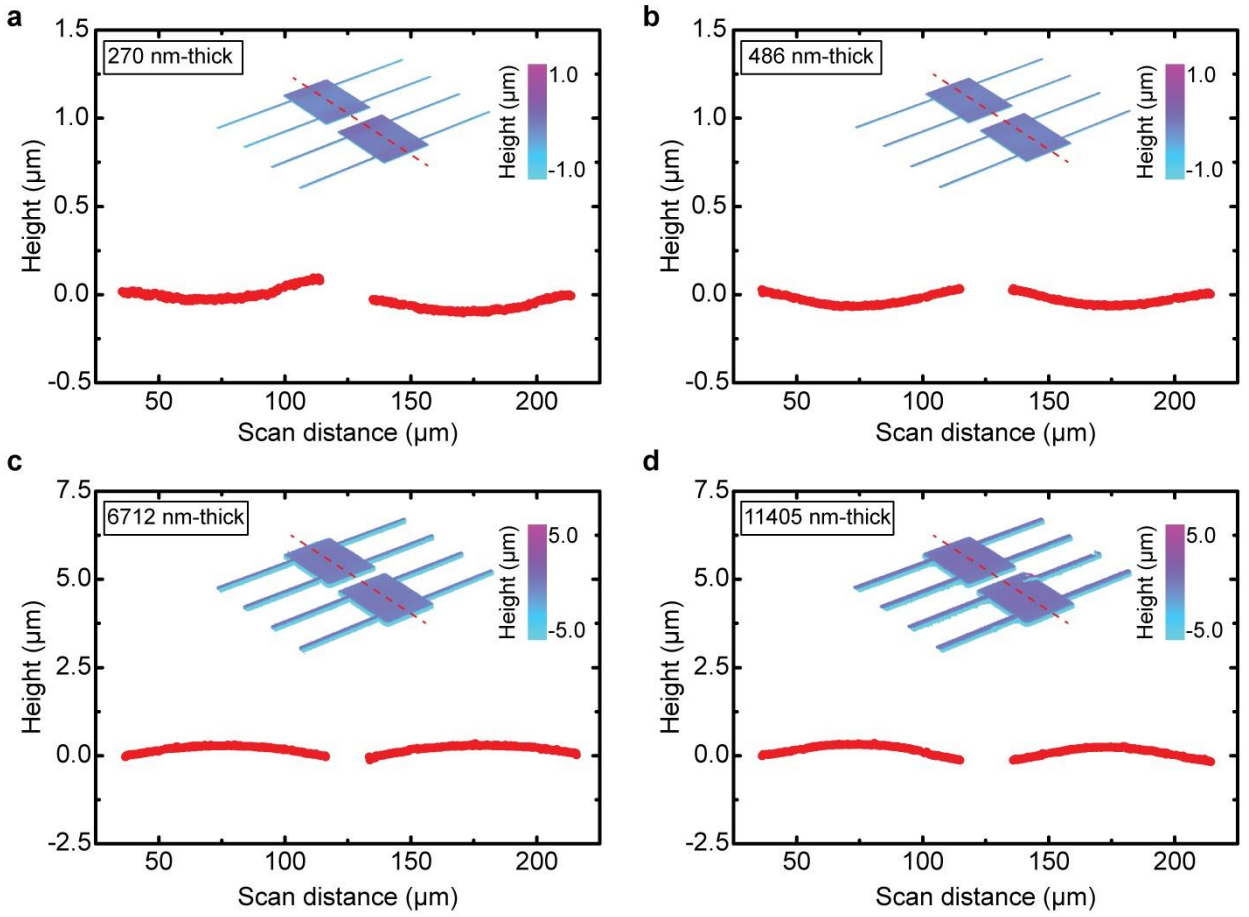

Figure 3-7. Characterization of the flatness and co-planarity of adjacent membranes. Data from laser scanning confocal microscope scans across adjacent membranes showing the flatness of (a) 270 nm thick, (b) 486 nm thick, (c) 6712 nm thick, and (d) 11405 nm thick membranes. Line profiles were taken over the red dashed line indicated in the surface plots shown in the insets.

Characterization of the electrical and thermal properties of the devices: Knowledge of the temperature coefficient of resistance (TCR) of the integrated platinum resistance thermometer (PRT), the thermal frequency response of the device, the beam thermal conductance, and the noise floor of the measurement scheme is crucial for accurate quantification of the radiative exchange between the adjacent membranes. These characterization experiments were performed inside a cryostat (Janis ST-100), which was evacuated to ~10^{-6} Torr using a turbo-molecular pump.

Temperature coefficient of resistance (TCR): The resistance (R) of the integrated PRT was measured by passing a small AC current of amplitude I_f = 1 μA (frequency f = 101 Hz) through the device, resulting in negligible heating. The 1f-component of the voltage signal across the PRT (V_f) was measured with a lock-in amplifier (bandwidth ~78 mHz) by using a 4-probe scheme and the resistance of the PRT was calculated as $R = V_f/I_f$. A representative plot of the resistance measured at various temperatures is shown in Figure 3-8a (see inset showing schematic of measurement scheme). We note that a commercial PID temperature controller was used to maintain the temperature of the cold finger of the cryostat to within ±10 mK of a fixed setpoint during experiments at each temperature. The slope of the best-fit line through these data points is used to find the TCR, which can be calculated at each temperature using $\alpha(T) = \frac{1}{R(T)}\frac{dR}{dT}$. At room temperature, the TCR was found to be ~$1.80 \pm 0.03 \cdot 10^{-3}$ K^{-1}.

Thermal frequency response: To characterize the frequency response of the devices, the suspended membrane of each of the devices employed in the experiments was heated by passing a sinusoidal current of fixed amplitude I_f through the integrated PRT. This sinusoidal current produced Joule heating of the membrane at a frequency 2f, which correspondingly resulted in temperature oscillations of the suspended device at frequency 2f and amplitude ΔT_{2f}. The voltage oscillation across the PRT at frequency 3f (V_{3f}) was measured using a SRS 830 lock-in amplifier (lock-in bandwidth ~3 mHz). The amplitude of temperature oscillations was determined from $\Delta T_{2f} = 2V_{3f}/I_f R\alpha$. The measured ΔT_{2f} as a function of frequency is shown in Figure 3-8b for devices of various thicknesses. Note that the AC temperature response ΔT_{2f} was normalized to the values obtained at low frequencies, which were ~1 K for each device (achieved by suitably adjusting the current I_f). It can be seen that the cut-off frequency is dependent on device thickness, and there is negligible attenuation below ~1 Hz for the three thinnest devices and ~0.3

Hz for the thickest two devices. At low temperatures, the thermal cut-off frequency was found to shift slightly to higher frequencies.

Beam thermal conductance: To determine the thermal conductance of the beams that support the suspended membrane devices, a large AC current (amplitude, I_f) was supplied through the integrated PRT at a fixed frequency *f*, which was selected to be below the thermal cut-off frequency of the device to ensure a full thermal response. The temperature modulation amplitude ΔT_{2f} was found from the 3*f*-component of the voltage across the PRT, as described previously. The modulated heat input was estimated as $Q_{2f} = I_f^2 R_{\text{tot}}/2$. Here, R_{tot} is the total electrical resistance of the integrated PRT and the current carrying leads on the beams. The current carrying leads were found to have a small resistance ~100 Ω, compared to the resistance of the PRT (~10 kΩ) and hence heating in the beams has negligible contributions to the heat input into the membrane . Figure 3-8c shows the amplitude of temperature oscillations ΔT_{2f} as a function of the heating power Q_{2f}. The inverse of the slope of the best-fit line through these data points provides the thermal conductance of the beams. As expected, the thermal conductance depends on the thickness of the beams, and at room temperature, ranges from ~80 nW/K for the thinnest device (270 nm thick) to ~1 μW/K for the thickest device (11.4 μm thick). The thermal conductance falls at lower temperatures due to the temperature-dependent thermal conductivity of silicon nitride. We note that for the thinnest devices there are significant contributions to the thermal conductance from the metal lines integrated into it (~75%). We also note that for the thickest two devices we have two different kinds of SiN (LPCVD and PECVD), whereas for the three thinner devices we only used LPCVD SiN. Past work has [132, 133] suggested that PECVD SiN has a lower thermal conductivity than the LPCVD SiNs, which partly explains why the thermal cutoff frequency is lower for the two thicker devices.

Measurement of $G_{\text{rad, eff}}$: The effective radiative conductance between the adjacent membranes was measured by first applying a large AC current (amplitude, I_f) through the integrated PRT of the emitter membrane. The frequency of the ac current was selected to ensure a full thermal response of the device (i.e. f was chosen to be well below the cut-off frequency for each of the devices). The temperature modulation amplitude of the emitter membrane $\Delta T_{\text{emit, } 2f}$ was found from the $3f$- component of the voltage across the PRT, as described previously. The resulting radiative heat flow ($Q_{\text{rad, } 2f}$) to the receiver membrane produced a modulated temperature rise ($\Delta T_{\text{rec, } 2f}$) of the receiver membrane. A DC current (amplitude I_{DC}) was supplied through the PRT on the receiver membrane and the $2f$- component of the voltage across the PRT (V_{2f}) was used to calculated the temperature modulation amplitude by $\Delta T_{\text{rec, } 2f} = V_{2f} / I_{\text{DC}} Ra$. A lock-in amplifier was used to detect V_{2f} with a bandwidth of 0.78 mHz to reduce noise. More specifically, $\Delta T_{\text{emit, } 2f}$ and $\Delta T_{\text{rec, } 2f}$ (e.g. shown in Figure 3-2a and Figure 3-8d) were obtained by measuring the lock-in output every 2 seconds 1500 times and computing the mean of the data. Error bars for $\Delta T_{\text{emit, } 2f}$ and $\Delta T_{\text{rec, } 2f}$ were found by obtaining the standard deviation of the same data. The measured values for $G_{\text{rad, eff}}$ plotted in Figure 3-2 and Figure 3-4 were determined by recording $\Delta T_{\text{rec, } 2f}$ for various values of $\Delta T_{\text{emit, } 2f}$ and calculating the slope of the linear regression line to this data (representative plot shown in Figure 3-2a). Finally, the effective radiative conductance between the membranes is obtained from:

$G_{\text{rad, eff}} = G_{\text{beams}} \Delta T_{\text{rec, } 2f} / (\Delta T_{\text{emit, } 2f} - \Delta T_{\text{rec, } 2f})$, whereas the error bars for $G_{\text{rad, eff}}$ were estimated from the uncertainty in the slope of the linear model described above.

Noise floor of the measurement scheme: To estimate the noise floor of the measurement scheme, the emitter membrane was Joule heated with progressively lower powers, and for each power $\Delta T_{\text{emit, } 2f}$ and $\Delta T_{\text{rec, } 2f}$ were simultaneously measured using the procedure described

previously. Representative data is shown in Figure 3-8d for a 2 μm thick device at 100 K where f was chosen to be 0.5 Hz, the bandwidth was 0.78 mHz and I_{DC} = 10 μA (lower temperature represents the more challenging scenario as the radiative conductance is smaller). It can be seen that $\Delta T_{rec,\,2f}$ decreases linearly for decreasing $\Delta T_{emit,\,2f}$. When $\Delta T_{emit,\,2f}$ is less than ~1 K, the signal measured by the receiver becomes noise limited: i.e. for progressively smaller temperature rise of the emitter membrane, the measured temperature rise of the receiver membrane never falls below 60 μK, which represents noise equivalent temperature (*NET*). Similar experiments performed at other temperatures reveal that the NET falls into the range of 25 μK - 70 μK depending on the choice of the modulation frequency and the magnitude of the DC sensing current I_{DC}. By knowing the *NET* and the beam thermal conductance of each device, we could estimate the heat flow resolution by $Q_{res} = G_{beams} \times NET$ at any given temperature. We used this estimation of the heat flow resolution to ensure that none of the measurements of the effective radiative conductance were noise limited. Typically, this required us to set $\Delta T_{emit,\,2f}$ to be ~5 – 10 K.

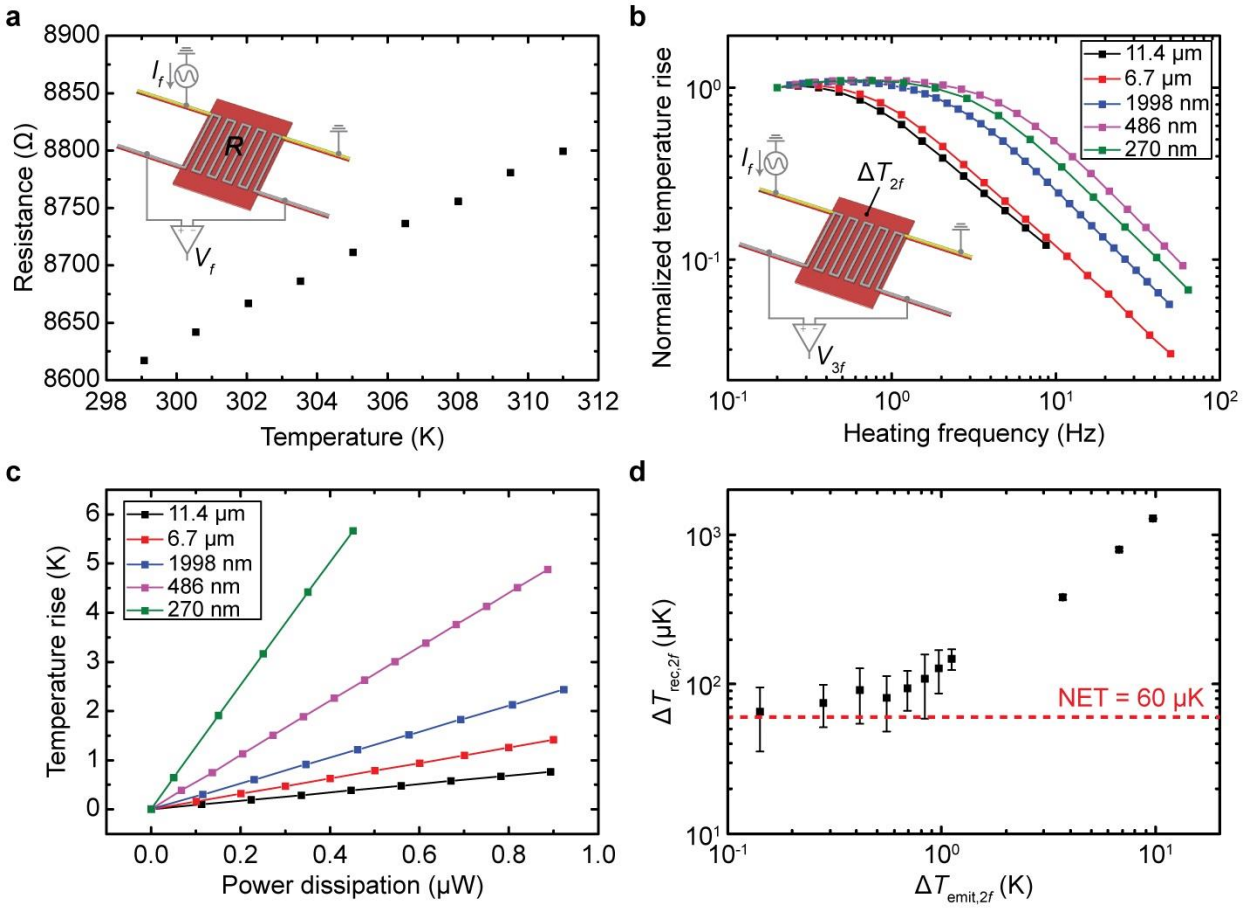

Figure 3-8. Characterization of the electrical and thermal properties of the devices. (a) Temperature dependence of the resistance of the integrated platinum resistance thermometer (PRT) near room temperature. The inset shows a schematic of the measurement scheme used for the resistance characterization. (b) Thermal frequency response of membrane devices with various thicknesses measured at T = 300 K. The inset depicts a schematic of the measurement scheme employed for these tests. (c) Temperature rise of the membrane as a function of the Joule heating in the PRT, measured at T = 300 K for devices of various thickness. (d) Temperature rise of the receiver membrane as a function of the temperature increase of the emitter membrane for a 2 μm thick device at 100 K. The noise equivalent temperature is ~60 μK for a temperature modulation frequency of 0.5 Hz and a measurement bandwidth of 0.78 mHz and I_{DC} = 10 μA.

Control experiments: To rule out that transport mechanisms other than far-field radiation or measurement artifacts contribute to the reported conductances, we conducted several control experiments. Such parasitic coupling mechanisms between the membranes may include conduction through residual air molecules inside the cryostat chamber, conduction through the Si

handle substrate into which the membranes are embedded, radiative exchange between the membranes that is mediated by reflections from various surfaces within the vacuum chamber, and capacitive or inductive coupling of the AC current being passed through the Pt heater on the emitter membrane to the Pt lines on the receiver membrane.

Conduction through residual air molecules: A simple analysis based on the kinetic theory of gases suggests that, at this pressure, energy exchange between the membranes due to conduction through residual air molecules is negligible compared to the radiative coupling measured by us. To experimentally verify this prediction, we measured $G_{\text{rad, eff}}$ at two different pressures (10^{-6} Torr and 10^{-3} Torr). Since conduction through air molecules is proportional to the pressure [134], increasing the pressure from 10^{-6} Torr to 10^{-3} Torr should result in a 1000-fold increase in this exchange mechanism. Thus, if parasitic conduction through molecules had significant contributions to $G_{\text{rad, eff}}$ at 10^{-6} Torr, then at 10^{-3} Torr we should have measured a large increase in the effective conductance between the emitter and receiver. Instead, we found no measurable increase. Results from measurements on one device featuring 2 μm thick membranes (Figure 3-9a), demonstrate that the measured conductance is independent of vacuum level for pressures between 10^{-3} Torr and 10^{-6} Torr. This pressure independence was confirmed for cryostat temperatures from 80 K to 300 K, suggesting that conduction through residual air molecules at 10^{-6} Torr is indeed negligible in all our experiments and can be ignored.

Conduction through handle substrate: All device structures were fabricated from thin-film SiN deposited on a silicon handle wafer (500 μm thick), hence one could envision a *scenario* where heat from the emitter membrane conducts out through the support beams, through the silicon handle wafer, and into the receiver membrane through its support beams, producing a measurable signal that could be misinterpreted as a radiative gap conductance (see

inset of Figure 3-9b). To test this hypothesis, a set of membranes was fabricated with short support beams (150 μm long instead of 400 μm long). We expected that an increase in the measured gap conductance between these short-beam devices compared to the gap conductance between devices with longer beams would signal a non-negligible energy exchange via conduction through the substrate. However, as shown in Figure 3-9b, it was found that the gap conductance measured between these short beam devices is essentially equal to that measured for the devices with 400 μm long beams. This control experiment verifies that conduction through the Si handle substrate negligibly contributes to the measured gap conductance and cannot account for the orders-of-magnitude enhancements in gap conductance that are measured.

Demonstration of Radiative Coupling: In order to further confirm that heat transport from the emitter to the receiver is completely dominated by direct radiative heat transfer from the emitter to the receiver we prepared disconnected emitter and receiver devices by cleaving the original (paired) devices (membrane thickness of 2 μm) in the middle. Next, we placed a separated emitter at a distance of ~1 mm from a single receiver (see Figure 3-9c). Confocal microscopy was performed to ensure that the devices were coplanar with each other. Next, a thin shim of reflective aluminum foil (thickness 24 μm) was placed in the gap between the adjacent membranes, blocking direct radiative exchange between them but allowing any possible radiative exchange via reflections from the top side (see inset of Figure 3-9d) and conduction through the underlying support structure. As shown in Figure 3-9d, with the aluminum shim in place, the measured coupling signal between the membranes is completely blocked (red). For membranes separated by the same gap distance but without the aluminum foil shim in place (black), there is a linear increase in the temperature of the receiver membrane as the temperature of the emitter membrane is raised. This control test conclusively illustrates that heat transfer between

membranes is completely dominated by direct radiative heat transfer from the emitter to receiver device. We also note that in all our experiments, devices were mounted over a Metal Velvet^{TM} coated foil, which has a hemispherical reflectance <4% for wavelengths <14 μm. Further, the inner surface of the radiation shield of the cryostat, which the membranes "see" on the top side, was also coated with Metal Velvet^{TM} foil. As verified by COMSOL (and the above described control experiment), such a mounting scheme effectively eliminates radiative coupling via reflections from the cold finger surface and the radiation shield.

Proof of negligible coupling via Capacitive/Inductive effects or via reflection of radiation: For each measurement of the effective radiative conductance between the emitter and receiver devices, the temperature of the emitter membrane is modulated by providing an AC current to the integrated Pt heater. Any capacitive coupling [135] between the Pt lines on the emitter device and Pt lines on the receiver device due to this AC current, and its harmonics, could potentially produce spurious signals that may be misinterpreted as the radiative conductance signal. Control experiments were performed to quantify the magnitude of this capacitive coupling. In these experiments we took advantage of the fact that the suspended devices used in the experiments were fabricated on a 10 mm × 10 mm silicon handle chip and each chip had four emitter/receiver pairs separated by 20 μm gaps, with each pair suspended in a separate through-hole in the handle chip (see Figure 3-9e showing two emitter/receiver pairs in separate through-holes). To quantify contributions from capacitive coupling, we used an emitter device from one pair of devices and a receiver device from a second pair of devices (see Figure 3-9e). In this configuration, direct radiative exchange between the emitter and receiver is blocked, but capacitive coupling between these non-adjacent devices is still possible because the electrical leads and contact pads on the handle substrate are in close proximity. As shown in

Figure 3-9f, the coupling signal between the non-adjacent devices in separate through-holes (red dots) is extremely small and is noise-limited. For comparison, the coupling signal between adjacent devices separated by a 20 μm gap (black squares) is shown to be readily measurable. This control test verifies that capacitive coupling between adjacent membranes is indeed negligible. Further, since there is no measurable coupling between the emitter from the first pair and the receiver on the second pair, one can also conclude that any radiative coupling via reflections within the cryostat is also negligible.

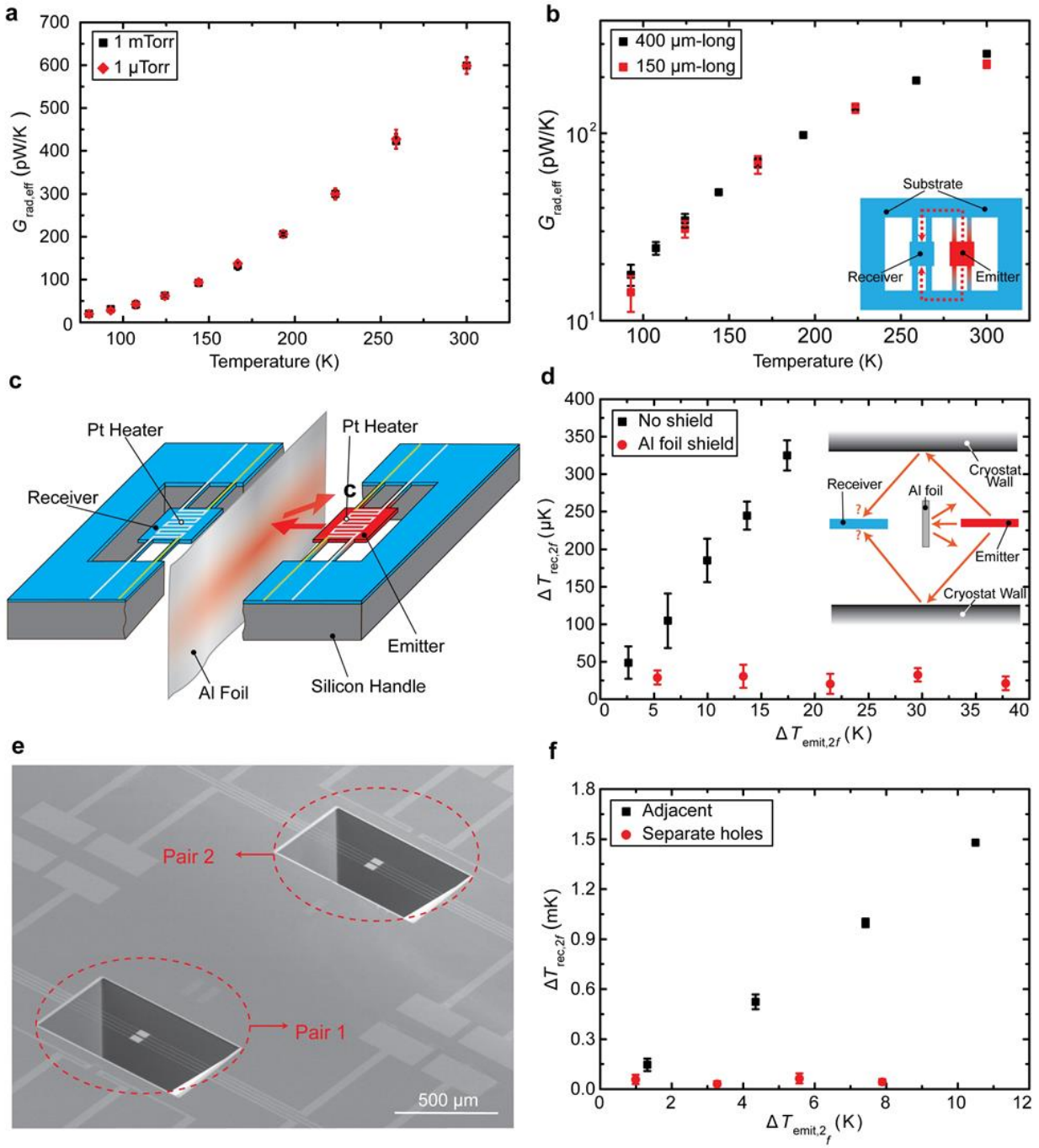

Figure 3-9. Quantification of parasitic energy transfer mechanisms. (a) Measured $G_{rad,\,eff}$ between 2 μm thick SiN membranes at various temperatures and pressures. Measurements performed at 10^{-3} Torr (black squares) and 10^{-6} Torr (red diamonds) are virtually identical, strongly supporting the expectation that conduction via remaining gas molecules plays no role. (b) Measured $G_{rad,\,eff}$ between 270 nm thick SiN membranes at various temperatures. The inset illustrates a hypothesis of how thermal energy between the devices can potentially couple via conduction through the substrate. The plotted data compare two device geometries: devices with 400 μm long support beams (black squares) and devices with 150 μm long support beams (red squares). Since devices

with short and long beams have identical $G_{rad,\,eff}$ it is clear that coupling via the suspending beams is negligibly small. (c) Schematic describing the control experiment where an emitter and a receiver are separated by an ~1 mm gap and an Al foil is placed between them blocking direct radiative heat transfer (not drawn to scale and proportion). (d) The measured coupling signal between 2 μm thick emitter and receiver membranes across a 1 mm wide gap (T = 300 K). Signals with (black squares) and without (red dots) an Al foil in the gap are shown. The inset (cross sectional view of the devices) illustrates how the Al foil shield blocks direct RHT between the membranes but potentially allows RHT via specular reflections. Since the signal in the presence of the Al blocker represents the noise floor of our measurement, we conclude that there is negligible heat transfer (via RHT or otherwise) in the presence of the Al foil. This control experiment provides unequivocal evidence that energy transfer between the membranes is exclusively mediated by direct radiation. (e) SEM image of two emitter and receiver pairs suspended in separate through-holes on the same handle substrate. (f) The measured coupling signal between 486 nm thick devices (T = 100 K). Signals from adjacent emitter and receiver devices (i.e. in the same through-hole, see pair 1 in panel e) with a 20 μm gap separation (black squares) are compared to signals when emitter and receiver devices are suspended in separate through-holes on the same silicon handle substrate (red dots).

Computational Methods: Calculations of radiative heat transfer in the framework of FF-RHT theory were performed using COMSOL Multiphysics (Altasim technologies). Calculations of RHT within the framework of fluctuational electrodynamics were performed using a boundary element method (BEM) [127, 129]. An implementation of this method is available via the open source code SCUFF-EM. More details of the computational methods including mesh sizes and analysis of different materials and structures are provided in the Supplementary Information.

Chapter 4 A Novel Scheme to Gate Radiative Heat Currents

Reproduced with permission from reference [100]:

Dakotah Thompson, Linxiao Zhu, Edgar Meyhofer and Pramod Reddy, (In Preparation), (2018).

4.1 Abstract

The ability to actively gate heat currents is a challenging and still largely unresolved problem, in contrast to the electronic analog which is now routine [136]. In this work, we demonstrate a novel scheme to actively gate the radiative heat current between two nanostructures in the far-field via mutual interactions with a third nanostructure that is in close proximity. Our modelling indicates that guided modes supported in the nanostructures can be modified by the third nanostructure if it is sufficiently close, and this evanescent interaction is responsible for the gating of the far-field radiative heat current. To demonstrate the potential for active gating using this scheme, we modulate the radiative heat current by a factor of 5 with a period of two minutes. The insights from this work could potentially enable technological advances in a number of fields where controlling radiative heat transfer is essential.

4.2 Introduction

It has been shown recently [12, 25, 37] that the radiative heat current between two bodies can be dramatically controlled by the presence of evanescent modes, which can tunnel though the vacuum gap between the bodies when they are in the near-field, i.e. gap separation smaller

than the peak thermal wavelength (λ_{Th} ~10 μm at room temperature). Indeed, the number of channels through which these evanescent modes can tunnel increases nonlinearly as the gap size is reduced, allowing orders of magnitude enhancements in the heat flux to be achieved by reducing the gap to the nanometer range [98]. There have been subsequent proposals to actively enhance or suppress near-field radiative heat transfer (NFRHT) between two bodies by leveraging this nonlinear behavior, including applying external electric and magnetic fields to the system [51, 53], utilizing phase change materials [50, 77, 137, 138], and leveraging the mutual interaction with a 3rd body in close proximity [139-142].

Such active control of radiative heat currents in the far-field, for gap separations larger than the peak thermal wavelength λ_{Th}, is not available. In contrast to NFRHT, far-field radiative heat transfer (FFRHT) occurs via propagating modes, and is spectrally broadband while lacking the sharp dependence on gap size [8]. So, methods to actively modify radiative heat currents between two bodies in the far-field rely on changing the view factor between them, which is typically accomplished with a radiation shield. What has not been explored, however, is the ability to gate the far-field heat current between two nanostructures, for which geometrical optics does not apply. Leveraging the unique optical properties of such nanostructures to effectively gate radiative heat currents in the far-field could enable technological advances in thermal management [116], thermal lithography [81, 85-87], infrared imaging and spectroscopy [84, 143-145], and energy conversion [58, 59, 70, 146], especially pyroelectric energy conversion which requires modulated heat currents to generate electrical power.

4.3 Experiments, Results and Analysis

In this work, we demonstrate a novel scheme to gate the radiative heat current between two coplanar nano-membranes in the far-field. Recently, it was shown [99] that the FFRHT

between two dielectric membranes with sub-wavelength thickness is enhanced by orders-of-magnitude compared to the Stefan-Boltzmann limit due to the large in-plane absorption cross-section of the membranes (Figure 4-1a). Here, we demonstrate that the heat transfer $Q_{1\text{-}2}$ between two such nano-membranes can be actively gated by simply adjusting the spatial offset d of a 3rd membrane that is parallel to the two original membranes (Figure 4-1b). To demonstrate this gating scheme, we fabricated a device featuring two coplanar silicon nitride (SiN) membranes (denoted the "emitter" and "receiver", see Figure 4-1c), each with a thickness of 486 nm, separated by a fixed distance of g = 20 μm. These suspended membranes, which are supported by long beams affixed to a silicon handler chip, each features an integrated platinum resistance thermometer (PRT) that is used to either resistively heat the suspended membrane or measure its temperature rise. We fabricated a second device on a separate handler that features a doubly-clamped silicon nitride (SiN) cantilever (denoted the "modulator", see Figure 4-1d) with a large footprint and a thickness of 524 nm (see Figure 4-5 for fabrication details). After placing these devices in a high vacuum environment and orienting them as shown schematically in Figure 4-1e, we parallelized them and adjusted the gap d between them using a custom-built nanopositioner (reported in detail elsewhere [105]). It should be noted that the modulator membrane is elevated above its handler substrate by 10 μm, ensuring that the top and bottom handler chips do not interfere with one another during the parallelization procedure. Also, the modulator, emitter, and receiver membranes were found to be extremely flat as indicated by laser scanning confocal microscopy (see Figure 4-6 for flatness characterization).

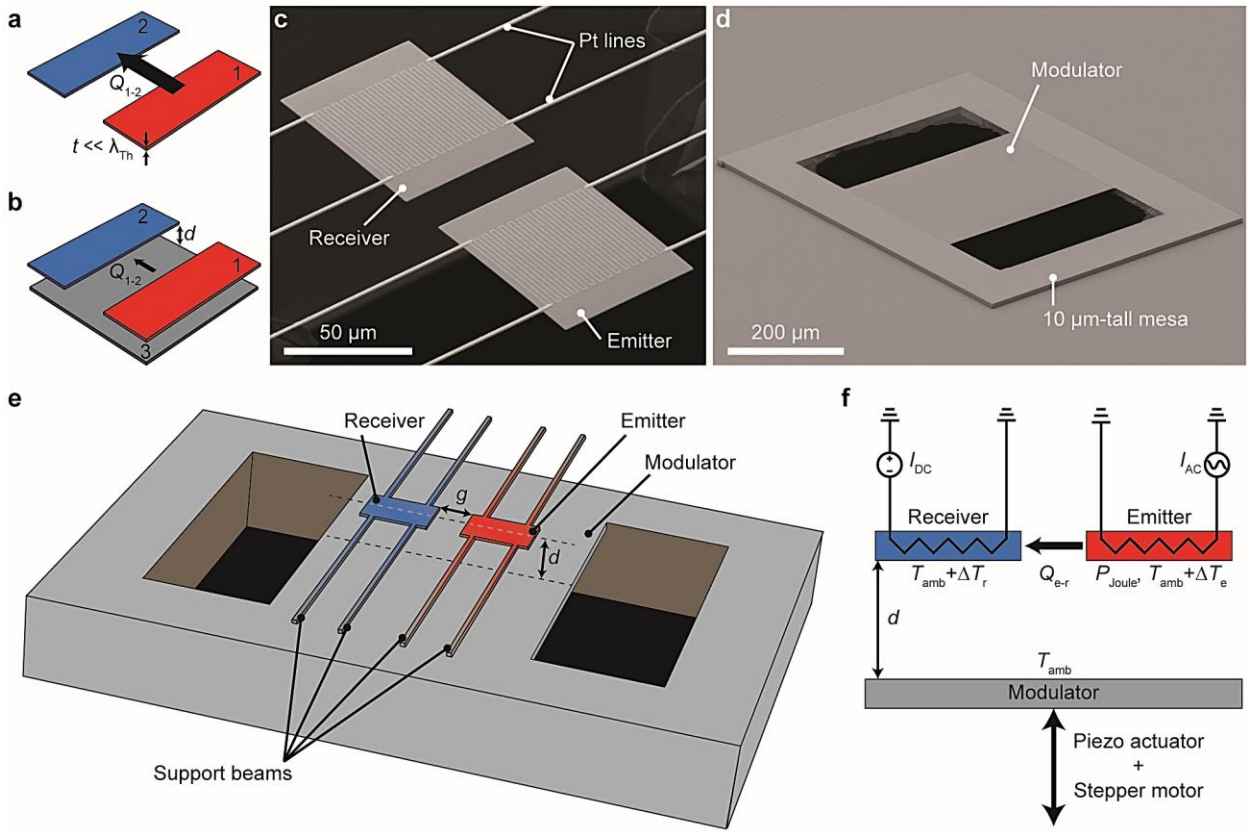

Figure 4-1. Experimental platform to demonstrate gating of radiative heat currents. (a) Schematic depicting large radiative heat transfer rate $Q_{1\text{-}2}$ between two nano-membranes (1 and 2) with sub-wavelength thickness t. Red indicates a hotter temperature and blue indicates a colder temperature. (b) Schematic illustrating how $Q_{1\text{-}2}$ is suppressed by introducing a third membrane (3) with a fixed gap separation d. (c) Scanning electron micrograph (SEM) of nanofabricated device comprised of two co-planar silicon nitride membranes (emitter and receiver) with integrated platinum lines. (d) SEM of doubly-clamped silicon nitride nano-membrane (modulator). (e) Rendering depicting the orientation of the emitter, receiver, and modulator during the experiment. Here, support beams of receiver and modulator are shown but the handler substrate is not. (f) Schematic side view depicting the experimental procedure. The modulator membrane is passively maintained at ambient temperature T_{amb} and its height is adjusted using a piezoelectric actuator and stepper motor in combination. The emitter is Joule heated by an amount ΔT_e, and the radiative heat current to the receiver $Q_{e\text{-}r}$ is found by measuring ΔT_r using the integrated platinum resistance thermometer (PRT).

The following procedure, schematically depicted in Figure 4-1f, was adopted to quantify how the radiative heat current between emitter and receiver depends on the gap d. First, the emitter membrane was isothermally heated by passing a sinusoidal electrical current with a fixed

amplitude of I_{AC} = 14 μA and frequency of 1 Hz through its integrated PRT, resulting in a sinusoidal temperature rise (ΔT_e) with an amplitude ~8.5 K at 2 Hz. The ensuing radiative heat current to the receiver membrane ($Q_{e\text{-}r}$) produced temperature oscillations of the receiver (ΔT_r), which we quantified by passing a fixed DC electrical current I_{DC} = 6 μA to the receiver's PRT and measuring the voltage fluctuations at 2 Hz (see Methods for details of how this temperature rise was measured). The radiative conductance ($G_{e\text{-}r}$) between the emitter and receiver was estimated from $G_{e\text{-}r} = (P_{Joule}/\Delta T_e)\times(\Delta T_e/\Delta T_r - 1)^{-1}$, where P_{Joule} is the power dissipated in the PRT of the emitter membrane. The modulator membrane, which was passively maintained at ambient temperature (T_{amb}), was then systematically displaced towards the emitter/receiver pair in precise steps as small as 232 nm using a feedback-controlled piezoelectric actuator. A stepper motor was used in combination with the piezoelectric actuator to extend the range of travel. A time trace of this approach process is depicted in Figure 4-2a. For each vertical gap separation *d* between the modulator and emitter/receiver (Figure 4-2a, top panel), the values of ΔT_e and ΔT_r were simultaneously recorded (Figure 4-2a, middle panel and lower panel, respectively). From these recorded values, the radiative conductance between the emitter and receiver $G_{e\text{-}r}$ could be quantified as a function of gap separation *d*, until contact was established. As shown in Figure 4-2a (middle and lower panels), contact between the modulator and emitter/receiver pair was indicated by a simultaneous jump in the thermal signals due to conduction through the contact point.

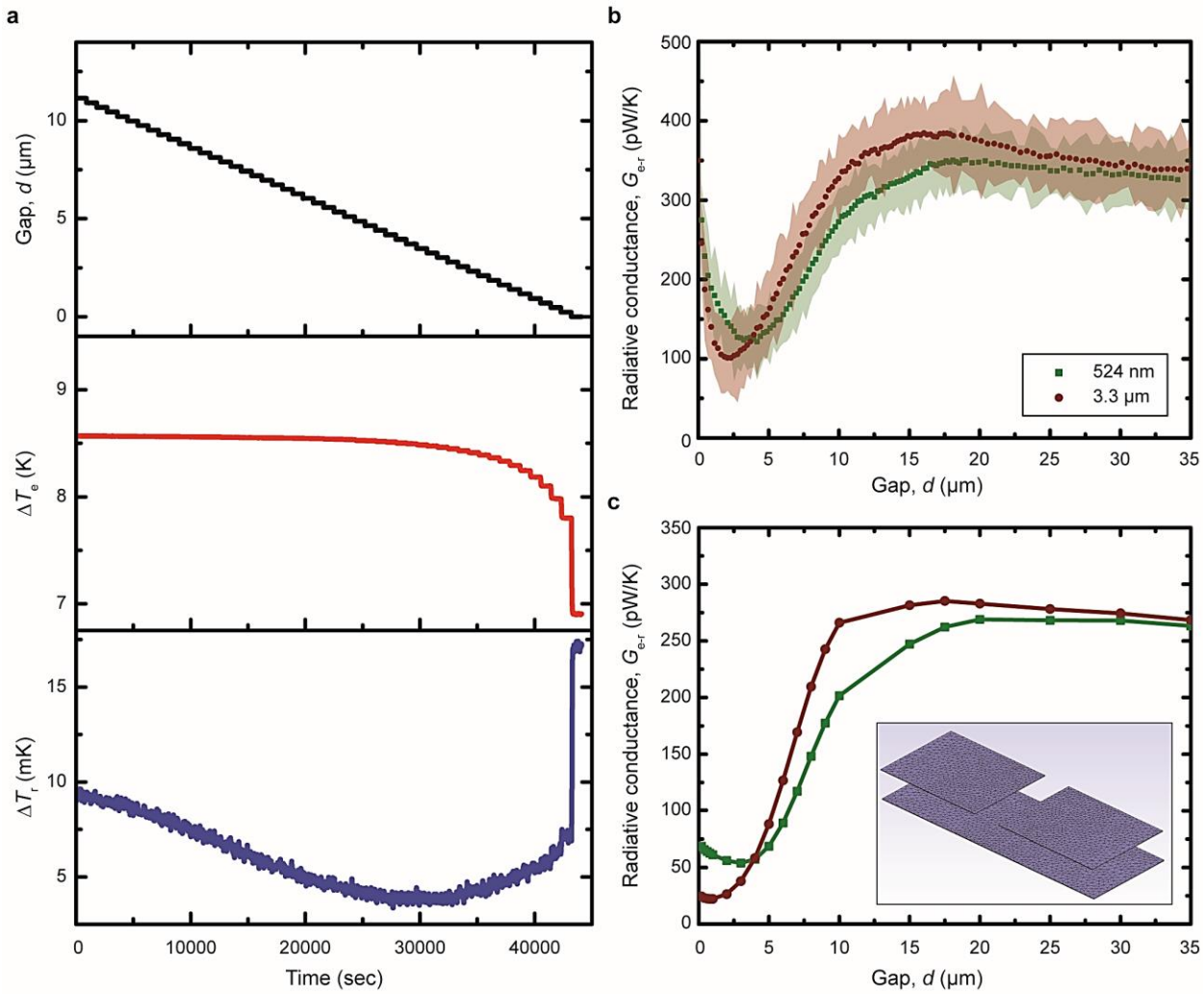

Figure 4-2. Measurement procedure and comparison of experimental results with computational predictions. (a) Raw time series data for the 524 nm-thick SiN modulator. Top: evolution of the gap d during the experiment. Middle: measured temperature rise of the emitter. Bottom: measured temperature rise of the receiver. (b) Measured radiative conductance $G_{e\text{-}r}$ as a function of gap size for the 524 nm-thick (green) and 3.3 μm-thick (brown) SiN modulator. (c) Computed radiative conductance $G_{e\text{-}r}$ for 524 nm-thick (green) and 3.3 μm-thick (brown) SiN modulator. The exact geometry of the model is depicted in the inset. Note that legend from b also applies to c.

The measured $G_{e\text{-}r}$ as a function of gap separation is shown in Figure 4-2b (green curve). For large gap separations greater than 18 μm, the radiative conductance has a value of ~350 pW/K that is largely insensitive to the gap size. As the gap size is reduced below ~18 μm, $G_{e\text{-}r}$ becomes rapidly suppressed, eventually reaching a minimum value of ~125 pW/K at 3 μm. This

experiment demonstrates significant gating of the radiative heat current between emitter and receiver: $G_{e\text{-}r}$ can be suppressed by a factor of ~3 by reducing the gap d from 18 μm to 3 μm. Further insight into this gating scheme was garnered by performing a second experiment where a SiN modulator with a thickness of 3.3 μm was used. For this thicker modulator, improved gating performance was observed as shown in Figure 4-2b (brown curve). Indeed, the thick membrane is able to modulate $G_{e\text{-}r}$ by a factor of ~4 as the gap d is varied between 2 μm and 15 μm. It is interesting to note that the thicker membrane suppresses $G_{e\text{-}r}$ at smaller gap separations than for the original modulator (524 nm-thick). In total, these observed effects offer a glimpse as to how radiative heat currents can be practically gated, though such effects are non-trivial and introduce several questions: Can these results be quantitatively explained? What is the physical explanation for this gating effect? How can the performance of this gating scheme be optimized?

To determine if the observed results can be accounted for under the framework of fluctuational electrodynamics (FED) [11, 12], we developed a FED model of the experimental system using the boundary element method (BEM) [17, 127]. The geometry of our FED model, along with its discretization into small surface elements, is depicted in the inset of Figure 4-2c. The exact geometry of the emitter and receiver membranes is captured in this model, though to keep computations tractable, the support beams and platinum lines are not included. Likewise, the entire lateral dimensions of the modulator are not captured, only the region comprising the footprint of the emitter and receiver (60 μm X 180 μm). It should also be noted that we used the exact dielectric properties of silicon nitride in our FED model, which have been reported in the literature [128]. We then computed the radiative conductance $G_{e\text{-}r}$ as a function of gap size d and the computed results are shown in Figure 4-2c for the 524 nm-thick (green) and 3.3 μm-thick (brown) SiN modulator. It is clear that these computed curves qualitatively resemble the

experimental results displayed in Figure 4-2b. However, the computed values for $G_{e\text{-}r}$ are systematically lower than the measured values. This discrepancy is due to the fact that the support beams, which significantly contribute to the radiative conductance (~40%) [99], were not included in the model. The modelled results also indicate that better gating performance than what was measured can be achieved. The computed curve for the thick modulator (brown curve) reveals that the radiative conductance can be suppressed by over an order-of-magnitude by reducing the gap d to ~1 μm. We speculate that similar gating of $G_{e\text{-}r}$ was not observed experimentally due to contributions to the radiative conductance from the beams.

Insight into the physical mechanism responsible for this gating effect can be garnered by analyzing the specific modes that contribute to the radiative heat current between the emitter and receiver. The computed spectral radiative conductance is plotted in Figure 4-3a and reveals that the heat transfer between the silicon nitride membranes occurs at infrared wavelengths primarily between 0.03 eV and 0.2 eV. Recent work performed by us [99] indicates that the radiative heat current between emitter and receiver is determined by their in-plane emission and absorption characteristics, which are significantly enhanced by guided modes supported in the thin membranes. As a result, understanding this gating effect can be achieved through an analysis of a simple slab waveguide with identical thickness as the emitter and receiver membranes [147]. The mode profile of a transverse electric (TE) guided mode (zero-order, symmetric, $\lambda = 16.5$ μm) in a semi-infinite SiN slab with a thickness of 486 nm is plotted in Figure 4-3b. It is clear from this plot that the mode tail extends tens of microns outside of the slab. How this mode is absorbed by the SiN slab was investigated using a commercial finite element modelling (FEM) package. Specifically, this guided mode was injected into the slab from the left side and the ensuing steady-state spatial distribution of the electric field (z-component) was computed and plotted in

Figure 4-3c. As shown in Figure 4-3c, the guided mode propagates along the slab with minimal scattering into free space. The mode is attenuated along the propagation direction due to absorption in the slab, which is governed by the imaginary part of the dielectric function for silicon nitride. The spatial distribution of the electric field was then re-computed after introducing a 524 nm-thick SiN slab to the model with a vertical offset of 3 μm (see Figure 4-3d). Clearly, the guided mode partially couples out of the original membrane and into the second membrane, which effectively reduces the overall power absorbed by the original membrane as some of the power in the mode is absorbed by the second membrane. This analysis suggests that the in-plane absorption cross-section of the receiver must be suppressed when the modulator is brought into close proximity, resulting in a reduction of $G_{\text{e-r}}$.

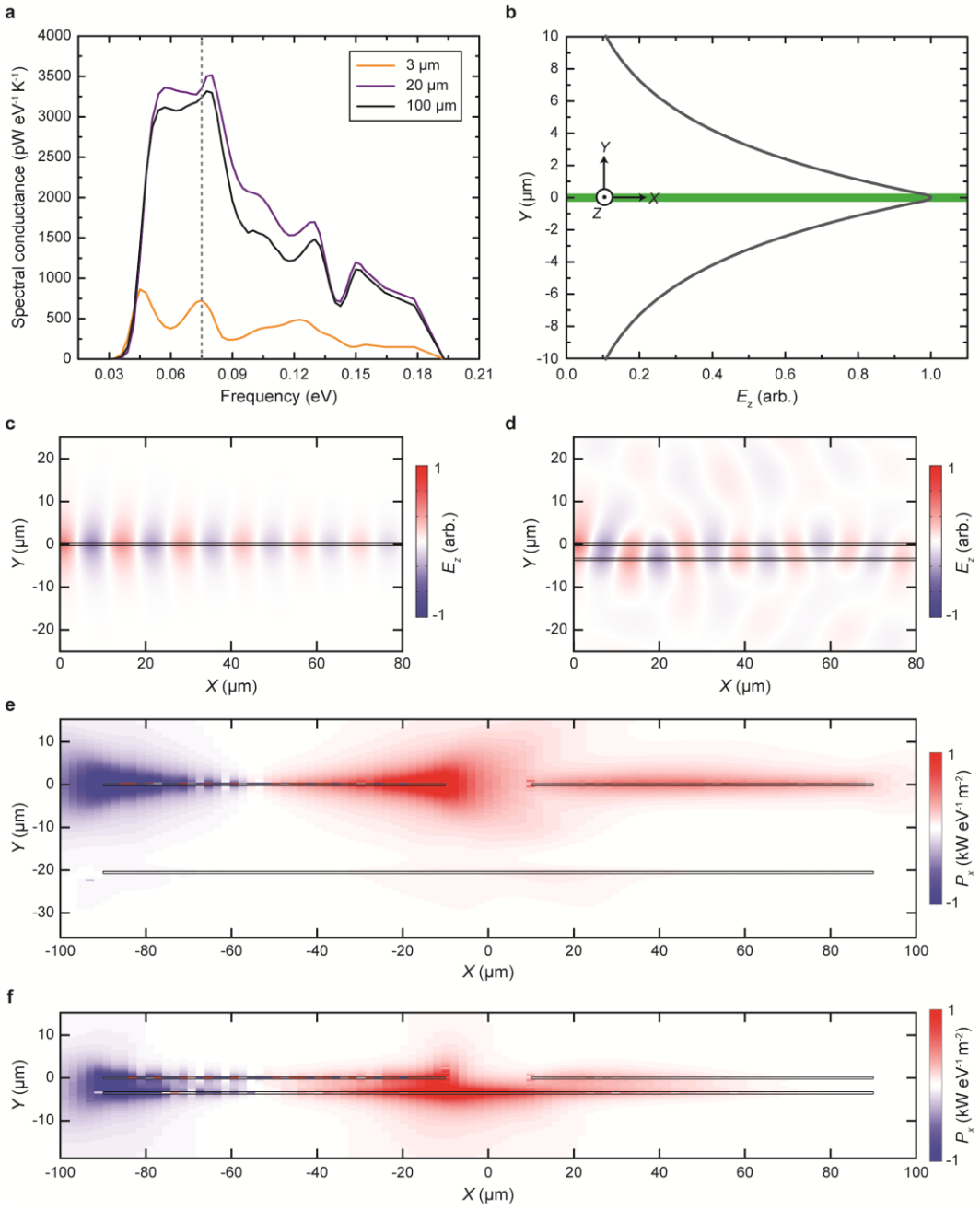

Figure 4-3. Analysis of the physical mechanism responsible for gating of radiative heat currents. (a) Computed spectral heat transfer rate between emitter and receiver for several gap sizes. Here, the modulator is a 524 nm-thick SiN membrane. The vertical dashed line marks a wavelength of 16.5 μm. (b) Mode profile of zero-order TE mode at λ = 16.5 μm in a 486 nm-thick SiN slab. Green region comprises the slab volume. (c) Steady-state spatial distribution of the electric field E_z after the TE mode from b is injected into the 486 nm-thick SiN slab from the left side. (d) Same as in c after a 524 nm-thick SiN slab is introduced with a gap d = 3 μm. (e) Computed Poynting flux P_x at λ = 16.5 μm due to thermally-induced radiation sources in the body of the emitter (top left), which is held at 300 K. The vertical gap between emitter and modulator is d = 20 μm. (f) Same as in e but for d = 3 μm.

We gained further insight by using the electromagnetic solver SCUFF-EM [129] to compute the spatial distribution of the Poynting flux (x-component) for a single wavelength λ = 16.5 μm in the three-body system illustrated in Figure 4-3e. In this model, the gap between the modulator and receiver/emitter pair is d = 20 μm and thermally-induced sources of radiation are established in the body of the emitter (see Methods for additional details about this model). For such a large value of d, the computed Poynting flux is largely confined to the plane of the emitter and receiver. When the gap d is reduced to 3 μm (Figure 4-3f), the Poynting flux effectively leaks from the emitter into the modulator rather than traversing the vacuum gap to the receiver, which is consistent with the reduction in the spectral radiative conductance at this wavelength (see Figure 4-3a, dashed vertical line). Such a picture confirms how the heat current between emitter and receiver can be suppressed due to the presence of the modulator. Additional computations performed by us reveal that the radiation from the emitter couples more strongly into the modulator as the thickness of the modulator is increased, explaining why better gating performance is observed for the 3.3 μm-thick modulator.

Finally, we demonstrate that the gating effect described above can be achieved for a wide range of materials. Specifically, we performed an additional experiment where the SiN modulator membrane was coated with 50 nm of gold (the SiN emitter and receiver membranes were uncoated). The measured radiative conductance $G_{e\text{-}r}$ as a function of gap d for the gold-coated modulator is shown in Figure 4-4a. It is clear that the gating performance is significantly better than that of the uncoated modulators. Indeed, the radiative conductance can be suppressed by over a factor of 5 as the gap is reduced from 18 μm to 2 μm. The measured radiative conductance for gaps greater than 200 μm (see inset of Figure 4-4a) does approach a constant value of ~325 pW/K, which is consistent with the large-gap results for the uncoated modulators

displayed in Figure 4-2b. As explained in the Methods, the magnitude of the peak $G_{e\text{-}r}$ for the gold-coated modulator is higher than that for the uncoated modulators, which can be attributed to the modulator mediating radiative exchange between the bottom surfaces of the emitter and receiver via reflection.

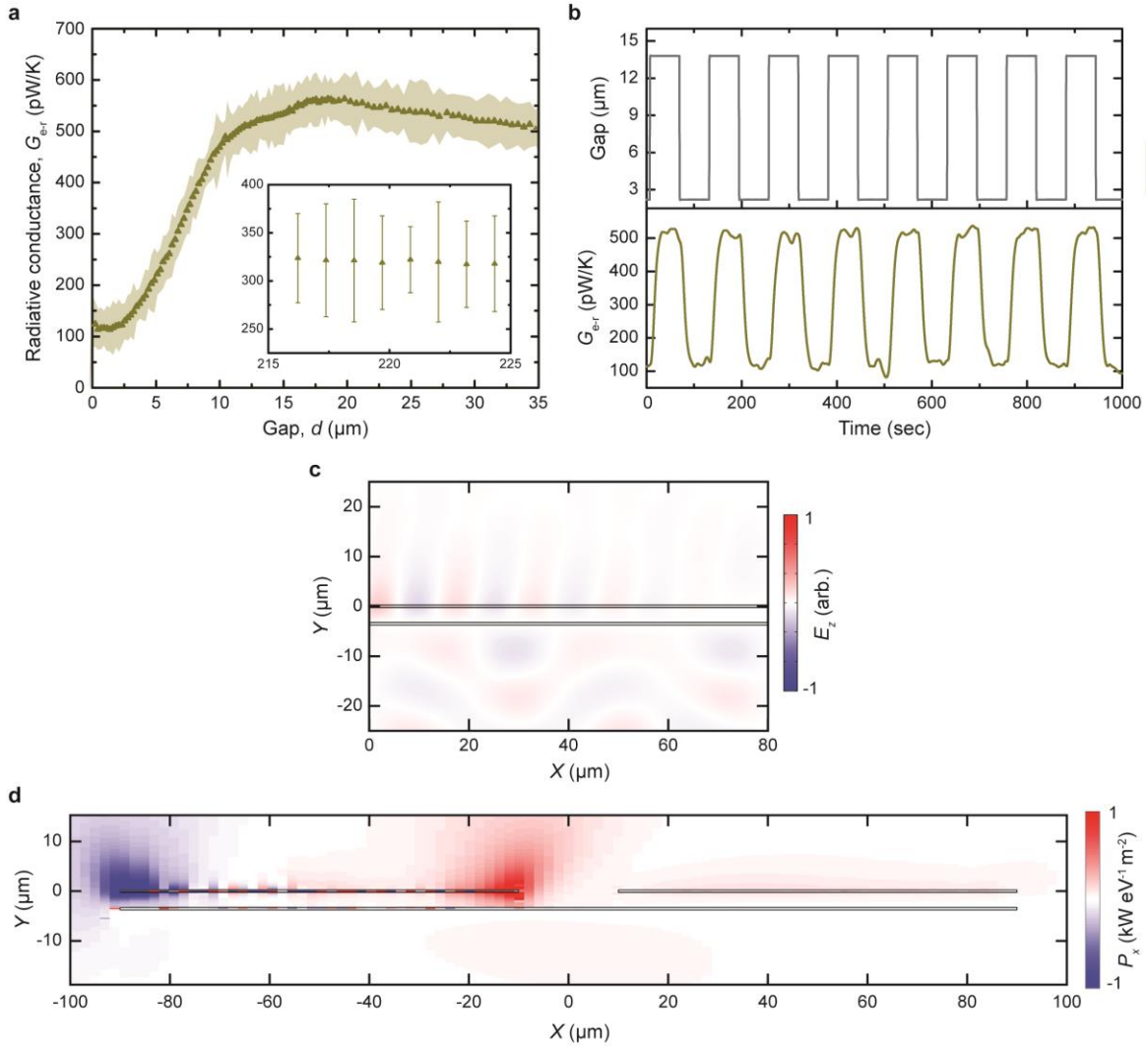

Figure 4-4. Demonstration of gating with gold-coated modulator. (a) Measured radiative conductance $G_{e\text{-}r}$ as a function of gap d for a SiN modulator coated with 50 nm-thick gold. (b) Active modulation of $G_{e\text{-}r}$ with a period of 2 minutes. (c) Steady-state spatial distribution of the electric field E_z after zero-order TE mode at $\lambda = 16.5$ μm is injected into the 486 nm-thick SiN slab from the left side. Here, a 524 nm-thick Au slab is parallel to this SiN slab with a gap separation $d = 3$ μm. Note that the same arbitrary units were used in Figure 4-3c and Figure 4-3d. (d) Computed Poynting flux P_x at $\lambda = 16.5$ μm due to thermally-induced radiation sources in the body of the SiN emitter at 300 K. A gold modulator with a thickness of 524 nm is present, with a gap separation $d = 3$ μm.

Based on the strong dependence of $G_{e\text{-}r}$ on the gap for $d < 20$ μm, we were able to demonstrate active modulation of the radiative conductance $G_{e\text{-}r}$ using the gold-coated modulator. As shown in Figure 4-4b (top panel), we modulated the gap between 2 μm and 13.5 μm by driving the piezo actuator with a square wave voltage with a period of 2 min. We simultaneously recorded the radiative conductance (Figure 4-4b, bottom panel) as the gap was modulated. Consistent with the results from Figure 4-4a, the radiative conductance was actively modulated by a factor of ~5 with the same period. The period of modulation in this experiment was limited by the time constant of the lock-in amplifiers used to collect the thermal signals (3 seconds). In principle, however, the modulation period can be significantly reduced as it is ultimately limited only by the thermal time constant of the suspended membranes, which has been characterized to be ~100 ms. Interestingly, FEM and SCUFF-EM computations indicate that the gating of the heat current using the gold-coated modulator occurs due to a different physical mechanism than for the uncoated modulators. As shown in Figure 4-4c, the TE guided mode injected into the SiN slab does not couple into the gold slab separated by $d = 3$ μm. Rather, the gold cuts off the mode tail so that the TE guided mode is no longer supported by the SiN slab. This results in scattering of this mode into free space instead of absorption in the slab. Similarly, Figure 4-4d reveals that the Poynting flux does not leak from the emitter into the modulator, but rather into free space above the emitter. The net result is that less heat is transferred to the receiver.

4.4 Conclusion

Our experiments and computations demonstrate that the radiative heat current between two SiN nano-membranes in the far-field can be actively suppressed by disturbing the guided modes supported in the membranes. Specifically, we show that a third body interacting with the

evanescent mode tails, which extend outside of the membranes, can be employed to suppress the heat current between the two membranes by several times. In principle, this method can be used to attenuate the radiative heat current without limit, by employing an infinitely thick SiN modulator membrane for instance. The insights from this work could eventually lead to the development of practical switches of radiative heat currents, as well as tunable filters that can effectively modify the heat transfer spectrum for a particular application. Further, since the thermal relaxation times of nanostructures such as the nano-membranes studied in this work are extremely short [148], rapid modulation of the radiative heat currents between such nanostructures is possible, which could have important ramifications for applications such as pyroelectric energy conversion.

4.5 Methods

Fabrication process for the devices: The fabrication process for the modulator device is schematically illustrated in Figure 4-5a. The process starts with a silicon-on-insulator (SOI) wafer with a 10 μm-thick device layer, a 500 nm-thick buried oxide (BOX) layer, and a 500 μm-thick handler wafer (Step 1). A 10 μm-tall mesa feature is then formed by etching through the top device layer to the BOX layer via deep reactive ion etching (Step 2). A LPCVD low-stress silicon nitride (SIN) film with a thickness of 524 nm was then deposited onto the wafer (Step 3). Vias in the SiN layer on the frontside and backside of the wafer were formed via subsequent RIE etch steps (Step 4). Finally, the modulator membrane was released by DRIE etching through the handler from the backside, followed by a 5 minute wet etch with a buffered hydrofluoric acid solution (5:1 BHF) to remove the BOX layer, followed by a 15 minute etch in a 30% KOH solution (Step 5).

The fabrication process for the emitter and receiver devices is shown in Figure 4-5b. The device fabrication begins with a double side polished (DSP) silicon wafer that is 500 μm-thick (Step 1). Then, a LPCVD low-stress silicon nitride (SiN) film with a thickness of 486 nm was deposited onto the wafer (Step 2). Then, 30 nm-thick platinum (Pt) heater-thermometer lines followed by 100 nm-thick gold (Au) contact pads were patterned onto the frontside via subsequent liftoff processes (Step 3). Vias in the SiN layer on the frontside and backside of the wafer were formed via subsequent RIE etch steps (Step 4). The emitter and receiver membranes were released by etching through the silicon handler via KOH (Step 5). The thickness of each device was characterized by spectroscopic reflectometry (resolution ~1 - 2 nm).

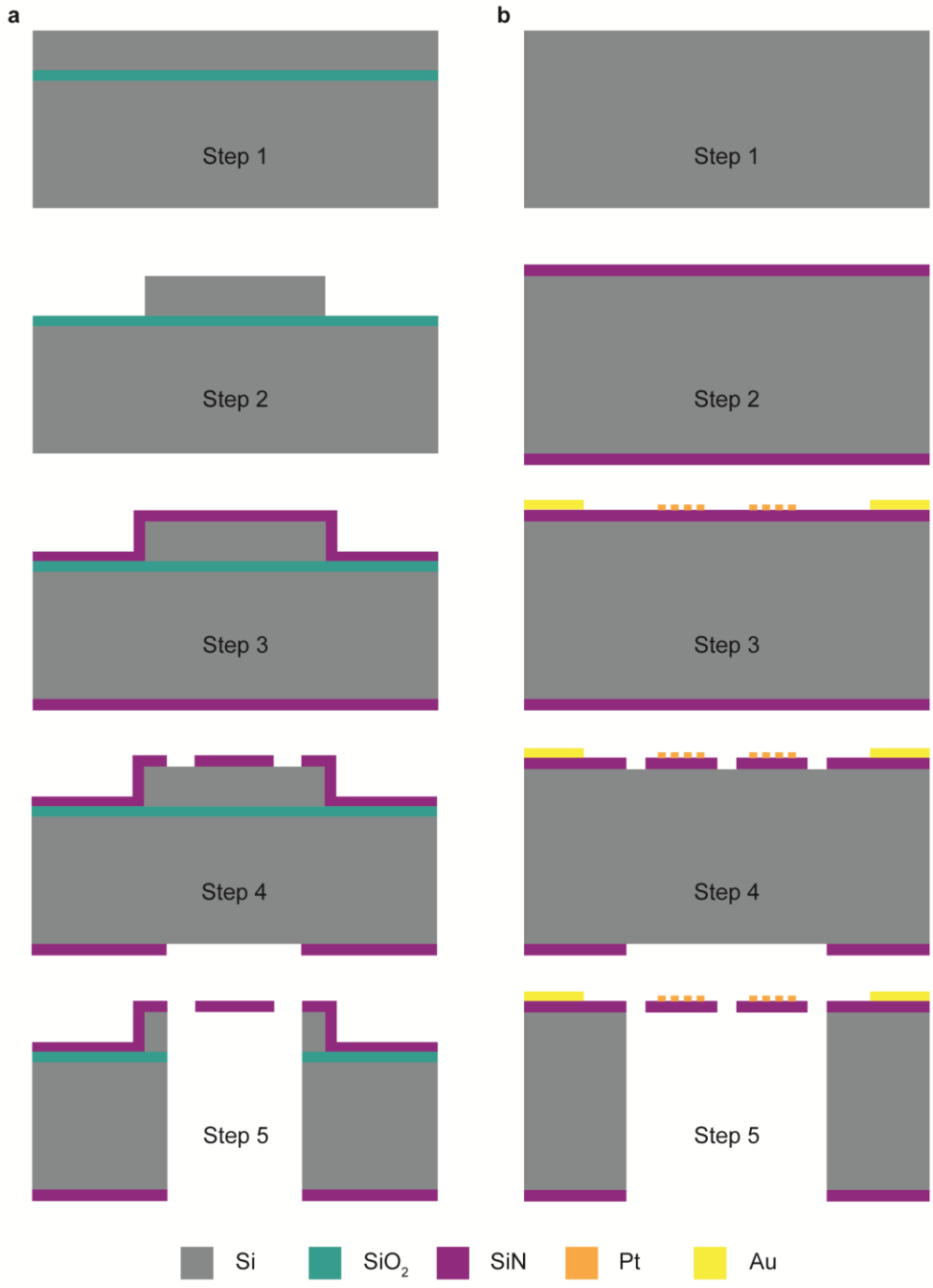

Figure 4-5. Fabrication process for the devices. (a) Fabrication of modulator device, (1) Begin with SOI wafer, (2) Formation of mesa feature, (3) Deposition of SiN layer, (4) Etching of contour in SiN on front and back, (5) Release of devices via combination of DRIE and wet etching, (b) Fabrication of emitter and receiver device, (1) Begin with DSP silicon wafer, (2) Deposition of SiN layer, (3) Patterning of Pt heater/thermometer and Au contact pads, (4) Etching of contour in SiN on front and back, (5) Release of devices via KOH etch.

Characterization of flatness of the suspended membranes: To characterize the flatness of the emitter, receiver, and modulator, we employed laser scanning confocal microscopy (LSCM) on each of the devices. LSCM allowed us to quantify height variations of the top surfaces with a resolution of 60 nm in the vertical direction. As shown in Figure 4-6a, the emitter and receiver are co-planar to an excellent approximation, and each membrane is extremely flat. In fact, the flatness across each membrane deviates by no more than 150 nm. As shown in Figure 4-6b, the 524 nm-thick modulator membrane is also very flat across its top surface. The membrane is slightly warped only near its free edges by ~350 nm due to internal stresses in the membrane.

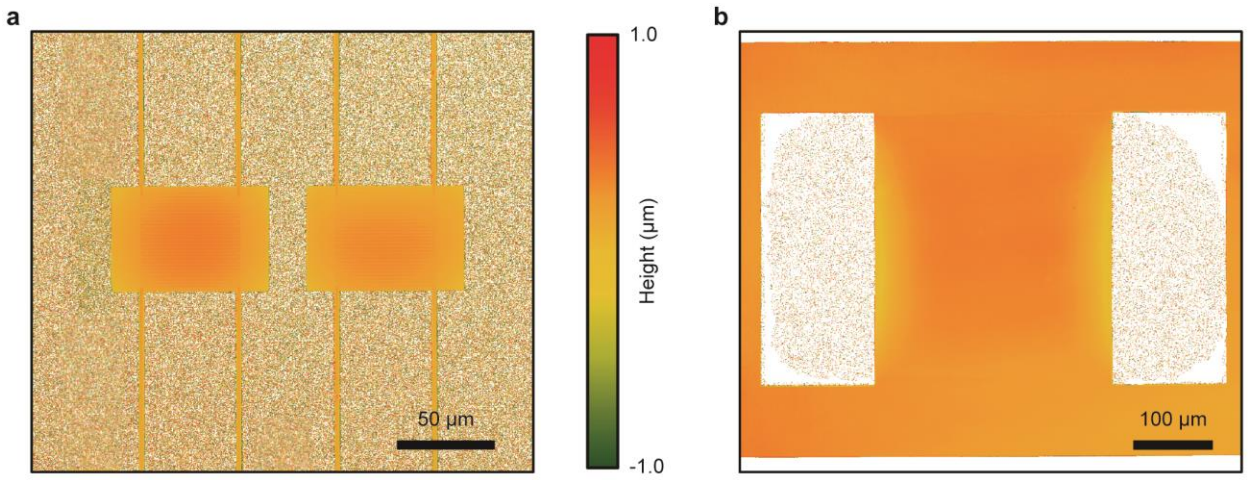

Figure 4-6. Characterization of flatness of suspended membranes. Surface height measured with LSCM for (a) Emitter and receiver devices comprised of 486 nm-thick SiN, and (b) Modulator device comprised of 524 nm-thick SiN.

Details of the measurement procedure: After placing the devices in a high vacuum environment (pressure < 10^{-6} Torr) at ambient temperature T_{amb} ~ 300 K, the emitter was isothermally heated by ~8.5 K at a frequency of 2 Hz by passing a sinusoidal current with a fixed amplitude I_{AC} = 14 µA and frequency of 1 Hz through its integrated platinum heater line. The frequency of the ac current was selected to ensure a full thermal response of the emitter device.

The corresponding voltage oscillation V_e across the heater line at a frequency of 3 Hz was measured using a 4-probe scheme and an SRS 830 lock-in amplifier (lock-in bandwidth ~7.8 mHz). The amplitude of the temperature oscillations of the emitter (ΔT_e) was determined from the equation $\Delta T_e = 2V_e / I_{AC} R\alpha$, where R is the electrical resistance of the heater line and α is the temperature coefficient of resistance (TCR) of the platinum line, which was characterized to be ~1.6×10^{-3} 1/K.

The ensuing radiative heat flow to the receiver device $Q_{e\text{-}r}$ resulted in a modulated temperature rise (ΔT_r) at a frequency of 2 Hz. A DC current I_{DC} = 6 μA was passed through the integrated platinum thermometer line on the receiver and the voltage oscillations V_r across it at a frequency of 2 Hz were measured with an SR830 lock-in amplifier (bandwidth ~ 7.8 mHz). The temperature rise of the receiver was found from $\Delta T_r = 2V_r / I_{DC} R\alpha$.

A thermal resistance network for the two devices is depicted in Figure 4-7. The emitter and receiver are modelled as lumped thermal masses that are each thermally isolated from the surroundings. The degree of thermal isolation is characterized by a thermal conductance G_{Th}, which accounts for conduction through the beams and radiation exchange with the inside of the vacuum chamber. The radiative exchange between the membranes and the modulator is gap-dependent, so the value of G_{Th} for each gap d is estimated from the equation $G_{Th} = P_{Joule}/\Delta T_e$, where P_{Joule} is the power dissipated in the platinum heater. It should be noted that the emitter and receiver are identical devices so that G_{Th} is the same for both. Based on these expressions and the thermal resistance network shown in Figure 4-7, the radiative conductance between the emitter and receiver is found from $G_{e\text{-}r} = (P_{Joule}/\Delta T_e)\times(\Delta T_e/\Delta T_r - 1)^{-1}$.

The measured values of $G_{e\text{-}r}$ were found from the above expression by recording the average value of the thermal signals ΔT_e and ΔT_r at each gap size d using a sampling time of 10

minutes and a sampling rate of 100 samples/second. The error bars displayed in Figure 4-2b and Figure 4-4a were found from the standard deviation of this same raw data. A wait time of 5 minutes was used between each gap size to allow for thermal equilibration of the devices.

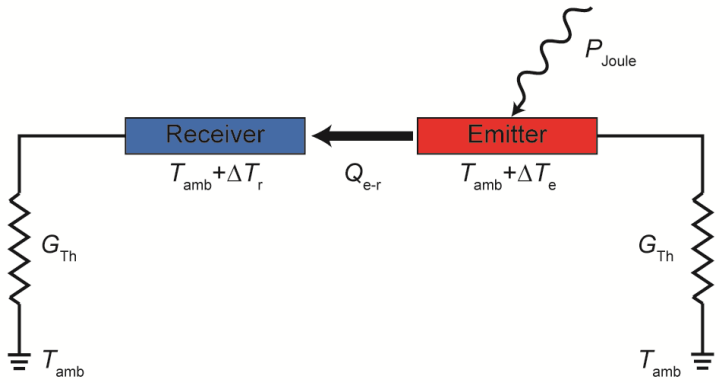

Figure 4-7. Thermal resistance network illustrating relevant heat flow pathways. Emitter and receiver membranes are modelled as lumped thermal masses, thermally isolated from the surroundings by an amount $R_{Th} = 1/G_{Th}$. Joule heating P_{Joule} of the emitter increases its temperature by an amount ΔT_e. Radiative heat flow to the receiver $Q_{e\text{-}r}$ raises its temperature by a corresponding amount ΔT_r.

Description of the SCUFF-EM model: The electromagnetic solver SCUFF-EM [129] was used to model the Poynting flux in the 3-body system depicted in Figure 4-3e, Figure 4-3f, and Figure 4-4d. Because such a calculation is computationally intensive, the full geometry of the three membranes was not modelled. The emitter and receiver membranes in this model were each 80 μm long in the x-direction, 10 μm wide in the z-direction, and 486 nm-thick in the y-direction. The emitter and receiver were separated by a gap of 20 μm. The modulator, also 10 μm wide, had a length of 180 μm, and a thickness of 524 nm.

Thermally-induced sources of radiation were then established in the body of the emitter membrane, which was given a fixed temperature of 300 K. The spatial distribution of the ensuing Poynting flux (x-component) was then computed for a single wavelength $\lambda = 16.5$ μm. We chose to compute the x-component of the Poynting flux because it is the x-component that accounts for

the heat flux from emitter to receiver, since they are co-planar. Note that the thermal radiation originating from the modulator and receiver was not included.

Contribution of reflection from gold-coated modulator to $G_{e\text{-}r}$: It is possible that out-of-plane emissions from the emitter device are reflected from the gold-coated modulator and absorbed by the receiver device, contributing to the measured radiative conductance $G_{e\text{-}r}$. We used the commercial finite element modelling (FEM) software COMSOL to investigate the extent to which these reflections contribute to the measured radiative conductance. A wire-frame rendering of the FEM model, which illustrates how the geometry is discretized, is depicted in Figure 4-8a. In this model, the exact dimensions of the emitter, receiver, and modulator membranes are captured, though Pt lines and support beams for the emitter and receiver are not included. The temperature of the modulator and receiver membranes were fixed at 300 K, while the temperature of the emitter membrane was fixed at 301 K. The surface of the modulator was given a reflectivity of 1, approximating gold as a perfect reflector. The emissivity of the emitter and receiver surfaces were set to 0.2, which is consistent with previous work [99] analyzing the directional emission characteristics of thin-film SiN. Finally, the edges of the emitter and receiver membranes were given insulating boundary conditions so as to eliminate direct heat flow between them. With these boundary conditions, the net heat flux into the receiver $Q_{e\text{-}r}$ due to reflections from the modulator was then computed as a function of gap d separating the modulator and emitter/receiver pair.

The computed radiative conductance $G_{e\text{-}r}$, plotted in Figure 4-8b as a function of gap, is peaked at a gap ~28 μm (see inset) and is rapidly reduced for both large and small gaps. These data indicate that reflection from the gold-coated modulator can contribute up to 90 pW/K to the measured radiative conductance $G_{e\text{-}r}$, which explains why the measured $G_{e\text{-}r}$ for the gold-coated

modulator is larger than that of the uncoated modulators for intermediate gaps (compare Figure 4-4a to Figure 4-2b).

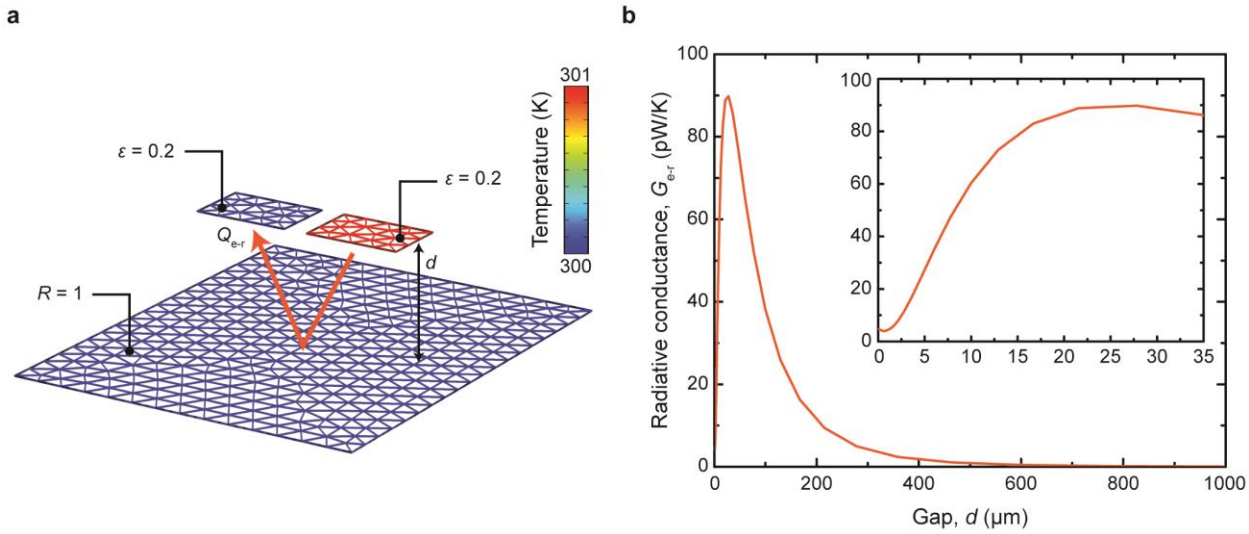

Figure 4-8. Modelling of reflection from gold-coated modulator. (a) Rendering of geometry (including surface discretization) used in FEM model to compute the heat flux to the receiver $Q_{e\text{-}r}$ via reflection from the modulator. Here, the modulator surface was given a reflectivity $R = 1$ and the emitter and receiver surfaces were given an emissivity $\varepsilon = 0.2$. The emitter was given a fixed temperature of 301 K, while all other bodies had a fixed temperature of 300 K. (b) Computed radiative conductance as a function of gap size d. Inset shows same data plotted over a narrow range of gap sizes between 0 and 35 μm.

Chapter 5 Overview and Outlook

5.1 Overview and Ongoing Work

This dissertation comprises a detailed exploration of a set of unanswered questions in the field of radiative thermal transport. In the second chapter (published as [98]) I developed, with help from collaborators in my lab, an experimental platform to measure the radiative heat transfer (RHT) between parallel planar surfaces separated by sub-100 nm gaps. This work demonstrated that orders-of-magnitude enhancements in the RHT above the blackbody limit are observed for polar dielectrics with gap separations as small as 60 nm, verifying theoretical predictions that had been untested for decades. The experimental platform we developed also provided a pathway for exploring a host of other interesting phenomena related to near-field radiative heat transfer (NFRHT). Although these investigations are not presented in this dissertation, I contributed to several follow-up studies which include the experimental demonstration of a near-field based thermophotovoltaic device [70] as well as a radiative thermal diode [138], which leverage the high power density and narrowband spectral characteristics of NFRHT for improved performance. There are many more aspects of NFRHT that I plan to study using this basic platform in the future. For instance, a number of theoretical works studying NFRHT between graphene-coated substrates show that the relative Fermi level of the graphene sheets dramatically influences the net heat transfer rate [45, 149, 150]. These predictions suggest that active suppression or enhancement of NFRHT between graphene-coated substrates is possible via electrostatic gating. Similar effects may be possible with other exotic 2D materials as well. Also, it would be interesting to experimentally study NFRHT between materials with

nanostructured surfaces, which have been predicted to further enhance and spectrally tune NFRHT [38]. Additional improvements to the experimental platform described in Ch. 2 will be required to enable many of these future studies. Currently, there is no way to quantitatively measure the absolute gap size during experiments, and this value must be estimated from the cleanliness of the surfaces and the characterized snap-in distance of the devices. Quantifying the absolute gap size could in principle be achieved interferometrically, and I would like to implement this feature into future manifestations of the platform.

In the third and fourth chapters, I explored interesting aspects of radiative heat transfer between nanostructures in the far-field. In Ch. 3 (published as [99]), I demonstrated that the far-field radiative heat transfer (FFRHT) between co-planar silicon nitride membranes with sub-wavelength thickness exceeds the blackbody limit by two orders-of-magnitude at room temperature. These observations provided the first evidence that Planck's blackbody limit could be dramatically exceeded in the far-field. In Ch. 4 (referenced as [100]), I further explored the physical mechanism responsible for the unique emission and absorption properties of these nano-membranes and demonstrated a novel scheme to gate radiative heat currents in a system with more than two bodies. Specifically, I showed that the FFRHT between two co-planar nano-membranes could be actively suppressed by a factor of five via mutual interactions with a third nano-membrane in close proximity. I hope to undertake several follow-up studies related to these works in the near future. First, I am interested in quantifying the FFRHT between co-planar nano-membranes comprised of gold. We have performed preliminary FED computations suggesting that the net heat transfer rate between such membranes may not monotonically decrease with decreasing membrane thickness, which is quite counterintuitive. Further, I plan to investigate other novel methods to actively suppress or enhance the heat transfer rate between

nanostructures in the far-field. Such schemes could leverage many-body effects similar to that explored in Ch. 4, or even leverage the active tunability of the permittivity of magneto-optic materials (InSb, doped-Si) through the application of an external magnetic field [55, 151].

5.2 Outlook and Future Directions

The interest in radiative thermal transport has grown considerably in recent years, though there remain numerous open questions in this field. To answer these questions, advances in both our theoretical and experimental tools will be required.

At a basic level, the fluctuational electrodynamics (FED) framework requires knowledge of the permittivity of the material system under study. However, information about the permittivity may simply not exist for some exotic or recently developed materials. Even for more common materials, the permittivity may only be known for a narrow range of frequencies, or in a narrow range of temperatures. Further, the permittivity of many materials is known to be size dependent, indicating that the permittivity of a spatially confined material may be dramatically different than that of its bulk counterpart. Indeed, there have been a number of theoretical studies examining the size-dependent permittivity in thin films and low dimensional materials [152-156]. Experimentally characterizing the permittivity of a material relies on Fourier transform infrared spectroscopy (FTIR). Conventional FTIR tools, which extract this information by measuring the material's transmission or reflection of light at a given frequency, are limited to bulk or laterally-large samples and are not guaranteed to accurately capture the permittivity of a nanometric material [157]. Techniques to measure a material's permittivity with nanoscale spatial resolution via scanning probe approaches [145] are still in their infancy, and permittivity information from these types of tools is still more qualitative than quantitative. Developing improved infrared spectroscopy tools that are cheaper, operate over a wider range of frequencies

and temperatures, and have better spatial resolution, will certainly be required to rigorously explore nanoscale radiative thermal transport using computational tools such as FED.

Another research direction that I believe to be interesting is to explore the ultimate limits to the applicability of FED itself. In short, for what system is FED no longer valid for describing thermal radiation and radiative heat transfer? How can breakdowns of FED be experimentally demonstrated? As discussed in Ch. 1, FED was originally formulated using the assumption of a local permittivity. This local approximation may no longer be valid when exploring RHT between metallic surfaces separated by sub-nanometer gaps, for example [14, 158]. Similarly, the FED framework might be inadequate for describing energy transfer in superconducting materials at cryogenic temperatures. Pursuing this research question will require advanced techniques to probe thermal transport in nanometer and Angstrom-sized systems which are smaller than the relevant mean free path of charge carriers comprising the materials. Such calorimetric techniques must have not only unprecedented heat flow resolution below the picowatt level, but also have stringent requirements for the temporal and spatial resolution. Novel techniques to measure nano-Kelvin temperature changes [159-163] are central to developing calorimeters/bolometers with the required heat flow resolution for these demanding studies. Improving the temporal resolution of the calorimeters would also be hugely beneficial for studying transient energy transfer processes that occur at short times scales [148]. Further, the ability to probe heat flows in nanometer/Angstrom sized systems will require thermometry techniques with correspondingly small spatial resolution. Techniques such as scanning thermal microscopy (SThM) have demonstrated single-digit nanometer spatial resolution [164-166] but require physical contact between the sample and the scanning probe tip. Achieving quantitative

nano-thermometry in a non-contact mode would be a huge advance, but such techniques are still in their infancy and currently feature poor temperature resolution [166].

With an eye towards technological applications, I believe that research investigating how to actively modulate and spectrally tune radiative thermal transport will be fruitful. Pyroelectric energy conversion [58, 59] is one example of an energy conversion technology that requires modulated heat flows to generate electrical work. Such a technology could be enabled using techniques to rapidly modulate radiative heat flows in the near-field and far-field. Similarly, the ability to actively tune the thermal emission spectrum of an object could have important ramifications for a number of thermal management technologies [167]. For instance, recent studies have demonstrated that appropriately designed metamaterials which emit exclusively in the atmospheric transparency window (8 μm – 14 μm) can be used for passive refrigeration below ambient temperatures, even in daytime [116]. The ability to actively tune the emission spectrum of such metamaterials could offer improved thermal management of buildings in various weather conditions and seasons. Active control of the spectral and directional characteristics of thermal radiation at nanometer length scales could also have important ramifications for advanced microscopy and spectroscopy tools.

Appendix A: Supplementary Information for Chapter 2

A.1 Nanopositioner and Measurement Environment

The nanopositioner used in our studies has been documented elsewhere [105] and will be briefly described here. It comprises of two major subassemblies: the top and the bottom. The top subassembly houses the receiver device and enables fine control of θ_x, θ_y via motorized linear actuators, as well as coarse positioning along the x and y directions by means of precision micrometer screws. The top subassembly also houses the optical components involved in detecting contact between emitter and receiver devices. The bottom subassembly houses the emitter device and enables lateral positioning along the x and y directions using linear xy stages, and alignment in the θ_x and θ_y angles using a tip-tilt stage. Further, the bottom subassembly enables rotation about (θ_z) as well as both coarse (motorized linear z stage) and fine (piezoelectric actuator) translations in the z direction. The top and bottom subassemblies are connected by four columns such that the emitter and receiver are brought into close proximity for parallelizing when the nanopositioner is fully assembled [105].

We adopted several measures to minimize mechanical disturbances from the laboratory environment, which is essential to maintain stable, nanometre-sized gaps between the emitter and receiver devices. Specifically, we designed a very stiff nanopositioner and performed all experiments on a vibration isolation table. Further, during experiments we employed only an ion pump to preserve a high vacuum in order to eliminate any vibrations resulting from the roughing pump. Additionally, the high vacuum environment largely attenuates the effects of acoustic

noise. We also note that the ambient ground vibration levels in our laboratory conform to the VC-D criterion [168], whereas the acoustic noise conforms to the RC-30 criterion. We estimate, based on the high stiffness of our devices and the low level of ambient vibrations, that the root mean square displacement of the devices due to acoustic perturbations is less than 1 nm. Further, we implemented active temperature control using thermoelectric Peltier devices, as well as passive measures such as radiation and convection shields, to attenuate thermal drift. These measures ultimately attenuated the variation in temperature of the experimental setup to ~10 mK over a period of 10 hours. The effect of this temperature drift on the vacuum gap was found to be negligible as the uncertainty in gap size was estimated to be <1 nm.

A.2 Theoretical Modelling of Near-Field Radiation

Our computation of nanoscale radiative heat transfer was based on the framework of fluctuational electrodynamics (FE) [11]. Specifically, we express the net heat flux Q from a planar multilayer emitter to a planar multilayer receiver in a Landauer-type formula as [111, 112]

$$Q(T_e, T_r, d) = \int_0^\infty \frac{d\omega}{4\pi^2}\left[\Theta(\omega, T_e) - \Theta(\omega, T_r)\right]\int_0^\infty dkk\left[\tau_s(\omega, k, d) + \tau_p(\omega, k, d)\right] \qquad \text{(A-1)}$$

where $\Theta(\omega, T) = \hbar\omega / \left[\exp(\hbar\omega / k_B T) - 1\right]$, T_e (T_r) is the temperature of the emitter (receiver) surface, d is the vacuum gap size, ω is the angular frequency of the radiation, k is the magnitude of the wavevector component parallel to the planes, and τ_s and τ_p are the transmission probabilities for the transverse electric (TE) and transverse magnetic (TM) modes, respectively. The transmissions can in turn be expressed as:

$$\tau_{\alpha=s,p}(\omega,k)=\begin{cases}\dfrac{(1-\left|R_\alpha^e\right|^2)(1-\left|R_\alpha^r\right|^2)}{\left|D_\alpha\right|^2}, k<\omega/c \\ \dfrac{4\,\mathrm{Im}\{R_\alpha^e\}\,\mathrm{Im}\{R_\alpha^r\}e^{-2\mathrm{Im}\{q_{vac}\}d}}{\left|D_\alpha\right|^2}, k>\omega/c\end{cases} \quad \text{(A-2)}$$

where $D_\alpha = 1-R_\alpha^e R_\alpha^r e^{2iq_{vac}d}$ is a Fabry-Perot-like denominator and q_{vac} is the magnitude of the vacuum wavevector component normal to the planes. The R_α terms represent the total reflection coefficients at the two vacuum interfaces and are functions of the interface Fresnel coefficients, $r_s^{ij}=\dfrac{q_i-q_j}{q_i+q_j}$ and $r_p^{ij}=\dfrac{\varepsilon_j q_i-\varepsilon_i q_j}{\varepsilon_j q_i+\varepsilon_i q_j}$. Here, the subscripts *i* and *j* represent adjacent layers, $q_i=\sqrt{\varepsilon_i\omega^2/c^2-k^2}$ is the magnitude of the normal wavevector component in layer *i*, and ε_i is the corresponding material dielectric function. For the case of two semi-infinite bodies separated by a vacuum gap, the indices *i* and *j* vary from 1 to 3 (1 for the emitter, 2 for the gap and 3 for the receiver) and we have $R_\alpha^e=r_\alpha^{21}$ and $R_\alpha^r=r_\alpha^{23}$. We also consider the case in which the emitter and receiver are thin films coated on semi-infinite substrates. For this case, *i* and *j* vary from 1 to 5 (counting up from the bottom layer of the emitter to the top layer of the receiver), $R_\alpha^e=\dfrac{r_\alpha^{32}+r_\alpha^{21}e^{2iq_2t_2}}{1-r_\alpha^{21}r_\alpha^{23}e^{2iq_2t_2}}$ and $R_\alpha^r=\dfrac{r_\alpha^{34}+r_\alpha^{45}e^{2iq_4t_4}}{1-r_\alpha^{45}r_\alpha^{43}e^{2iq_4t_4}}$, where t_i is the thickness of layer *i*.

Since we employ high resolution modulated calorimetry techniques we only needed a small (2 K) temperature difference between the emitter and the receiver in our nanoscale heat transfer experiments, which allows us to analyze the measured thermal conductance in the linear response regime with negligible (<1%) error. We thus compare the measured data with the linearized radiative heat conductance $G(T,d)$ given by:

$$G(T,d)=A_{device}\int_0^\infty\frac{d\omega}{4\pi^2}\frac{\partial\Theta(\omega,T)}{\partial T}\int_0^\infty dkk\left[\tau_s(\omega,k,d)+\tau_p(\omega,k,d)\right] \quad \text{(A-3)}$$

where A_{device} is the 48 μm × 48 μm active area. Here we assume an absolute temperature of T = 300 K. Knowledge of the dielectric functions $\varepsilon_i(\omega)$ for each layer is sufficient to solve for the heat conductance using the above equation. Data for the dielectric function of SiO_2 was extracted from Palik [169] while that for Au was taken from Ordal et al. [170]. The dielectric functions for intrinsic Si was obtained according to the procedure outlined by Wang and Zhang [74]. Further, we modelled doped Si using the dielectric functions from Basu et al. [171].

A.3 Derjaguin Approximation

As confirmed by the large-area AFM scans (Figure 2-1f), the active surface of our receiver features minor deviations from perfect planarity (~30 nm). To accurately compare the measured thermal conductances with computational predictions, we used the well-established Derjaguin approximation [172] and systematically accounted for the deviation from planarity. We directly used the topography obtained from our AFM image of the active surface of the receiver and computed the total gap thermal conductance between small differential surface elements (~50 nm × 50 nm) on the emitter and correspondingly small differential surface elements on the receiver. Specifically, data from the computed parallel plane calculations (described above) were used to obtain the conductance between pairs of elements chosen such that the element on the emitter was immediately beneath the element on the receiver. Finally, the total thermal conductance was obtained by summing the contributions from all such pairs.

Appendix B: Supplementary Information for Chapter 3

B.1 Theory of Far-Field Radiative Heat Transfer between Finite Bodies

The theory of far-field radiative heat transfer (FF-RHT) is presented in numerous textbooks, for example see Ref. [8]. Here, for completeness, we summarize key results from FF-RHT theory. Specifically, we describe how radiative heat transfer between blackbodies is computed within FF-RHT theory. The key properties of blackbodies are: (1) A blackbody absorbs all incident radiation regardless of wavelength and direction, and (2) a blackbody is a diffuse emitter, i.e. the emitted radiation intensity is independent of direction. Given these simplifying properties, the net heat flow (Q_{12}) between two blackbodies (labeled 1 and 2, see Figure B-1) is given by:

$$Q_{12} = \sigma A_1 F_{12}(T_1^4 - T_2^4) = \sigma A_2 F_{21}(T_1^4 - T_2^4) \tag{B-1}$$

where σ is the Stefan-Boltzmann constant, A is the surface area, T is the temperature, and F_{12} and F_{21} are geometric functions known as the view factor. The view factors are given by the following integrals:

$$F_{12} = \frac{1}{A_1}\iint_{A_1,A_2}\frac{\cos(\theta_1)\cos(\theta_2)}{\pi r_{12}^2}dA_1\,dA_2; \quad F_{21} = \frac{1}{A_2}\iint_{A_1,A_2}\frac{\cos(\theta_2)\cos(\theta_1)}{\pi r_{21}^2}dA_2\,dA_1 \tag{B-2}$$

where the angles (θ_1, θ_2), the differential elements (dA_1, dA_2) and the spatial separation between the differential elements (r_{12}) are indicated in Figure B-1. From these integrals it is also

clear that the reciprocity relationship $A_1F_{12} = A_2F_{21}$ is satisfied. Finally, at low biases (i.e. when $T_1 \sim T_2 = T$) the thermal conductance (G) between the blackbodies is given by:

$$G = 4\sigma A_1F_{12}T^3 = 4\sigma A_2F_{21}T^3 \quad \text{(B-3)}$$

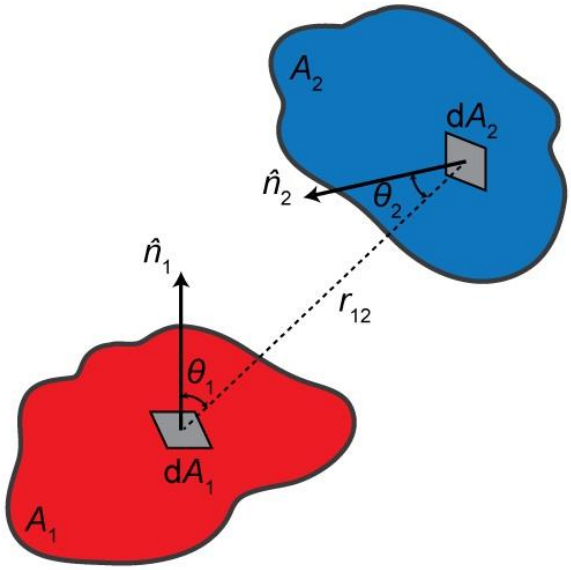

Figure B-1. Schematic describing two finite sized objects at different temperatures exchanging thermal radiation. Infinitesimal surface patches are shown along with other relevant parameters.

B.2 Ratio of the Radiative Conductance Estimated from FED to That Estimated from the Blackbody Limit for Metallic and Dielectric Nano- and Micro-Spheres

One may incorrectly assume that the blackbody limit can be readily overcome for sub-wavelength metallic and dielectric spheres as it is well known that such spheres possess resonances in their absorption cross-section. In fact, a careful analysis of the problem reveals the challenges in overcoming the blackbody limit. To illustrate this fact, we computed the radiative heat transfer between spheres separated by a gap of 20 microns (see Figure B-2a). First, we computed the spectral radiative heat conductance for Au spheres of various diameters using the boundary element method based on fluctuational electrodynamics (FED, [127, 129]).

Next, we treated the spheres as blackbodies and computed the spectral radiative heat conductance taking into account the view factor. Between two spheres of equal diameters *d*, with a vacuum gap size of *L*, the view factor is given by [8]:

$$F_{12} = \frac{1}{2}\left[1 - \sqrt{1 - \left[\frac{d}{2(d+L)}\right]^2}\right] \tag{B-4}$$

Thus, at temperature *T*, the spectral radiative heat conductance ($G(\omega)$) between the spheres, assuming the spheres are blackbodies, is given by:

$$G(\omega) = \pi d^2 F_{12} \frac{1}{\lambda^2} \frac{d}{dT}\left[\frac{\hbar\omega}{e^{\frac{\hbar\omega}{k_B T}} - 1}\right] \tag{B-5}$$

where λ is the wavelength, $\hbar$ is the reduced Planck's constant and ω is the angular frequency. Finally, the total radiative thermal conductance (*G*) is given by:

$$G = \int_0^\infty \pi d^2 F_{12} \frac{1}{\lambda^2} \frac{d}{dT}\left[\frac{\hbar\omega}{e^{\frac{\hbar\omega}{k_B T}} - 1}\right] d\omega = \pi d^2 F_{12} \times (4\sigma T^3) \tag{B-6}$$

From these data we computed the ratio of the FED spectral heat conductance to that obtained from the blackbody limit. The computed ratios, which we call the enhancement ratios, are depicted in Figure B-2c. It can be seen that enhancement ratios are rather small. Further, analysis of the ratio of the total thermal conductance computed using FED to that computed using the blackbody limit (Figure B-2b) reveals that there is no enhancement compared to the blackbody limit. Similar analysis performed on dielectric SiN spheres of various diameters reveals that enhancement ratios in the range of 1 - 3 can be potentially achieved for the spectral heat flux (Figure B-2d), but the total thermal conductance barely exceeds the blackbody limit only for SiN spheres with ~10 μm diameters. We note that as the spectral radiative heat transfer between blackbodies is broad-band, enhancement at certain wavelengths does not necessarily

lead to an exceedance of the total thermal conductance over the blackbody limit. In strong agreement with these theoretical predictions, there is no experimental evidence to date that the heat transfer rate between any two objects in the far-field (macroscopic or microscopic) can exceed the blackbody limit as given by Eqns. (B-1 & B-2).

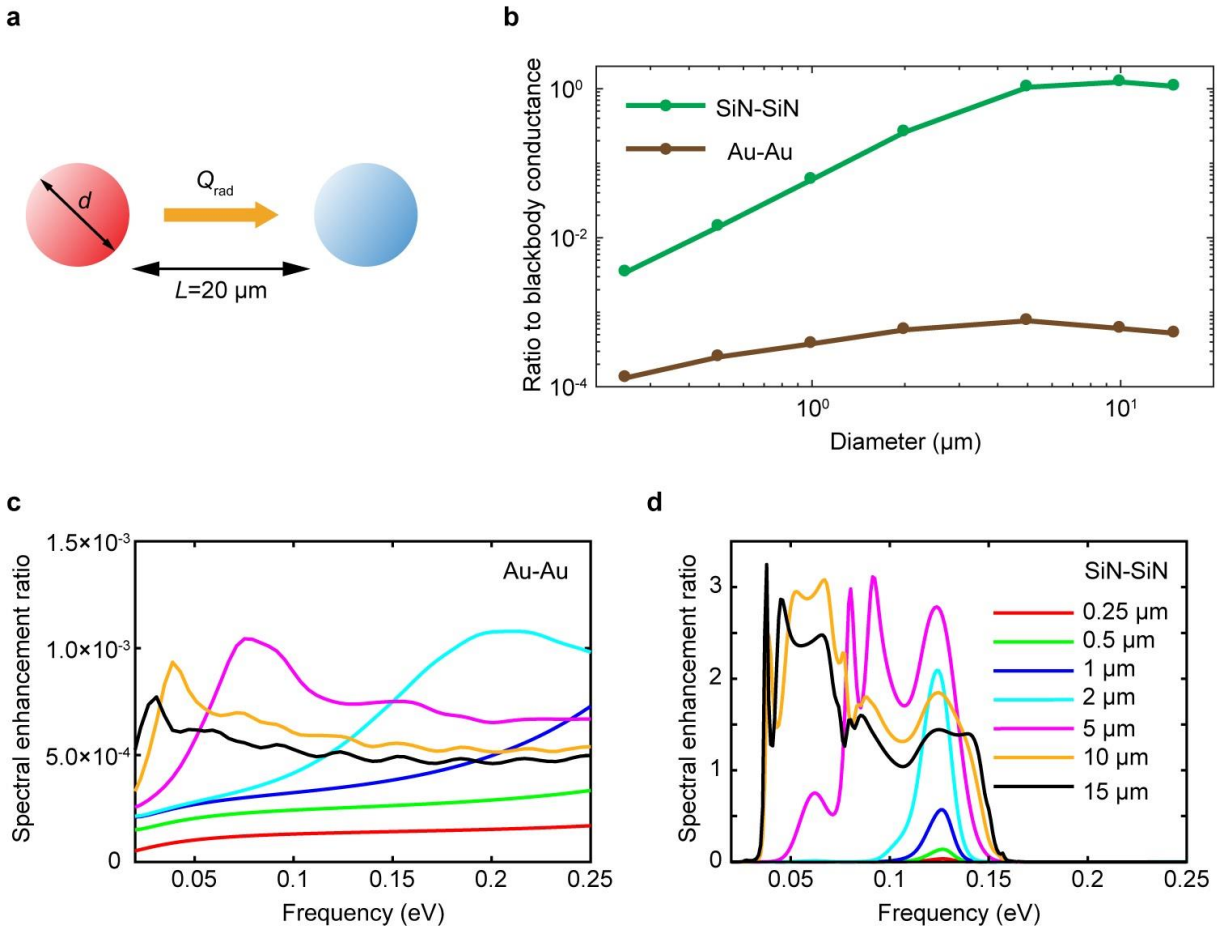

Figure B-2. FED computation of the radiative conductance at 300 K between sub-wavelength spherical particles separated by a 20 μm vacuum gap. (a) Two spheres with equal diameters *d* separated by a vacuum gap of *L*=20 μm. (b) Spectrally-integrated radiative conductance normalized to the blackbody limit. Ratio of the computed spectral radiative conductance to the spectral blackbody conductance for (c) Au spheres and (d) SiN spheres of various diameters. The legend in d also applies to the curves in c.

B.3 Finite Element Simulations Performed to Compute $G_{rad,\,eff}$ and Compare Measured Radiative Heat Transfer with Predictions of FF-RHT Theory

We employed COMSOL Multiphysics (AltaSim Technologies) to simulate the effective radiative conductance ($G_{rad,\,eff}$) between adjacent membranes assuming that both the emitter and receiver are blackbodies. This assumption was made to estimate the upper bound to $G_{rad,\,eff}$ based on Planck's FF-RHT theory. In this model, the exact geometry of the devices, including the platinum resistive thermometer and the beams, was accounted for (see Figure B-3a and c for representative images of the COMSOL model). In our simulations the ends of the beams, which are affixed to a silicon substrate, were given a 300 K fixed-temperature boundary condition. Volumetric Joule heating, that is proportional to the local resistivity, was applied to the serpentine heater on the emitter membrane as well as the current-carrying leads on two of the support beams. The surfaces of the SiN membranes were assigned an emissivity of 1 so that they radiate thermal energy like blackbodies. Further, the thermal conductivity of the SiN was assumed to be ~3 W/m·K [132], which is consistent with our measurements of the beam conductance. In our simulations we meshed the suspended membranes and the beams into >10,000 domain elements (Figure B-3b) and computed the temperature rise of the suspended regions of the emitter and receiver (we note that we carefully checked for convergence of our calculations). Finally, effective radiative conductance ($G_{rad,\,eff}$) in the blackbody limit (emissivity = 1) was computed following an approach mirroring that employed in experimental measurements, i.e. it was estimated from $G_{rad,\,eff} = G_{beams}\Delta T_{rec} / (\Delta T_{emit} - \Delta T_{rec})$. For self-consistency, the value of G_{beams} employed in these calculations was obtained by computing the temperature rise of the emitter membrane for a given heat input. FEM simulations were

performed for each device-geometry employed in our experiments. The obtained results are shown in Figure 3-2b, c.

Finally, FEM simulations were also used to characterize the temperature uniformity of the suspended membranes. Specifically, we determined that any temperature deviations within the suspended membranes were less than 1% from the average temperature. Similarly, the temperature profile along the support beams was found to be essentially linear, even for the support beams with the current-carrying leads.

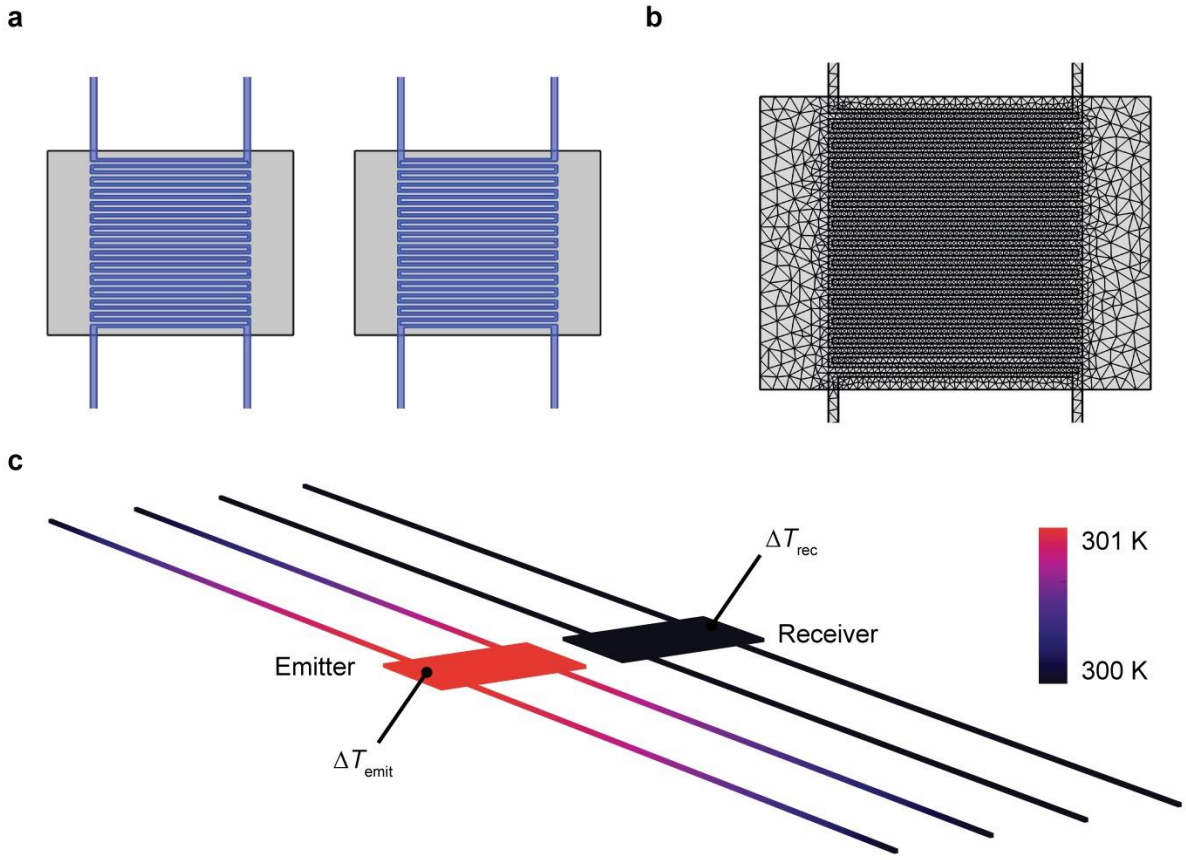

Figure B-3. Details of FEM simulations performed to estimate $G_{rad,\,eff}$. (a) Top view of the device geometry as modeled in COMSOL. Silicon nitride membranes are shown in gray while the Pt serpentine pattern is highlighted in blue. (b) Zoomed-in view of the discretization mesh on one membrane. (c) Computed surface temperatures of the emitter membrane and receiver membrane. In the simulations the ends of the beams were fixed at 300 K and the emitter membrane was Joule heated by 1 K.

B.4 Description of the Computation Scheme for Evaluating $G_{\text{rad, eff}}$ using the BEM

BEM calculations of the RHT between the suspended devices employed in this work are challenging due to the following reasons: First, the support beams are long and make non-negligible contributions to the RHT. Therefore, the beams have to be included in successful modeling efforts, which makes the calculations computationally intensive. Secondly, the emitter device features a large temperature gradient along the support beams (see Figure B-3c), which prevents treating the suspended emitter as an isothermal body and requires modeling the emitter as many bodies at different temperatures. Thirdly, modeling the temperature rise of the receiver membrane (ΔT_{rec}) requires careful evaluation of the spatial distribution of the radiation absorbed by the beams and the resulting impact on the temperature of the suspended membrane.

To tackle the above-mentioned challenges, we use a many-body approach to directly calculate the RHT from different parts of the emitter device to different parts of receiver device. Specifically, we treat the emitter side as a composition of multiple bodies: the suspended membrane is treated as a single body (with negligible temperature gradients) while the long beams are evenly divided into four segments each, as shown in Figure B-4b. For the sake of visualization, we show a gap between the segments of the support beam in Figure B-4b, but in actual computations the segments are continuous. In performing our BEM calculations, each segment is assumed to be isothermal, and the temperature of each segment is represented by the temperature at its center location. Similar segmentation of the support beams was also performed for the receiver. We note that our numerical analysis shows that segmenting each support beam into four parts is sufficient for achieving results with ~2.5% accuracy. Accordingly, in this study, we have 17 bodies to represent the emitter, and another 17 bodies for the receiver (see discussion below).

Following the segmentation of the geometry, we calculated the radiative conductance from each of the bodies on the emitter to each of the bodies of the receiver. In total, we computed 289 different radiative conductances. We note that this approach makes no assumptions regarding the additivity of radiative heat transfer, and interference effects between bodies are completely captured. We also point out that in our calculations the temperature of each segment of the emitter side is obtained from the fact that the temperature profile in the beams is linear to a very good approximation. For the receiver side, in performing the RHT analysis, we first assume that the temperature of all the segments is the same as the ambient since the temperature rise is very small. Finally, to compute the temperature rise of the suspended region of the receiver device (i.e. ΔT_{rec}) due to the radiative currents, which is necessary to evaluate $G_{\text{rad, eff}}$ (recall $G_{\text{rad, eff}} = G_{\text{beams}} \Delta T_{\text{rec}} / (\Delta T_{\text{emit}} - \Delta T_{\text{rec}})$), we take the radiative heat currents into the individual beam segments as inputs to the 1-dimensional (1D) heat conduction equation ($k(x)\frac{\partial^2 T}{\partial x^2} = -q(x)$) [173], where k is the thermal conductivity and $q(x)$ is the radiative heat input per-unit length at location x along the beam and solved for ΔT_{rec} numerically via a finite difference scheme. Specifically, each beam segment was assigned a node number n, with radiative heat input per unit length and temperature for the node denoted as q_n and T_n, respectively. Then, an expression is developed that relates the temperature of the node to the temperatures of the surrounding nodes via $q_n \Delta x = \left(kA_c / \Delta x\right)\left[2T_n - T_{n-1} - T_{n+1}\right]$, where Δx is the length of each beam segment, A_c is the cross sectional area of the beam, and thermal conductivity k is assumed to be constant. A similar equation is developed for each node, and then all equations are solved simultaneously to determine the temperature of each node and the

temperature of the suspended membrane. We denote this method as the FED + heat conduction equation approach.

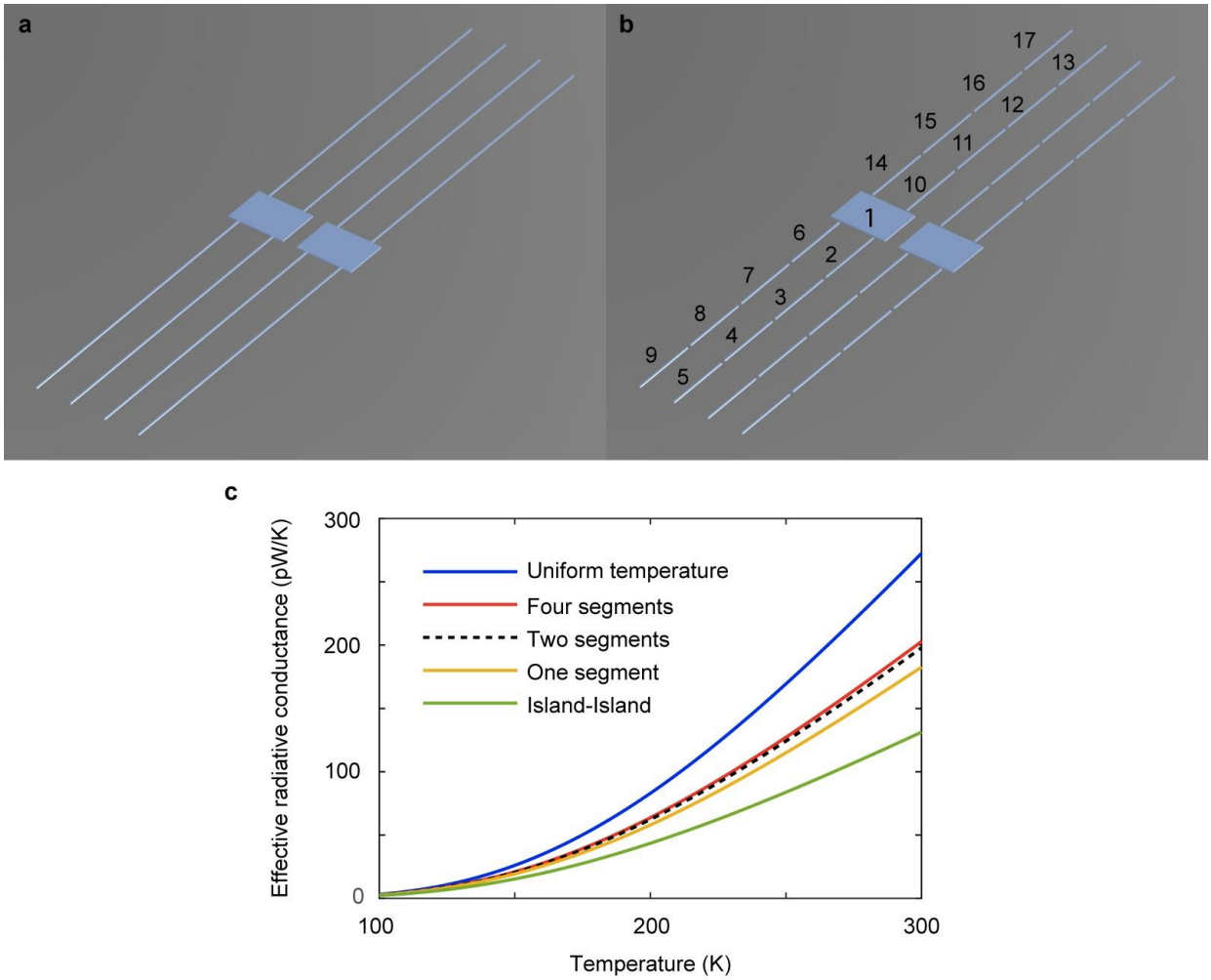

Figure B-4. Geometry and approach for discretization for BEM simulation. (a) A representative geometry employed in BEM simulations. (b) An illustration of the segmenting scheme used in the calculations where each beam was divided into four segments. A gap is shown between neighboring segments for ease of visualization. (c) The computed effective radiative conductance for a scenario featuring 270 nm thick membranes, using different segmentation schemes for the beams. The green line denotes the radiative conductance obtained by neglecting the beams. The blue line denotes the radiative conductance obtained assuming a uniform temperature in the beams of the emitter and that all the RHT to the receiver is effectively localized to the suspended region of the receiver. The yellow, black dashed, and red lines denote the effective radiative conductance obtained by dividing each beam into one, two and four segments, respectively.

We confirmed the accuracy of the FED + heat conduction equation approach, by comparing it with an alternate approach where we combine FED results for modeling RHT with COMSOL simulations for solving for heat conduction. Specifically, we introduced the radiative heat flux into each segment of the receiver side as a heat source in a COMSOL based finite element model (which does not make the 1D approximation inherent in the approach described above) and used COMSOL to directly calculate the resulting temperature rise on the Pt sensor. The results from the FED + 1D heat conduction equation approach and those from the combined FED + COMSOL simulation were practically the same.

Finally, to illustrate the necessity of considering the long beams and for using the many-body approach, we show in Figure B-4c results from calculations where we invoked coarser segmentation approaches or ignored the contributions of the beams. When the beams are ignored, i.e. when only the RHT between the two planar membranes is considered (green line), $G_{\text{rad, eff}}$ is underestimated by ~40 %. However, if one approximates the beams of the emitter to be at one uniform temperature (same as the emitter membrane), then $G_{\text{rad, eff}}$ is overestimated by ~40% (blue line). The yellow, black dashed, and red lines denote the radiative conductance computed by dividing each long beam into 1 part, 2 parts, and 4 parts, respectively. We observe that dividing each long beam into 4 parts is sufficient for obtaining convergence within 2.5%.

B.5 Definitions of HFER and ACER

We define the Heat Flux Enhancement Ratio as HFER = $S_{\text{FED}}/S_{\text{BB}}$. Here S_{FED} is the heat flux (time averaged Poynting vector) corresponding to thermal emissions from a membrane, which was computed using fluctuational electrodynamics at a desired location along the dashed circle shown in Figure B-5. The denominator S_{BB} (blackbody heat flux) is the heat flux at

corresponding points on the dashed circle (see Figure B-5) obtained by treating the membrane as a blackbody and calculated by using standard FF-RHT theory.

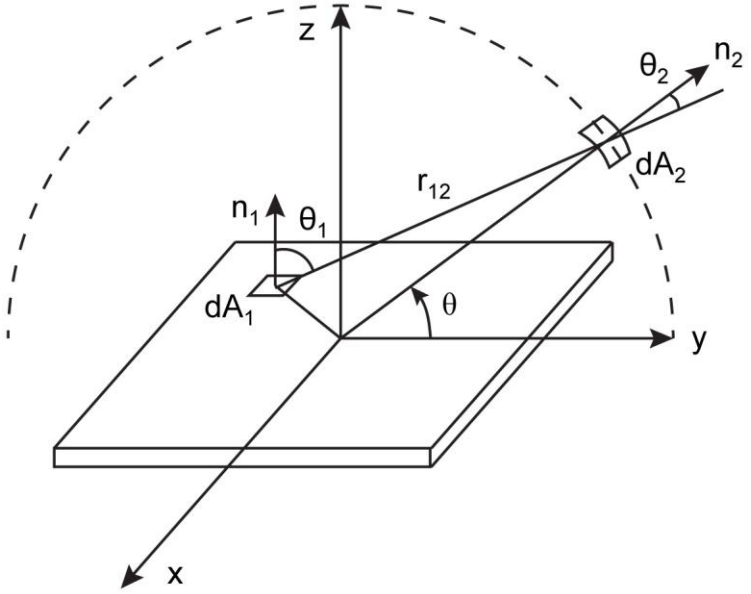

Figure B-5. Schematic describing the angles and area elements employed in evaluating the heat flux (S_{BB}).

For completeness, we note that S_{BB} is evaluated from $S_{BB} = \frac{\sigma T^4}{\pi} \iint \frac{dA_1 \cos\theta_1 \cos\theta_2}{r_{12}^2}$,

where T is the absolute temperature of the surface and the angles θ_1, θ_2, and the distance r_{12} are as shown in Figure B-5. The surface integral is evaluated over all area elements of the membrane that have a direct line of sight to the point of interest.

The Absorption Cross-Section Enhancement Ratio is defined as ACER = σ_{FED}/σ_{BB}. Here, σ_{FED} is the absorption cross-section as computed from fluctuational electrodynamics, whereas σ_{BB} is the projected area of the membrane when viewed from different angles (see Figure B-6). The σ_{FED} is averaged from the absorption cross-sections at two orthogonal polarizations. In the calculation for the absorption cross-section at one polarization, a

monochromatic plane wave of that polarization with unity intensity is incident on the structure, and we compute the power absorbed by the structure, which gives the absorption cross-section of the structure at that polarization. The definition of S_{BB} follows from the fact that in FF-RHT theory all rays intersecting a blackbody are absorbed, while those that do not intersect the surface are not absorbed.

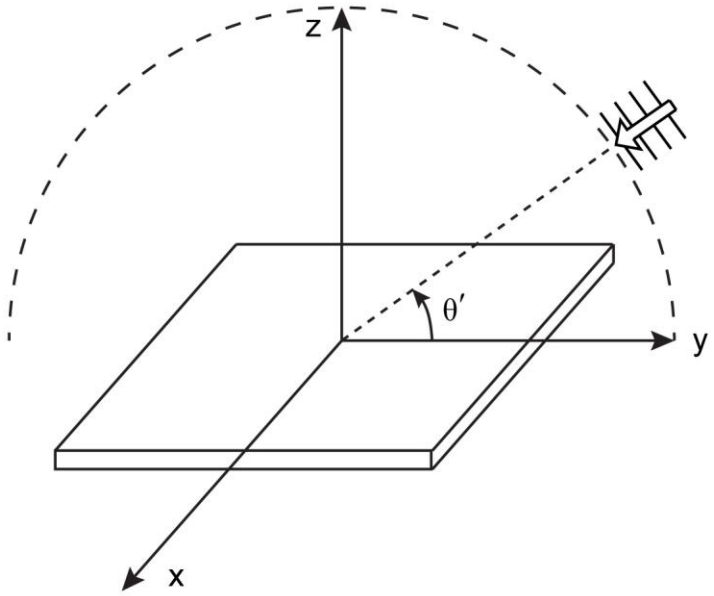

Figure B-6. The projected area of the membrane when viewed along the ray making an angle θ' with respect to the y-axis gives the absorption cross-section S_{BB} corresponding to that angle.

Finally, we note that the HFER values shown in Figure 3-5a, c, were computed at relatively small distances from the membrane center (radius of ~60 μm) and are in general not equal to the computed ACER values. However, from Kirchhoff's law one should expect that if HFER values were computed at distances much larger than the dimensions of the objects then the HFER and ACER values must agree well with each other. The data shown in Figure B-7 below indeed confirms this expectation.

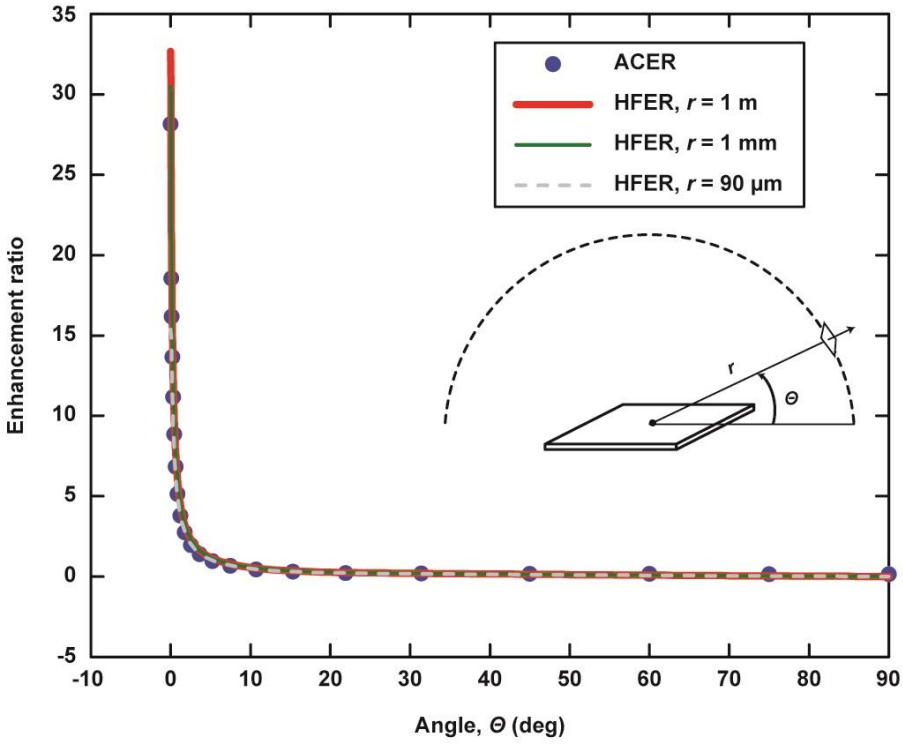

Figure B-7. Comparison of computed ACER with HFER values at relatively large distances. HFER values computed at a radius of 90 µm, 1 mm and 1 meter for various polar angles are shown along with ACER values computed for the same polar angles. The ACER and HFER values are found to be identical to each other.

B.6 Computed HFER and ACER for 486 nm and 6712 nm Thick SiN Membranes

In Figure B-8, we present the results for HFER (heat flux enhancement ratio) and ACER absorption cross-section enhancement ratio) for the cases where the thicknesses of the SiN membranes were 486 and 6712 nm. Consistent with Figure 3-5, for thin membranes (486 nm), HFER and ACER exceed unity in the in-plane direction. As the thickness increases, HFER and ACER become increasingly independent of the polar angle (q,q').

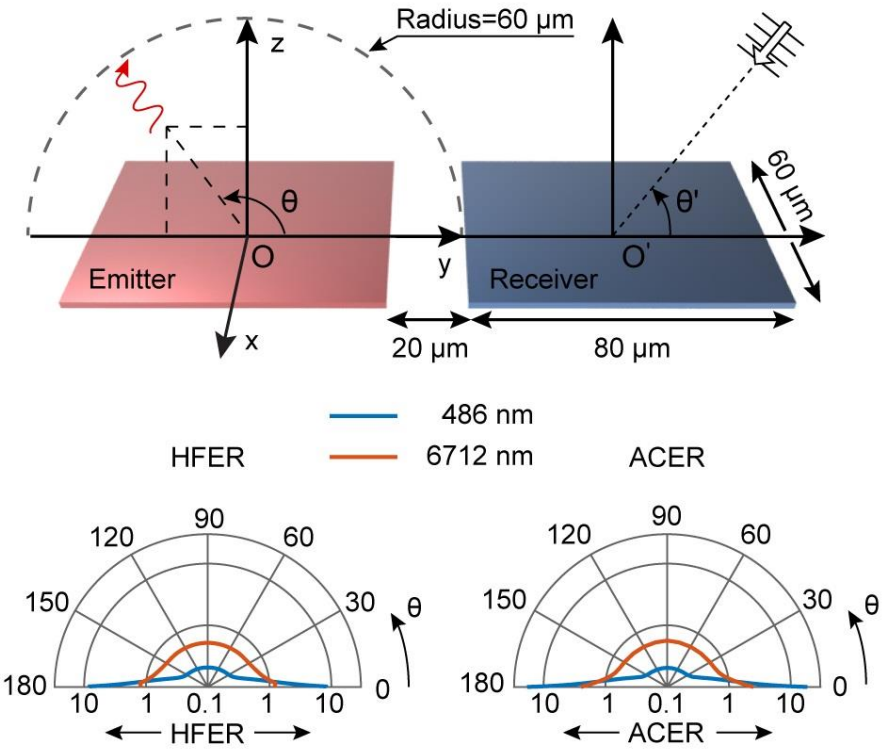

Figure B-8. The heat flux enhancement ratio (HFER) and absorption cross-section enhancement ratio (ACER) for silicon nitride membranes. HFER and ACER are shown for the cases where the membrane thickness is 486 nm and 6712 nm. The transverse dimensions of the membranes are 80 μm by 60 μm. The gap between the two membranes is 20 μm.

B.7 Radiative Heat Transfer Between Thin Gold Membranes

A question that arises naturally is whether exceedances in comparison to the blackbody limit are restricted to dielectrics such as silicon nitride that are the focus of our work presented earlier. To answer this question, we computationally studied RHT between gold (Au) membranes in the far-field. For this analysis the dielectric function for gold was obtained from Ref. [174].

The geometry of the two coplanar gold membranes studied in this work is illustrated in Figure B-9a. The gold membranes have a width of 20 μm and a depth of 80 μm, with a 20 μm vacuum gap between the two membranes. We use the BEM to analyze the RHT, for a series of thicknesses, including 100 nm, 270 nm, 486 nm, 1998 nm, 6712 nm and 11405 nm. To achieve

convergence for heat transfer between gold membranes, it was found that a finer mesh was required than that used in SiN structures. We note that to keep the computations tractable, these gold membranes were chosen to have smaller widths than the SiN membranes analyzed in this study.

The computed spectral radiative conductance at a temperature of 300 K is shown in Figure B-9b for different thicknesses. When the thickness increases from 1998 nm to 11405 nm, the spectral conductance rises slightly. In contrast to naive expectations, when the thickness is decreased below 2 μm, the spectral conductance in fact increases. This is most clearly demonstrated for 100 nm thick membranes, which feature the highest conductance among the six cases examined.

We also studied the dependence of radiative conductance on temperature (Figure B-9c). Indeed, thin gold membranes continue to exhibit a rather large radiative conductance at all temperature ranges. In Figure B-9d, we show the ratio of radiative conductances predicted by FED relative to that predicted by FF-RHT theory when the Au membranes are treated as blackbodies. We observe that for thick gold membranes the ratios are small. In contrast, for gold membranes with deep sub-wavelength thickness, the RHT from FED is seen to surpass the blackbody limit by orders of magnitude! We do not experimentally probe these results due to challenges in creating the necessary devices. Based on the above analysis we suggest that the blackbody limit may be violated by orders of magnitude for a range of sub-wavelength metallic and dielectric planar structures. Thus, the findings presented in the study are expected to apply to a broad array of materials. These interesting and somewhat counter-intuitive predictions (especially for ~100 nm thin films) need to be experimentally verified and will be the focus of our future work.

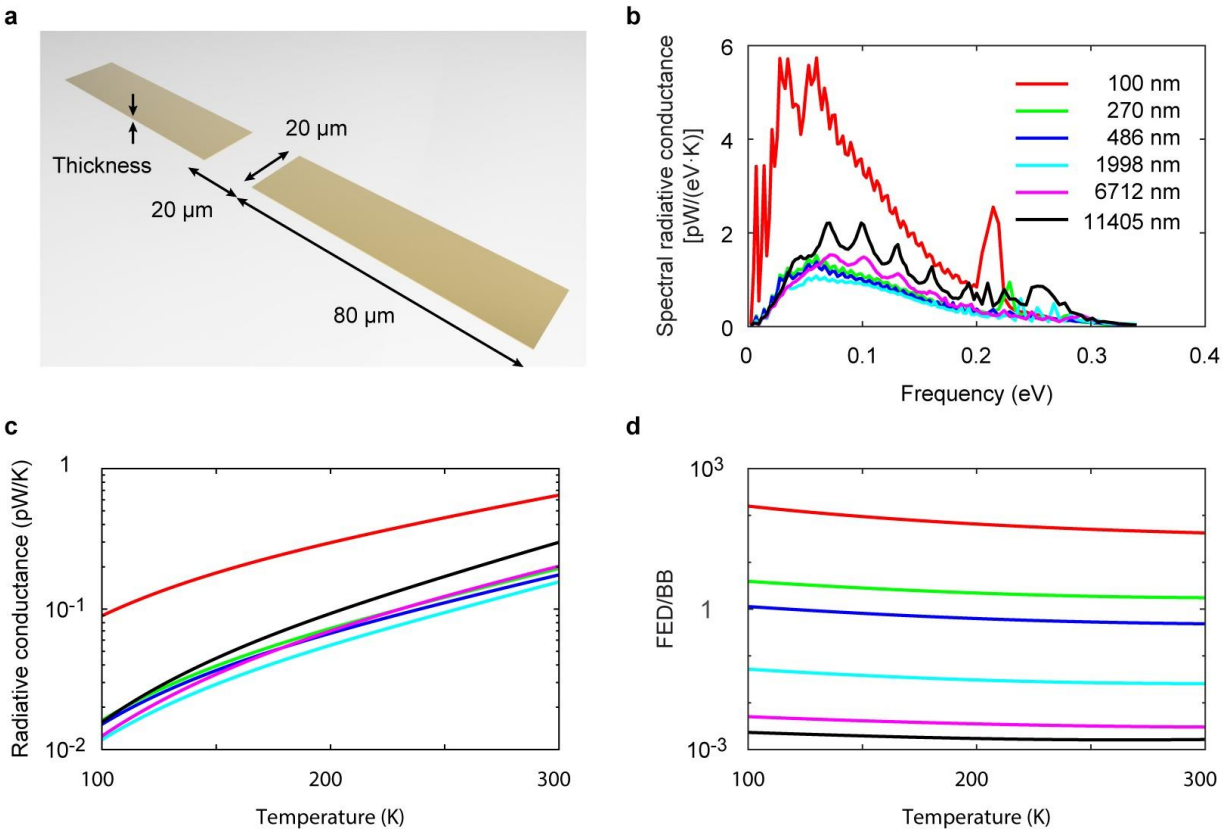

Figure B-9. (a) Geometry of the Au membranes. The analyzed Au membranes have a thickness of 100 nm, 270 nm, 486 nm, 1998 nm, 6712 nm and 11405 nm. (b) Spectral radiative conductance between two Au membranes at a temperature of 300 K, for different thicknesses. (c) Dependence of radiative conductance on temperature, for different thicknesses. (d) The ratio between the radiative conductance computed using FED to that from basic FF-RHT theory (by treating the Au membranes as black bodies) as a function of temperature. The legend shown in the inset of b applies to b-d.

B.8 Computed HFER and ACER for Gold Membranes

To better understand why the radiative heat transfer between sub-wavelength gold membranes can greatly exceed that from far-field theory assuming blackbodies, we examined the HFER and ACER for the gold membranes (similar to the analysis presented in Figure 3-5 for SiN membranes). The geometry considered by us in this analysis is illustrated in Figure B-10a. Using SCUFF-EM, we calculate the radial component of the Poynting flux due to thermal

radiation out of the left gold membrane. We examine the Poynting flux in the y-z plane, at a radius of 60 μm (to correspond to gap-sizes of 20 μm between the membranes). The origin is set at the volumetric center of the membranes.

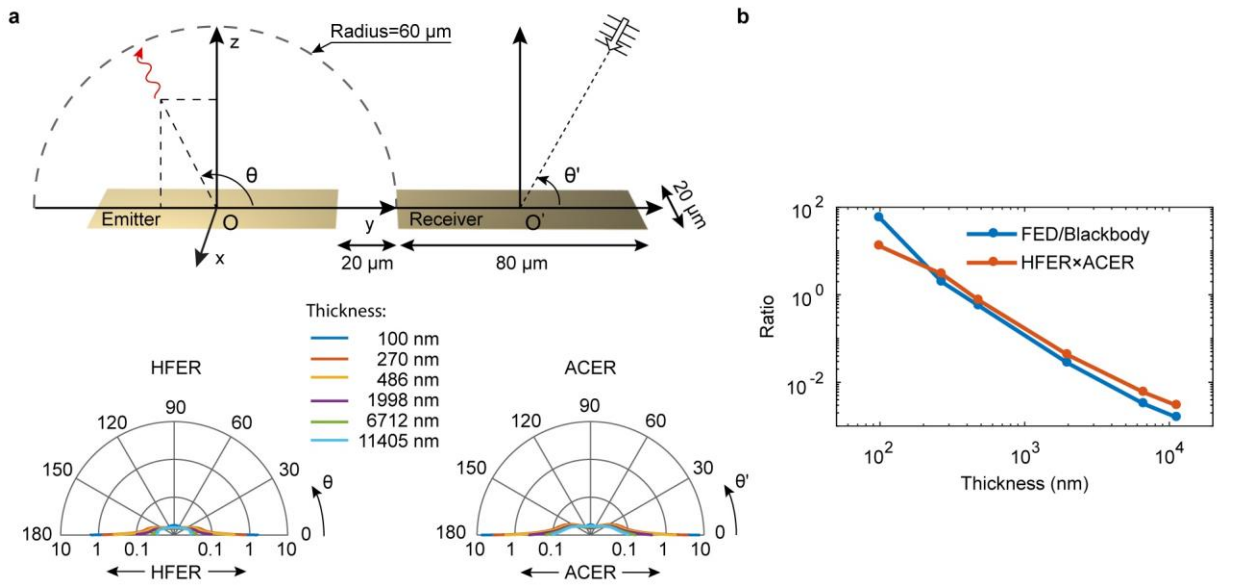

Figure B-10. Enhancement of radiative heat transfer between gold membranes. (a) Schematic of two Au membranes. The Au membranes have a width of 20 μm, a depth of 80 μm, and the gap between the membranes is 20 μm. The radial heat flux from an isolated gold membrane along a circle in y-z plane is computed. We also examine the absorption cross-section of an isolated Au membrane along the same circle in the y-z plane. The ratio between the heat flux calculated using FED and the heat flux evaluated using FF-RHT is shown in HFER polar plot. The ratio between the absorption cross-section calculated using FED and the geometrical cross section at different angles is shown in the ACER polar plot. All calculations were performed for a temperature of 300 K. (b) The enhancement of RHT using FED compared with FF-RHT (treating the Au membranes as blackbodies), for various thicknesses (blue points). The red points denote the product of HFER and ACER.

We observe that both HFER and ACER are strongly enhanced in the in-plane direction for thin gold membranes. For the thinnest case, in the in-plane direction, the HFER is over unity, and its ACER can reach around 10. As the gold membranes thicken, the enhancement in the in-plane direction quickly reduces. For thick gold membranes, both HFER and ACER are much smaller than unity. Figure B-10b shows that the ratio of RHT computed using BEM to that of the

far-field theory (assuming Au to be blackbodies) matches well with the multiplication of the HFER and ACER. Thus, the enhancement of the RHT in Au membranes can be understood by considering both the enhanced heat flux and absorption cross-section in the in-plane direction.

B.9 Analysis of the Contribution of the Pt lines to RHT

To make the BEM computations tractable we neglected the Pt lines in our BEM analysis of $G_{\text{eff, rad}}$. The radiative heat transfer due to the Pt lines is for most cases much smaller than the heat transfer between SiN structures, and, in general, can be neglected. However, as we show below, for the thinnest devices, especially at low temperature, the Pt lines, which contribute several pW/K to the radiative conductance, can readily dominate the radiative conductance.

To evaluate the contribution of Pt lines, we analyzed the RHT between parallel Pt lines for the geometry shown in Figure B-11a. In this analysis, the width of the Pt line was chosen to be 1 μm, matching the width of the Pt lines integrated into the devices employed in our experiments. The distance between the Pt lines was chosen to be 49 μm, which represents the distance between the closest pair of Pt lines on the long beams of the emitter and receiver devices. Finally, we varied the length of the Pt lines from 5 μm to 80 μm. The thickness of the Pt lines was chosen to be 30 nm to correspond well with the thickness of the Pt lines employed in our devices. The dielectric function for Pt was obtained from Ref. [174].

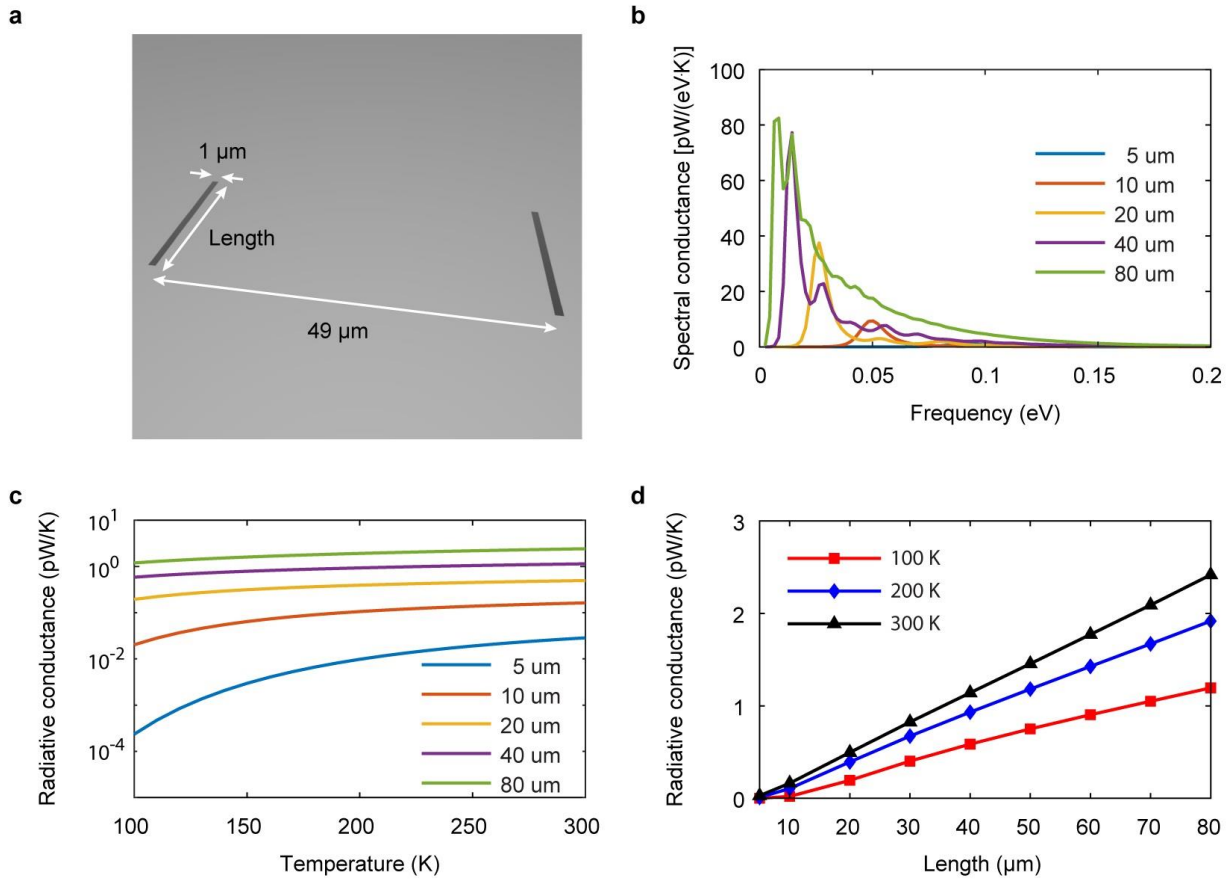

Figure B-11. Analysis of radiative heat transfer between parallel Pt lines. (a) Geometry of two parallel Pt lines. The Pt lines have a width of 1 μm, and variable lengths, and are separated by a vacuum gap of 49 μm. The thickness of the Pt line is chosen to be 30 nm. (b) The spectral radiative conductance between Pt lines with different lengths, at a temperature of 300 K. (c) Temperature-dependence of radiative conductance between Pt lines as the length is varied. (d) Length dependence of radiative conductance between Pt lines.

Figure B-11b shows the spectral radiative conductances for five lengths, which show pronounced peaks. As the length increases, the frequency for the main peak is red-shifted to longer wavelengths. Further, as the length increases, the spectral radiative conductance generally increases. The computed radiative conductances as a function of temperature are shown in Figure B-11c. It can be seen that the radiative conductance between these extremely thin Pt lines can be quite large. For example, at 100 K, the radiative conductance between 80 μm long Pt lines

exceeds 1 pW/K. Importantly, one can also see that for the long Pt lines, the radiative conductance is relatively insensitive to temperature. For example, for the 80 μm long Pt lines, the radiative conductance is only halved when temperature drops from 300 K to 100 K. Such insensitivity of radiative conductance to temperature is dramatically different from the strong temperature dependence of the radiative conductance between SiN structures. This behavior can be understood by noting that the spectral radiative conductance between the Pt lines peaks in the far infrared, and occurs at wavelengths much longer than the peaks in heat transfer of SiN structures (compare Figure B-11b to Figure 3-4c).

To keep the calculations manageable, we have not computed the heat transfer between Pt lines longer than 80 μm. However, from the length dependence of RHT shown in Figure B-11d it can be seen that the radiative conductance scales linearly with the length of the Pt lines. For example, at 100 K, one may estimate the radiative conductance between 400 μm long Pt lines (the length of the long support beams in the experiment) to be ~6 pW/K. Note, for simplicity, we assumed that the Pt lines do not feature any temperature gradients.

The results of the above analysis, when combined with the fact that there are several pairs of parallel Pt lines in the devices, suggest that the overall contribution of the Pt lines to RHT can be several pW/K even at temperatures as low as 100 K. This can at least partly explain the difference between the experimental results and the FED simulations presented in Ch. 3.

B.10 Orientation Effects of Radiative Conductance between Pt Lines

In addition to the Pt lines on the beams, which are parallel to each other, our devices also feature Pt lines that are oriented collinear with respect to each other. Here, we compare the radiative conductance between parallel Pt lines and collinear Pt lines and show that RHT between collinear Pt lines is negligible in comparison to that of parallel lines. Figure B-12a

shows the geometry of two parallel Pt lines, whereas Figure B-12b shows the geometry of two collinear Pt lines. The vacuum gap size between the closest points in both cases are maintained to be 49 μm. The chosen gap-size reflects the parameters of the actual experiment.

In Figure B-12c, we show the spectral conductance for the two orientations at a temperature of 300 K. We observe that the parallel case has much larger spectral conductance than the collinear one. Specifically, one can see from Figure B-12d that the radiative conductance for the parallel case is over one order of magnitude larger than that for the collinear case. This analysis clearly suggests that the contributions between collinear lines can be neglected.

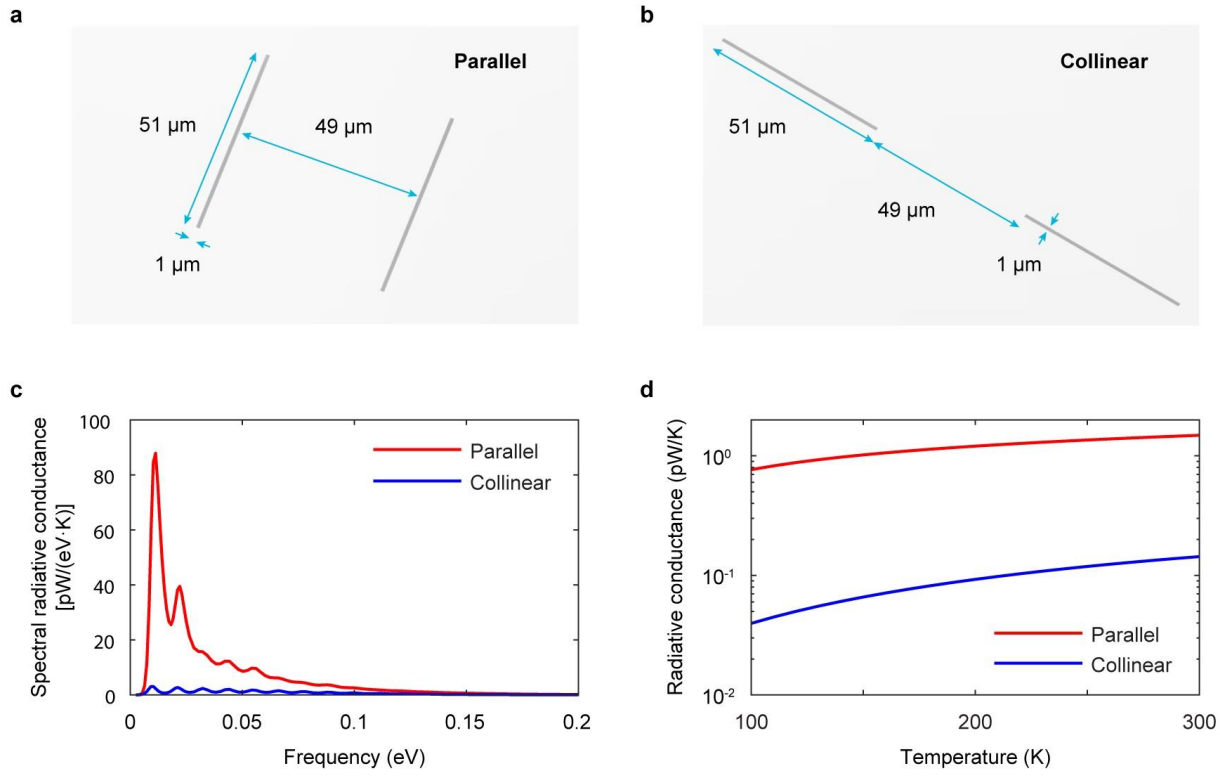

Figure B-12. Orientation effects of radiative heat transfer between Pt lines. (a) Geometry of two parallel Pt lines, separated by a distance of 49 μm. (b) Geometry of two collinear Pt lines. The dimensions of the Pt lines are the same as in a. (c) The spectral radiative conductance for the parallel and collinear cases, at a temperature of 300 K. (d) The radiative conductance for the parallel and collinear cases, as a function of temperature.

B.11 Assessment of the Contribution of Near-Field Effects to the Measured $G_{\text{rad, eff}}$

To assess the contribution of the near-field effects to RHT in our devices, we estimated the contributions of evanescent waves using proximity theory following previous work [175]. We first computed the contribution of evanescent waves to RHT between two SiN semi-infinite spaces, separated by a vacuum gap from the following expression, which gives the heat transfer coefficient per unit area (h_{NF}):

$$h_{\text{NF}}(T,d)=\int_0^\infty \frac{d\omega}{4\pi^2}\frac{\partial}{\partial T}\left[\frac{\hbar\omega}{e^{\hbar\omega/k_BT}-1}\right]\int_{\omega/c}^\infty dkk\left[\tau_s(\omega,k)+\tau_p(\omega,k)\right] \tag{B-7}$$

where, ω is the angular frequency of the radiation, k is the magnitude of the wavevector component parallel to the planes, T is the absolute temperature, d is the gap size, and τ_s and τ_p are the transmission coefficients for the transverse electric (TE) and transverse magnetic (TM) waves, respectively. The transmission is given by:

$$t_{a=s,p}(w,k)=\frac{4\,\text{Im}\left\{R_a^e\right\}\,\text{Im}\left\{R_a^r\right\}e^{-2\,\text{Im}\{q_{vac}\}d}}{\left|D_a\right|^2},\ \text{for}\ k\ ³\ w/c \tag{B-8}$$

where $D_\alpha=1-R_\alpha^eR_\alpha^re^{2iq_{vac}d}$ and q_{vac} is the magnitude of the vacuum wavevector component normal to the planes. Further, $r_s^{ij}=\dfrac{q_i-q_j}{q_i+q_j}$ and $r_p^{ij}=\dfrac{\varepsilon_jq_i-\varepsilon_iq_j}{\varepsilon_jq_i+\varepsilon_iq_j}$. Here, the subscripts i and j represent adjacent layers, $q_i=\sqrt{\varepsilon_i\omega^2/c^2-k^2}$ is the magnitude of the normal wavevector component in layer i, and ε_i is the corresponding material dielectric function. For the case of two semi-infinite SiN objects separated by a vacuum gap, the indices i and j vary from 1 to 3 (1 for the emitter, 2 for the gap and 3 for the receiver), and we have $R_\alpha^e=r_\alpha^{21}$ and $R_\alpha^r=r_\alpha^{23}$.

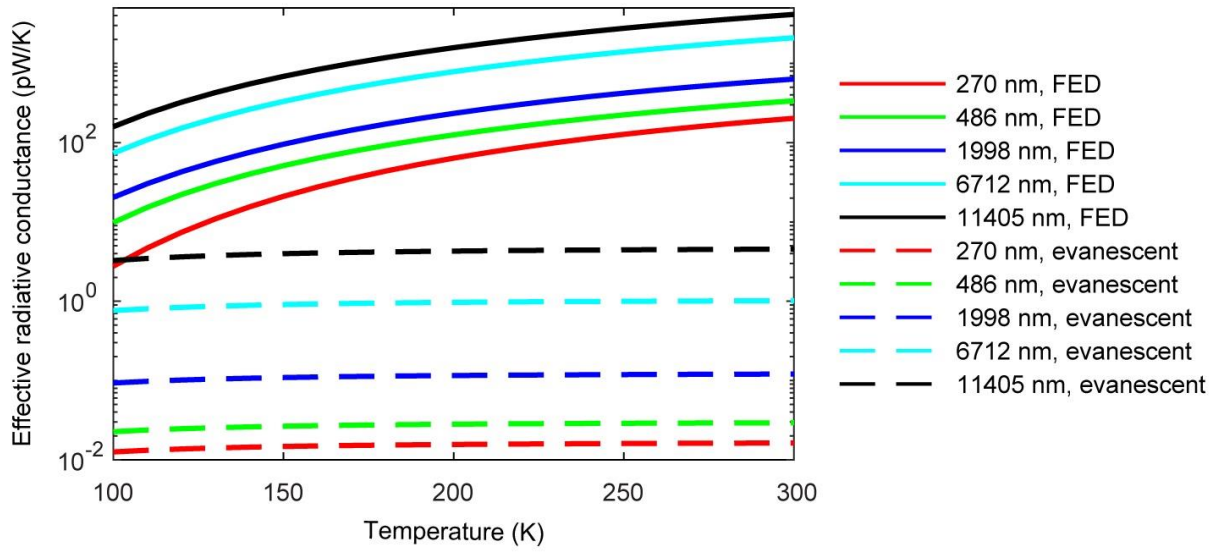

Figure B-13. Quantification of near-field contributions. Comparison of effective radiative conductances evaluated using FED with the evanescent wave contribution evaluated using the proximity approximation.

Next, we used the proximity approximation, to evaluate the near-field contribution to thermal conductance $G_{\mathrm{NF}} = h_{\mathrm{NF}} A$, where A is the area of cross-section of the membranes and the beams. We note that in our proximity approximation-based calculations we account for the beams, the temperature gradient on the emitter's beams, and the spatial distribution of the RHT in the receiver.

In Figure B-13, we present the effective radiative conductance for the five devices using FED and using the proximity approximation for the near-field (evanescent wave) contribution at various temperatures (T). We observe that for all devices, the near-field contribution is negligible, compared with the effective radiative conductance calculated using FED. In fact, the contribution of the evanescent wave to the heat transfer is at most around 2% (at the lowest temperatures) for all the devices and all temperatures that are relevant to this study. Thus, it is clear that the phenomenon observed in this study is not due to near-field radiation effects.

B.12 Dispersion Relations for SiN Slabs

To understand the modes that are responsible for RHT between the SiN membranes, we analyze the dispersion relation of guided modes. In this analysis we consider a slab of SiN with a thickness equal to the thickness of the suspended membrane, as shown in Figure B-14a. The material faces a vacuum on both sides and has an isotropic dielectric permittivity and unity magnetic permeability. When the relative permittivity exceeds unity, the system supports guided waves. For such guided modes, the field profile decays exponentially outside the slab, but features propagating waves inside the slab. By enforcing the continuity of impedance across the vacuum-slab interface, one can solve the dispersion relation. The dispersion relations for different modes can be found in Ref. [147].

We note that when the relative permittivity ϵ is larger than unity, the slab supports at least one branch each of the fundamental TE and TM modes. As the thickness increases, the number of supported guided modes increases. In fact, the number of branches of both the TE guided modes and the TM guided modes, for this slab, is given by $1+[\frac{\text{thickness}}{\lambda}\sqrt{\epsilon - 1}]$, where λ is the wavelength in vacuum, ϵ is the relative permittivity of the slab material, and ($[x]$) denotes the largest integer that does not exceed a real number x.

As can be seen in Figure B-14b-e, for the thinner structures there is always at least one branch each for TE and TM modes. Importantly, the dispersion relation for TE modes is highly dispersive at a frequency of around 0.1 eV (resulting in a large density of states), which aligns with the peak of radiative heat transfer (see Figure 3-4c). As the thickness increases, more branches of guided modes are supported over a broad range of frequencies and accordingly the spectral selectivity is reduced.

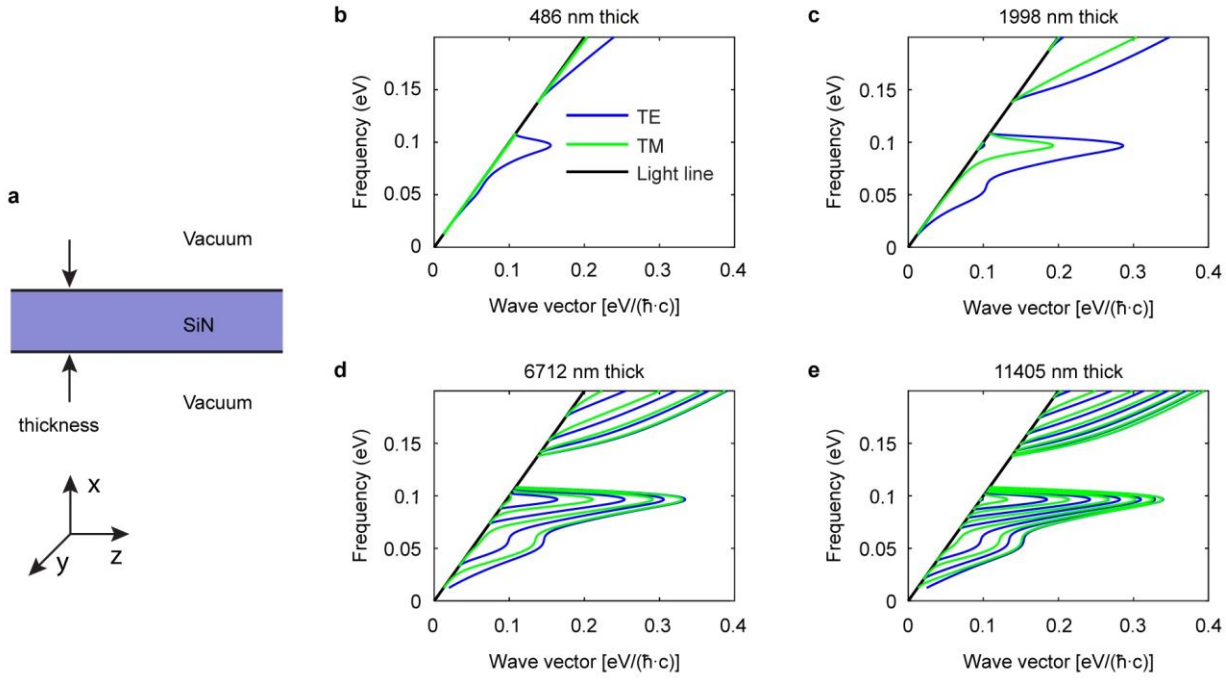

Figure B-14. Dispersion relation of guided modes in a SiN slab. (a) Geometry of a SiN slab surrounded by vacuum on both sides. (b)-(e) Dispersion relation for the guided modes in the slab with a thickness of (b) 486 nm, (c) 1998 nm, (d) 6712 nm, and (e) 11405 nm. The transverse-electric (TE) guided modes have the electric field oriented in y-direction, and are shown as blue lines. The transverse-magnetic (TM) guided modes have the magnetic field oriented in the y-direction, and are denoted by green lines. The light line is shown in black.

Finally, we contrast our observations to those from past work [98] on near-field RHT, where surface polaritons are typically found to dominate the RHT when the gap size is much smaller than the thermal wavelength. However, surface modes do not make significant contributions to the observed far-field enhancements, as is reflected in the lack of alignment in the calculated spectral conductances and the density of states of surface modes (not shown here).

B.13 Evaluating the Effect of Deviations from Planarity

As shown in Figure 3-1 and Figure 3-7, the devices employed in the experiments show small deviations from planarity. These deviations increase the projected area by a small fraction (~50 % for the thinnest devices and even smaller values for thicker ones), Thus, they have an

insignificant effect on the predictions of basic FF-RHT theory and therefore cannot explain the dramatic differences between predictions of basic FF-RHT theory and measurement. However, one may ask if the predictions of FED would be affected if the deviations from planarity are accounted for. Since it is challenging to model the exact curved geometry of the membranes we evaluate the effect of imperfections by modeling *scenarios* where the membranes are tilted (see Figure B-15a). Specifically, we consider the case of 270 nm thick membranes and vary the tilt angle from 0˚ to 20˚ and evaluate $G_{\text{rad, eff}}$ as a function of tilt angle. Note that the increase in the projected area of the emitter as seen from the receiver and *vice versa*, even for a 1˚ tilt is much larger than the increase in the projected area due to the imperfections in the devices. The computed spectral conductances as a function of tilt angle are shown in Figure B-15b. It can be seen that even for a tilt as large as 5˚ there is very little change in the spectral conductance. Significant changes are only seen when the tilt exceeds 10˚. The computed $G_{\text{rad, eff}}$ as a function of tilt angle (Figure B-15c) confirms this expectation.

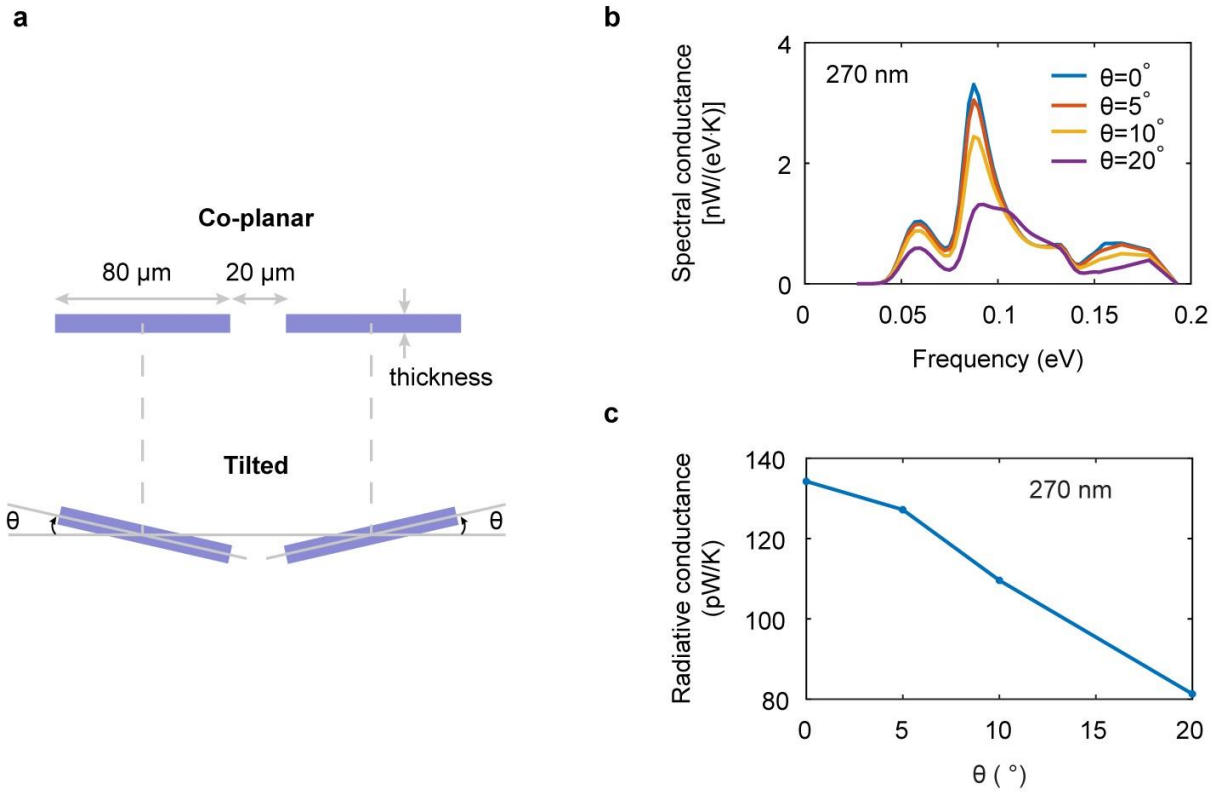

Figure B-15. Effect of tilting on the radiative conductance. (a) Schematic cross-section of two rectangular SiN membranes. The membranes have transverse dimensions of 80 μm by 60 μm. There is a 20 μm gap between the two membranes in the co-planar configuration. In our analysis each membrane is tilted by the same angle around its center of mass (as shown in panel a). (b) Spectral radiative conductance between 270 nm thick membranes as a function of tilt angle. (c) Radiative conductance between 270 nm thick membranes as a function of tilt.

Finally, to experimentally confirm the FED predictions of Figure B-15 we measured $G_{rad,\,eff}$ for devices featuring tilted SiN membranes. Fabrication of the desired devices was accomplished by first etching from the front side a thin slit into the SiN layer (270 nm thick) on the substrate (Figure B-16a) via RIE. Subsequently, KOH was used to etch through the silicon handle to release the suspended devices. Because KOH preferentially etches convex corners at a faster rate, the KOH release step produced a large undercut of the silicon handle layer beneath the SiN layer surrounding the opening of the slit. Due to stresses in the SiN layer, the free hanging SiN becomes warped and tilts. This fabrication technique produced suspended devices

(Figure B-16a, b) with a well characterized tilt of 11º (tilt angle characterized by LSCM, see Figure B-16d, e). Data from experiments performed on these devices are shown in Figure B-16c (red dots), where we plot the temperature rise of the receiver membrane as a function of the temperature rise of the emitter membrane. For comparison, data are also shown for untilted devices (black squares).

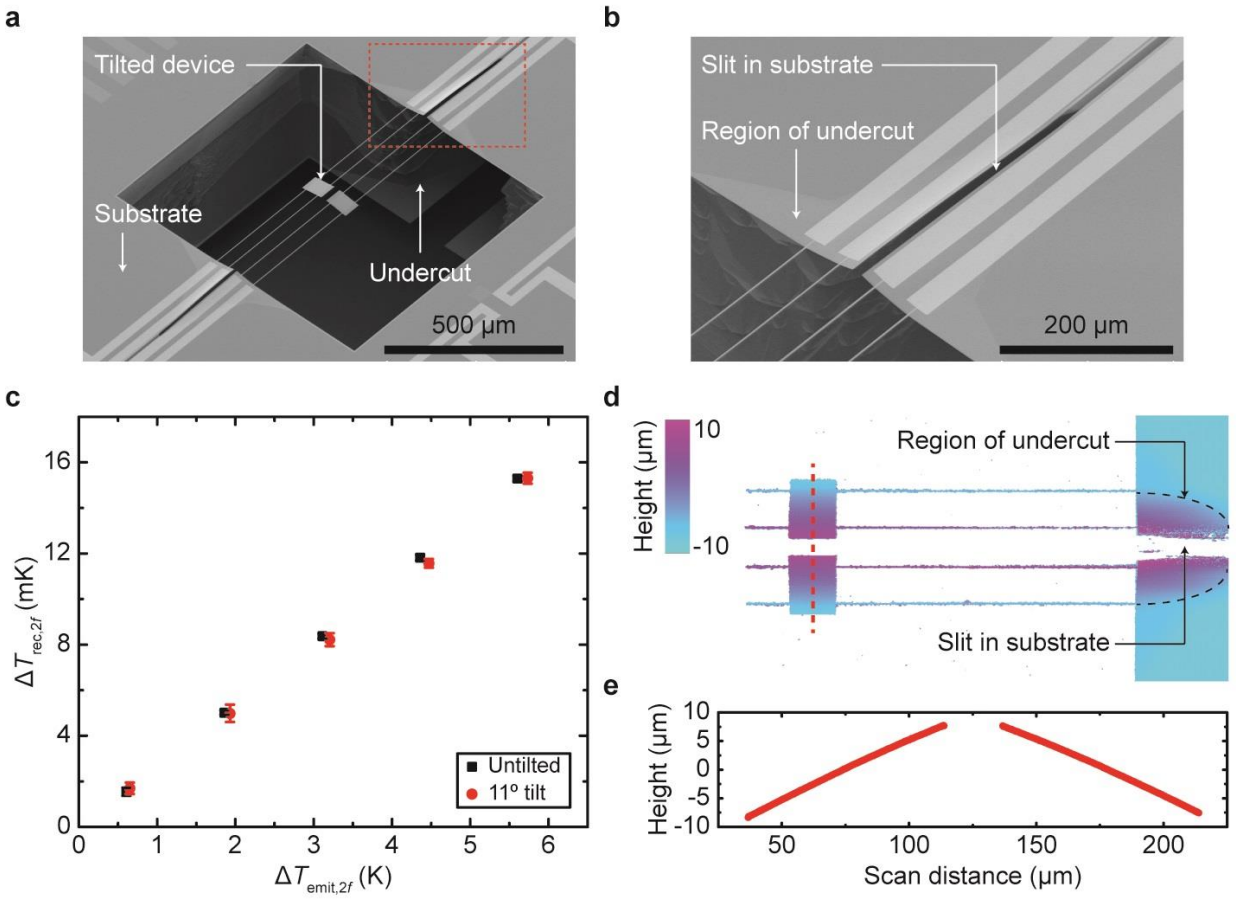

Figure B-16. Experimental verification of the effect of tilt on the radiative conductance. (a) Scanning electron microscope (SEM) images of devices featuring a tilt angle. (b) SEM of the region marked by the rectangular box in panel a. The warping in the undercut regions can be seen. (c) The measured temperature rise of the receiver membrane as a function of the temperature rise of the emitter membrane for untilted (black squares), and 11º tilted (red dots) devices at 300 K. Device thicknesses are 270 nm in both cases. (d) Confocal microscope scan showing the surface height of the 270 nm thick suspended devices and the substrate to which they are affixed. It is clear that the SiN film on the substrate is warped near the narrow slit in the substrate due to undercut of the underlying silicon handle layer. As a result, the suspended devices are tilted by 11º. (e) Height profile of the suspended devices along the dashed line indicated in d.

From these data it can be seen that the receiver temperature rise, for a given emitter temperature rise, is slightly smaller for devices featuring a tilt. Specifically, the $G_{\text{rad, eff}}$ for tilted devices is 206 ± 2 pW/K at room temperature, which is reduced by 13 pW/K when compared to the conductance between untilted devices (219 ± 1 pW/K). These experimental observations combined with our FED analysis provide unambiguous evidence that the small imperfections in our devices have no influence on the central conclusions of the work.

B.14 Computed Gap-Dependence of the Radiative Conductance of Membranes

To illustrate the impact of gap-size on the RHT between SiN membranes we performed systematic calculations. For simplicity we did not include beams in this analysis. Specifically, the gap-size was varied from 20 μm to 1 cm in our calculations. Figure B-17a shows the spectral conductance for 270 nm thick membranes at different gap-sizes, at a temperature of 300 K. It can be seen that the heat transfer spectra at different gaps feature similar shapes. Further, the magnitude of radiative conductance reduces as the gap-size increases. In order to understand how large the deviations from FF-RHT theory are as a function of gap-size, we present in Figure B-17b the ratio of radiative conductance obtained from FED to that from far-field theory assuming blackbodies, as a function of gap-size. It is found that, as gap-size increases, the ratio of FED to blackbody conductance increases until it plateaus at about 1500 when the gap-size reaches ~1 mm. Thus, one can expect orders of magnitude exceedances over the predictions of basic FF-RHT theory over a large range of gap-sizes.

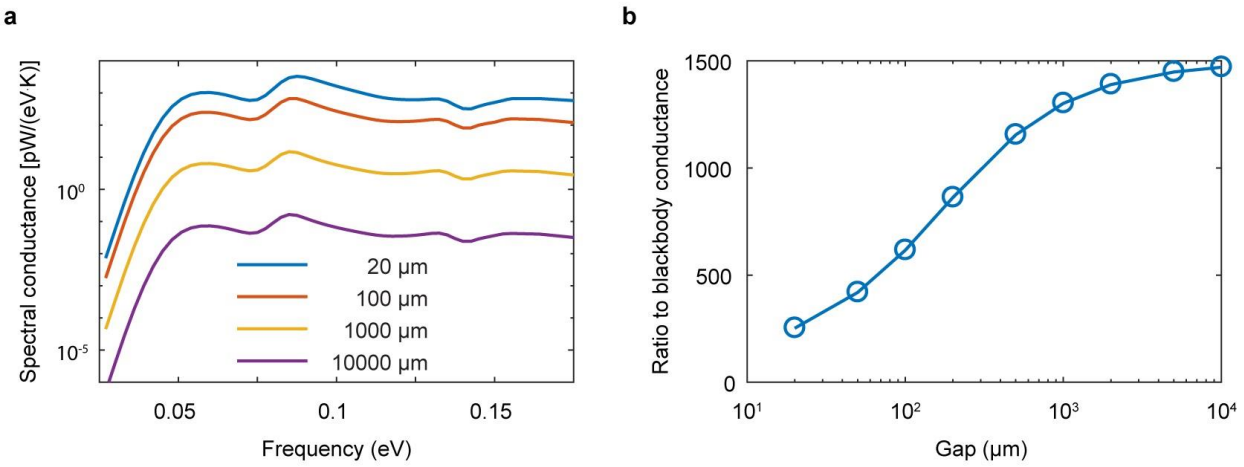

Figure B-17. Gap-dependence of the radiative conductance. (a) Spectral radiative conductance between two 270 nm thick SiN membranes for different gaps at 300 K. The transverse dimensions of each membrane are 80 μm by 60 μm. (b) Ratio of radiative conductance computed using FED to that from basic FF-RHT theory (treating the membranes as blackbodies) as a function of gap size. The temperature of the membranes is assumed to be 300 K. Note, for simplicity the supporting beams that are present in our devices were not included in this analysis.

B.15 Measured Gap-Dependence of the Enhancement of Radiative Conductance for Devices with Beams and Comparison with FED Calculations

We performed additional experiments to analyze the gap dependence of the radiative conductance between SiN membranes. For these experiments, we fabricated 520 nm-thick membranes with various gap sizes ranging from 20 μm to 750 μm. As shown in Figure B-18, the measured radiative conductance between these membranes (blue circles) exceeds the estimated blackbody conductance (black triangles) by a factor of ~40 for the entire range of gap sizes investigated. These measured results also agree very well with FED simulations (red circles). Here, the blackbody conductance and FED conductance were both computed by accounting for the exact geometry of the devices including the beams. The experimental data presented in Figure B-18 unambiguously demonstrates that large enhancements in radiative heat transfer between sub-wavelength membranes can be achieved even for macroscopically large gaps.

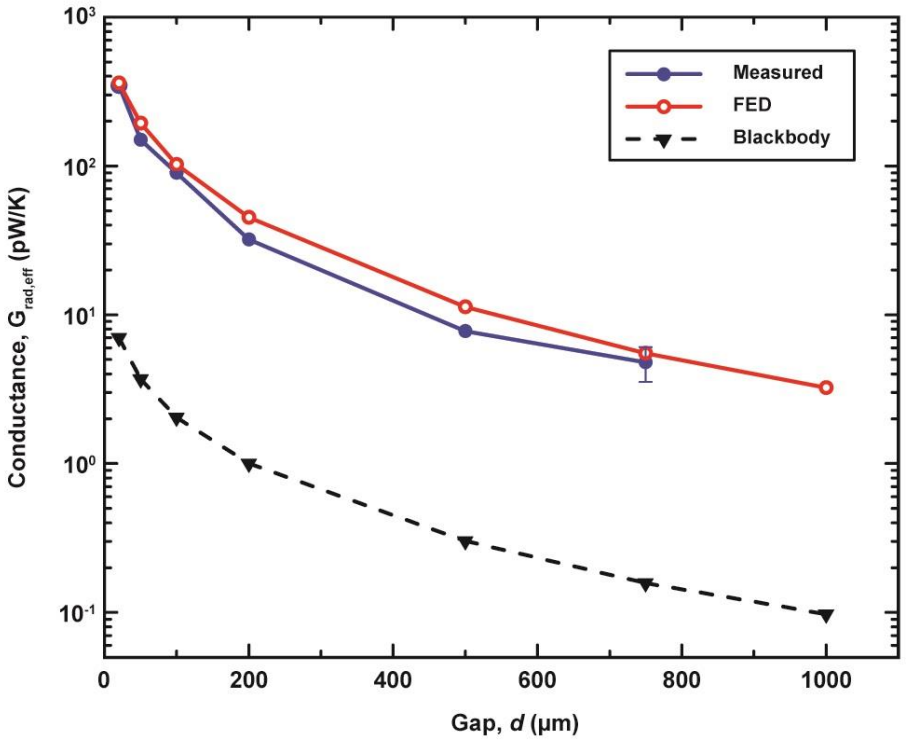

Figure B-18. Radiative conductance between 520 nm-thick membranes at room temperature. Various sets of 520 nm-thick SiN membranes were fabricated with gaps ranging from 20 μm to 750 μm. For each gap, the measured conductance (blue solid circles) is compared with the fluctuational electrodynamics (FED) simulation (red open circles), and the blackbody conductance (black triangles) as computed using COMSOL.

References

[1] Herschel, W., *Experiments on the refrangibility of the invisible rays of the Sun.* Philosophical Transactions of Royal Society of London. **90**, 284-292, (1800).

[2] Herschel, W., *Experiments on the solar, and on the terrestrial rays that occasion heat; with a comparative view of the laws to which light and heat, or rather rays which occasion them, are subject, in order to determine whether they are the same, or different. Part I.* Philosophical Transactions of Royal Society of London. **90**, 293-326, (1800).

[3] Herschel, W., *Experiments on the solar, and on the terrestrial rays that occasion heat; with a comparative view of the laws to which light and heat, or rather rays which occasion them, are subject, in order to determine whether they are the same, or different. Part II.* Philosophical Transactions of Royal Society of London. **90**, 437-538, (1800).

[4] Barr, E.S., *Historical survey of the early development of the infrared spectral region.* Americal Journal of Physics. **28**, 42-54, (1960).

[5] Bohm, D., *Quantum theory*. (New York: Prentice-Hall, Inc., 1951).

[6] Planck, M.K.E.L., *Über eine verbesserung der wienschen spectralgleichung.* Verhandl. Dtsc. Phys. Ges. **2**, 202, (1900).

[7] Planck, M.K.E.L., *Zur theorie des gesetzes der energieverteilung im normalspectrum.* Verhandl. Dtsc. Phys. Ges. **2**, 237, (1900).

[8] Modest, M.F., *Radiative heat transfer*. 3rd ed., xxii, 882 pages (New York: Academic Press, 2013).

[9] Planck, M. and M. Masius, *The theory of heat radiation*. xiv, p., 1 l., 225 p. diagrs. (Philadelphia: P. Blakiston's Son & Co., 1914).

[10] Rytov, S.M., *Theory of electric fluctuations and thermal radiation*. 1953, Air Force Cambride Research Center: Bedford, MA.

[11] Rytov, S.M., I.A. Kravtsov, and V.I. Tatarskii, *Principles of statistical radiophysics*. 2. rev. and enl. ed. (Berlin ; New York: Springer-Verlag, 1987).

[12] Polder, D. and M. Van Hove, *Theory of radiative heat transfer between closely spaced bodies.* Physical Review B. **4**, 3303-3314, (1971).

[13] Callen, H.B. and T.A. Welton, *Irreversibility and generalized noise.* Physical Review. **83**, 34-40, (1951).

[14] Cahill, D.G., et al., *Nanoscale thermal transport. II. 2003 - 2012.* Applied Physics Reviews. **1**, 011305, (2014).

[15] Gall, D., *Electron mean free path in elemental metals.* Journal of Applied Physics. **119**, 085101, (2016).

[16] McCauley, A.P., et al., *Modeling near-field radiative heat transfer from sharp objects using a general three-dimensional numerical scattering technique.* Physical Review B. **85**, 165104, (2012).

[17] Rodriguez, A.W., M.H. Reid, and S.G. Johnson, *Fluctuating-surface-current formulation of radiative heat transfer for arbitrary geometries.* Physical Review B. **86**, 220302, (2012).

[18] Rodriguez, A.W., et al., *Frequency-selective near-field radiative heat transfer between photonic crystal slabs: A computational approach for arbitrary geometries and materials.* Physical Review Letters. **107**, 114302, (2011).
[19] Reid, M.T.H., A.W. Rodriguez, and S.G. Johnson, *Fluctuation-induced phenomena in nanoscale systems: Harnessing the power of noise.* Proceedings of the IEEE. **101**, 531-545, (2013).
[20] Bimonte, G., *Scattering approach to Casimir forces and radiative heat transfer for nanostructured surfaces our of thermal equilibrium.* Physical Review A. **80**, 042102, (2009).
[21] Narayanaswamy, A. and G. Chen, *Thermal near-field radiative transfer between two spheres.* Physical Review B. **77**, 075125, (2008).
[22] Emslie, A.G., in *Aerodynamically Heated Structures*, P.E. Glaser, Editor. 1962, Prentice-Hall.
[23] Bijl, D., *Note on thermal radiation at low temperatures.* The London, Edinburgh, and Dublin Philosophical Magazine and Journal of Science. **43**, 1342-1344, (1952).
[24] Domoto, G., R. Boehm, and C.L. Tien, *Experimental investigation of radiative transfer between metallic surfaces at cryogenic temperatures.* Journal of Heat Transfer. **92**, 412-416, (1970).
[25] Pendry, J.B., *Radiative exchange of heat between nanostructures.* Journal of Physics: Condensed Matter. **11**, 6621-6633, (1999).
[26] Mulet, J.P., et al., *Nanoscale radiative heat transfer between a small particle and a plane surface.* Applied Physics Letters. **78**, 2931, (2001).
[27] Mulet, J.P., et al., *Enhanced radiative heat transfer at nanometric distances.* Microscale Thermophysical Engineering. **6**, 209-222, (2002).
[28] Fu, C.J. and Z.M. Zhang, *Nanoscale radiation heat tarnsfer for silicon at different doping levels.* International Journal of Heat and Mass Transfer. **49**, 1703-1718, (2006).
[29] Rousseau, E., M. Laroche, and J.J. Greffet, *Radiative heat transfer at nanoscale mediated by surface plasmons for highly doped silicon.* Applied Physics Letters. **95**, 231913, (2009).
[30] Shen, S., A. Narayanaswamy, and G. Chen, *Surface phonon polaritons mediated energy transfer between nanoscale gaps.* Nano Letters. **9**, 2909-2913, (2009).
[31] Craig, F.B., F. Bohren, and D.R. Huffman, *Absorption and scattering of light by small spheres*. (New York: John Wiley & Sons, 1983).
[32] Kattawar, G. and M. Eisner, *Radiation from a homogeneous isothermal sphere.* Applied Optics. **9**, 2685-2690, (1970).
[33] Liu, X., et al., *Infrared spatial and frequency selective metamaterial with near-unity absorbance.* Physical Review Letters. **104**, 207403, (2010).
[34] Zhu, L., et al., *Temporal coupled mode theory for thermal emission from a single thermal emitter supporting either a single mode or an orthogonal set of modes.* Applied Physics Letters. **102**, 103104, (2013).
[35] Liu, B., et al., *Perfect thermal emission by nanoscale transmission line resonators.* Nano Letters. **17**, 666-672, (2017).
[36] Bimonte, G., et al., *Polarized thermal emission by thin metal wires.* New Journal of Physics. **11**, 033014, (2009).

[37] Joulain, K., et al., *Surface electromagnetic waves thermally excited: Radiative heat transfer, coherence properties and Casimir forces revisited in the near field.* Surface Science Reports. **57**, 59-112, (2005).
[38] Liu, X.L., R.Z. Zhang, and Z.M. Zhang, *Near-field radiative heat transfer with doped-silicon nanostructured metamaterials.* International Journal of Heat and Mass Transfer. **73**, 389-398, (2014).
[39] Francoeur, M., S. Basu, and S.J. Petersen, *Electric and magnetic surface polariton mediated near-field radiative heat transfer between metamaterials made of silicon carbide particles.* Optics Express. **19**, 18774-18788, (2011).
[40] Jahani, S. and Z. Jacob, *All-dielectric metamaterials.* Nature Nanotechnology. **11**, 23-36, (2016).
[41] Biehs, S.-A., et al., *Nanoscale heat flux between nanoporous materials.* Optics Express. **19**, A1088-A1103, (2011).
[42] Song, B., et al., *Enhancement of near-field radiative heat transfer using polar dielectric thin films.* Nature Nanotechnology. **10**, 253-258, (2015).
[43] Boriskina, S.V., et al., *Enhancement and tunability of near-field radiative heat transfer mediated by surface plasmon polaritons in thin plasmonic films.* Photonics. **2**, 659-683, (2015).
[44] Ilic, O., et al., *Overcoming the black body limit in plasmonic and graphene near-field thermophotovoltaic systems.* Optics Express. **20**, A366-A384, (2012).
[45] Svetovoy, V., P. Van Zwol, and J. Chevrier, *Plasmon enhanced near-field radiative heat transfer for graphene covered dielectrics.* Physical Review B. **85**, 155418, (2012).
[46] Messina, R. and P. Ben-Abdallah, *Graphene-based photovoltaic cells for near-field thermal energy conversion.* Scientific Reports. **3**, (2013).
[47] Svetovoy, V. and G. Palasantzas, *Graphene-on-silicon near-field thermophotovoltaic cell.* Physical Review Applied. **2**, 034006, (2014).
[48] Van Zwol, P., et al., *Fast nanoscale heat-flux modulation with phase-change materials.* Physical Review B. **83**, 201404, (2011).
[49] Van Zwol, P., et al., *Phonon polaritons enhance near-field thermal transfer across the phase transition of VO 2.* Physical Review B. **84**, 161413, (2011).
[50] Yang, Y., S. Basu, and L. Wang, *Radiation-based near-field thermal rectification with phase transition materials.* Applied Physics Letters. **103**, 163101, (2013).
[51] Huang, Y., S.V. Boriskina, and G. Chen, *Electrically tunable near-field radiative heat transfer via ferroelectric materials.* Applied Physics Letters. **105**, 244102, (2014).
[52] Yang, Y. and L. Wang, *Electrically-gated near-field radiative thermal transistor.* arXiv preprint arXiv:1501.00479, (2015).
[53] Moncada-Villa, E., et al., *Magnetic field control of near-field radiative heat transfer and the realization of highly tunable hyperbolic thermal emitters.* Physical Review B. **92**, 125418, (2015).
[54] Zhu, L. and S. Fan, *Persistent directional current at equilibrium in nonreciprocal many-body near field electromagnetic heat transfer.* Physical Review Letters. **117**, 134303, (2016).
[55] Ekeroth, R.M.A., et al., *Anisotropic thermal magnetoresistance for an active control of radiative heat transfer.* ACS Photonics. **5**, 705-710, (2018).
[56] Schwede, J.W., et al., *Photon-enhanced thermionic emission for solar concentrator systems.* Nature Materials. **9**, 762, (2010).

[57] Lee, J.-H., et al., *Optimal emitter-collector gap for thermionic energy converters.* Applied Physics Letters. **100**, 173904, (2012).
[58] Fang, J., H. Frederich, and L. Pilon, *Harvesting nanoscale thermal radiation using pyroelectric materials.* Journal of Heat Transfer. **132**, 092701, (2010).
[59] Pandya, S., et al., *Pyroelectric energy conversion with large energy and power density in relaxor ferroelectric thin films.* Nature Materials. **17**, 432-438, (2018).
[60] Whale, M. and E.G. Cravalho, *Modeling and performance of microscale thermophotovoltaic energy conversion devices.* IEEE Transactions on Energy Conversion. **17**, 130-142, (2002).
[61] Harder, N.P. and P. Wurfel, *Theoretical limits of thermophotovoltaic solar energy conversion.* Semiconductor Science and Technology. **18**, S151, (2003).
[62] Narayanaswamy, A. and G. Chen, *Surface modes for near field thermophotovoltaics.* Applied Physics Letters. **82**, 3544, (2003).
[63] Laroche, M., R. Carminati, and J.J. Greffet, *Near-field thermophotovoltaic energy conversion.* Journal of Applied Physics. **100**, 063704, (2006).
[64] Basu, S., Y.B. Chen, and Z.M. Zhang, *Microscale radiation in thermophotovoltaic devices—a review.* International Journal of Energy Research. **31**, 689-716, (2007).
[65] Guo, Y., et al., *Thermal excitation of plasmons for near-field thermophotovoltaics.* Applied Physics Letters. **105**, 073903, (2014).
[66] Lenert, A., et al., *A nanophotonic solar thermophotovoltaic device.* Nature Nanotechnology. **9**, 126-130, (2014).
[67] Chen, K.F., P. Santhanam, and S.H. Fan, *Suppressing sub-bandgap phonon–polariton heat transfer in near-field thermophotovoltaic devices for waste heat recovery.* Applied Physics Letters. **107**, 091106, (2015).
[68] Tong, J.K., et al., *Thin-film 'thermal well' emitters and absorbers for high-efficiency thermophotovoltaics.* Scientific Reports. **5**, 10661, (2015).
[69] Molesky, S. and Z. Jacob, *Ideal near-field thermophotovoltaic cells.* Physical Review B. **91**, 205435, (2015).
[70] Fiorino, A., et al., *Nanogap near-field thermophotovoltaics.* Nature Nanotechnology (In Press), (2018).
[71] Otey, C.R., W.T. Lau, and S. Fan, *Thermal rectification through vacuum.* Physical Review Letters. **104**, 154301, (2010).
[72] Basu, S. and M. Francoeur, *Near-field radiative transfer based thermal rectification using doped silicon.* Applied Physics Letters. **98**, 113106, (2011).
[73] Zhu, L., C.R. Otey, and S. Fan, *Ultrahigh-contrast and large-bandwidth thermal rectification in near-field electromagnetic thermal transfer between nanoparticles.* Physical Review B. **88**, 184301, (2013).
[74] Wang, L.P. and Z.M. Zhang, *Thermal rectification enabled by near-field radiative heat transfer between intrinsic silicon and a dissimilar material.* Nanoscale and Microscale Thermophysical Engineering. **17**, 337-348, (2013).
[75] Gu, W., G.-H. Tang, and W.-Q. Tao, *Thermal switch and thermal rectification enabled by near-field radiative heat transfer between three slabs.* International Journal of Heat and Mass Transfer. **82**, 429-434, (2014).
[76] Joulain, K., et al., *Radiative thermal rectification between SiC and SiO_2.* Optics Express. **23**, A1388-A1397, (2015).

[77] Ben-Abdallah, P. and S.-A. Biehs, *Near-field thermal transistor.* Physical Review Letters. **112**, 044301, (2014).
[78] Ben-Abdallah, P., et al., *Heat flux splitter for near-field thermal radiation.* Applied Physics Letters. **107**, 053109, (2015).
[79] Ben-Abdallah, P., *Photon thermal hall effect.* Physical Review Letters. **116**, 084301, (2016).
[80] Kryder, M.H., et al., *Heat assisted magnetic recording.* Proceedings of the IEEE. **96**, 1810-1835, (2008).
[81] Challener, W., et al., *Heat-assisted magnetic recording by a near-field transducer with efficient optical energy transfer.* Nature Photonics. **3**, 220-224, (2009).
[82] Stipe, B.C., et al., *Magnetic recording at 1.5 Pb m− 2 using an integrated plasmonic antenna.* Nature Photonics. **4**, 484-488, (2010).
[83] Kittel, A., et al., *Near-field thermal imaging of nanostructured surfaces.* Applied Physics Letters. **93**, 193109, (2008).
[84] Huth, F., et al., *Infrared-spectroscopic nanoimaging with a thermal source.* Nature Materials. **10**, 352-356, (2011).
[85] Garcia, R., A.W. Knoll, and E. Riedo, *Advanced scanning probe lithography.* Nature Nanotechnology. **9**, 577-587, (2014).
[86] Wolf, H., et al., *Sub-20 nm silicon patterning and metal lift-off using thermal scanning probe lithography.* Journal of Vacuum Science & Technology B, Nanotechnology and Microelectronics: Materials, Processing, Measurement, and Phenomena. **33**, 02B102, (2015).
[87] Albisetti, E., et al., *Nanopatterning reconfigurable magnetic landscapes via thermally assisted scanning probe lithography.* Nature nanotechnology. **11**, 545-551, (2016).
[88] Wischnath, U.F., et al., *The near-field scanning thermal microscope.* Review of Scientific Instruments. **79**, 073708, (2008).
[89] Shi, L., et al., *Measuring thermal and thermoelectric properties of one-dimensional nanostructures using a microfabricated device.* Journal of Heat Transfer. **125**, 881-888, (2003).
[90] Wingert, M.C., et al., *Ultra-sensitive thermal conductance measurement of one-dimensional nanostructures enhanced by differential bridge.* Review of Scientific Instruments. **83**, 2012, (2012).
[91] Zheng, J., et al., *Sub-picowatt/kelvin resistive thermometry for probing nanoscale thermal transport.* Review of Scientific Instruments. **84**, 114901, (2013).
[92] Sadat, S., et al., *Room temperature picowatt-resolution calorimetry.* Applied Physics Letters. **99**, 043106, (2011).
[93] Sadat, S., E. Meyhofer, and P. Reddy, *Resistance thermometry-based picowatt-resolution heat-flow calorimeter.* Applied Physics Letters. **102**, 163110, (2013).
[94] Canetta, C. and A. Narayanaswamy, *Sub-picowatt resolution calorimetry with a bi-material microcantilever sensor.* Applied Physics Letters. **102**, 103112, (2013).
[95] Dechaumphai, E. and R. Chen, *Sub-picowatt resolution calorimetry with niobium nitride thin-film thermometer.* Review of Scientific Instruments. **85**, 094903, (2014).
[96] Cahill, D.G., *Thermal conductivity measurement from 30 to 750 K: the 3w methods.* Review of Scientific Instruments. **61**, 802, (1990).

[97] Sadat, S., E. Meyhofer, and P. Reddy, *High resolution resistive thermometry for micro/nanoscale measurements.* Review of Scientific Instruments. **83**, 084902, (2012 Review of Scientific Instruments).
[98] Song, B., et al., *Radiative heat conductances between dielectric and metallic parallel plates with nanoscale gaps.* Nature Nanotechnology. **11**, 509-514, (2016).
[99] Thompson, D., et al., *Hundred-fold enhancement in far-field radiative heat transfer over the blackbody limit.* Nature (In Press), (2018).
[100] Thompson, D., et al., *A novel scheme to gate radiative heat currents.* (In Preparation), (2018).
[101] Rousseau, E., et al., *Radiative heat transfer at the nanoscale.* Nature Photonics. **3**, 514-517, (2009).
[102] Kim, K., et al., *Radiative heat transfer in the extreme near-field.* Nature. **528**, 387-391, (2015).
[103] DiMatteo, R.S., P. Greiff, and S.L. Finberg, *Enhanced photogeneration of carriers in a semiconductor via coupling across a nonisothermal nanoscale vacuum gap.* Applied Physics Letters. **79**, 1894-1896, (2001).
[104] Song, B., et al., *Near-field radiative thermal transport: from theory to experiment.* AIP Advances. **5**, 053503, (2015).
[105] Ganjeh, Y., et al., *A platform to parallelize planar surfaces and control their spatial separation with nanometer resolution.* Review of Scientific Instruments. **83**, 105101, (2012).
[106] Cravalho, E.G., G.A. Domoto, and C.L. Tien. *Measurements of thermal radiation of solids at liquid-helium temperatures*. in *AIAA 3rd Thermophysics Conference*. Los Angeles, CA. (1968).
[107] Hargreaves, C.M., *Anomalous radiative transfer between closely-spaced bodies.* Physics Letters A. **30**, 491-492, (1969).
[108] Ottens, R.S., et al., *Near-field radiative heat transfer between macroscopic planar surfaces.* Physical Review Letters. **107**, 014301, (2011).
[109] Lim, M., S.S. Lee, and B.J. Lee, *Near-field thermal radiation between doped silicon plates at nanoscale gaps.* Physical Review B. **91**, 1915136, (2015).
[110] St-Gelais, R., et al., *Demonstration of strong near-field radiative heat transfer between integrated nanostructures.* Nano Letters. **14**, 6971-6975, (2014).
[111] Biehs, S.A., E. Rousseau, and J.J. Greffet, *Mesoscopic description of radiative heat transfer at the nanoscale.* Physical Review Letters. **105**, 234301, (2010).
[112] Narayanaswamy, A. and Y. Zheng, *A Green's function formalism of energy and momentum transfer in fluctuational electrodynamics.* Journal of Quantitative Spectroscopy and Radiative Transfer. **132**, 12-21, (2014).
[113] Chapuis, P.O., et al., *Effects of spatial dispersion in near-field radiative heat transfer between two parallel metallic surfaces.* Physical Review B. **77**, 035431, (2008).
[114] Chandrasekhar, S., *Radiative transfer*. The International series of monographs on physics. xiv, 393 p. (Oxford,: Clarendon Press, 1950).
[115] Reipurth, B., D. Jewitt, and K. Keil, *Protostars and planets V*. The University of Arizona space science series. xxiv, 951 p.University of Arizona Press, 2007).
[116] Raman, A.P., et al., *Passive radiative cooling below ambient air temperature under direct sunlight.* Nature. **515**, 540-544, (2014).

[117] Guler, U., A. Boltasseva, and V.M. Shalaev, *Refractory Plasmonics.* Science. **344**, 263-264, (2014).
[118] Fernández-Hurtado, V., et al., *Super-Planckian far-field radiative heat transfer.* arXiv:1708.06191, (2017).
[119] Golyk, V.A., M. Krüger, and M. Kardar, *Heat radiation from long cylindrical objects.* Physical Review E. **85**, 046603, (2012).
[120] Biehs, S.-A. and P. Ben-Abdallah, *Revisiting super-Planckian thermal emission in the far-field regime.* Physical Review B. **93**, 165405, (2016).
[121] Au, Y.-Y., et al., *Thermal radiation spectra of individual subwavelength microheaters.* Physical Review B. **78**, 085402, (2008).
[122] Schuller, J.A., T. Taubner, and M.L. Brongersma, *Optical antenna thermal emitters.* Nature Photonics. **3**, 658-661, (2009).
[123] Wuttke, C. and A. Rauschenbeutel, *Thermalization via heat radiation of an individual object thinner than the thermal wavelength.* Physical Review Letters. **111**, 024301, (2013).
[124] Hochbaum, A.I., et al., *Enhanced thermoelectric performance of rough silicon nanowires.* Nature. **451**, 163-167, (2008).
[125] Kim, P., et al., *Thermal transport measurements of individual multiwalled nanotubes.* Physical Review Letters. **87**, 215502, (2001).
[126] St-Gelais, R., et al., *Near-field radiative heat transfer between parallel structures in the deep subwavelength regime.* Nature Nanotechnology. **11**, 515-519, (2016).
[127] Otey, C.R., et al., *Fluctuational electrodynamics calculations of near-field heat transfer in non-planar geometries: A brief overview.* Journal of Quantitative Spectroscopy and Radiative Transfer. **132**, 3-11, (2014).
[128] Cataldo, G., et al., *Infrared dielectric properties of low-stress silicon nitride.* Optics Letters. **37**, 4200-4202, (2012).
[129] Reid, M.H. and S.G. Johnson, *Efficient computation of power, force, and torque in BEM scattering calculations.* IEEE Transacions on Antennas and Propagation. **63**, 3588-3598, (2015).
[130] Goody, R.M. and Y.L. Yung, *Atmospheric radiation : theoretical basis*. 2nd ed., xiii, 519 p. (New York: Oxford University Press, 1989).
[131] Draine, B. and J.C. Weingartner, *Radiative torques on interstellar grains: I. Superthermal spinup.* Astrophysical Journal. **470**, 551-565, (1996).
[132] Sultan, R., et al., *Thermal conductivity of micromachined low-stress silicon-nitride beams from 77 to 325 K.* Journal of Applied Physics. **105**, 043501, (2009).
[133] Lee, S.-M. and D.G. Cahill, *Heat transport in thin dielectric films.* Journal of Applied Physics. **81**, 2590-2595, (1997).
[134] Kennard, E.H., *Kinetic theory of gases, with an introduction to statistical mechanics*. 1st ed. International series in physics. xiii, 483 p. (New York, London,: McGraw-Hill Book Company, inc., 1938).
[135] Horowitz, P. and W. Hill, *The art of electronics*. Vol. 2 Cambridge university press Cambridge, 1989).
[136] Li, N., et al., *Colloquium: Phononics: Manipulating heat flow with electronic analogs and beyond.* Reviews of Modern Physics. **84**, 1045-1066, (2012).

[137] Van Zwol, P., L. Ranno, and J. Chevrier, *Tuning near field radiative heat flux through surface excitations with a metal insulator transition.* Physical Review Letters. **108**, 234301, (2012).
[138] Fiorino, A., et al., *A thermal diode based on nanoscale thermal radiation.* ACS Nano. **12**, 5774-5779, (2018).
[139] Ben-Abdallah, P., S.-A. Biehs, and K. Joulain, *Many-body radiative heat transfer theory.* Physical Review Letters. **107**, 114301, (2011).
[140] Zheng, Z. and Y. Xuan, *Enhancement or suppression of the near-field radiative heat transfer between two materials.* Nanoscale and Microscale Thermophysical Engineering. **15**, 237-251, (2011).
[141] Messina, R., M. Antezza, and P. Ben-Abdallah, *Three-body amplification of photon heat tunneling.* Physical Review Letters. **109**, 244302, (2012).
[142] Nikbakht, M., *Radiative heat transfer in anisotropic many-body systems: Tuning and enhancement.* Journal of Applied Physics. **116**, 094307, (2014).
[143] De Wilde, Y., et al., *Thermal radiation scanning tunnelling microscopy.* Nature. **444**, 740-743, (2006).
[144] Biehs, S.-A., et al., *Spheroidal nanoparticles as thermal near-field sensors.* Journal of Applied Physics. **108**, 014312, (2010).
[145] Jones, A.C. and M.B. Raschke, *Thermal infrared near-field spectroscopy.* Nano Letters. **12**, 1475-1481, (2012).
[146] Basu, S., Z. Zhang, and C. Fu, *Review of near-field thermal radiation and its application to energy conversion.* International Journal of Energy Research. **33**, 1203-1232, (2009).
[147] Haus, H.A., *Waves and fields in optoelectronics*. (Englewood Cliffs, NJ: Prentice-Hall, 1984).
[148] Yu, R., A. Manjavacas, and F.J.G. de Abajo, *Ultrafast radiative heat transfer.* Nature Communications. **8**, 1-12, (2017).
[149] Ilic, O., et al., *Near-field thermal radiation transfer controlled by plasmons in graphene.* Physical Review B. **85**, 155422, (2012).
[150] Liu, X.L. and Z.M. Zhang, *Graphene-assisted near-field radiataive heat transfer between corrugated polar materials.* Applied Physics Letters. **104**, 251911, (2014).
[151] Ekeroth, R.M.A., A. Garcia-Martin, and J.C. Cuevas, *Thermal discrete dipole approximation for the description of thermal emission and radiative heat transfer of magneto-optical systems.* Physical Review B. **95**, 235428, (2017).
[152] Parker, C.B., J.-P. Maria, and A.I. Kingon, *Temperature and thickness dependent permittivity of (Ba, Sr)TiO_3 thin films.* Applied Physics Letters. **81**, 340, (2002).
[153] Zhang, G., et al., *Quantum size effects on dielectric constants and optical absorption of ultrathin silicon films.* IEEE Electron Device Letters. **29**, 1302-1305, (2008).
[154] Tian, M., M. Li, and J.C. Li, *Effect of size on dielectric constant for low dimension materials.* Physica B. **406**, 541-544, (2011).
[155] Laref, S., et al., *Size-dependent permittivity and intrinsic optical anisotropy of nanometric gold thin films: a density funcional theory study.* Optics Express. **21**, 11827-11838, (2013).
[156] Starkov, I.A. and A.S. Starkov, *The thickness dependence of dielectric permittivity in thin films.* Journal of Physics: Conference Series. **741**, 012004, (2016).
[157] Smith, B.C., *Fundamentals of Fourier transform infrared spectroscopy*. 2nd ed. (Boca Raton: CRC Press, 2011).

[158] Chiloyan, V., et al., *Transition from near-field thermal radiation to phonon heat conduction at sub-nanometer gaps.* Nature Communications. **6**, 6755, (2015).
[159] Goodson, K.E. and M. Asheghi, *Near-field optical thermometry.* Microscale Thermophysical Engineering. **1**, 225-235, (2010).
[160] Kucsko, G., et al., *Nanometre-scale thermometry in a living cell.* Nature. **500**, 54-58, (2013).
[161] Toyli, D.M., et al., *Flourescence thermometry enhanced by the quantum coherence of single spins in diamond.* Proceedings of the National Academy of Sciences. **110**, 8417-8421, (2013).
[162] Weng, W., et al., *Nano-kelvin thermometry and temperature control: Beyond the thermal noise limit.* Physical Review Letters. **112**, 160801, (2014).
[163] Xu, H., et al., *Ultra-sensitive chip-based photonic temperature sensor using ring resonator structures.* Optics Express. **22**, 3098-3104, (2014).
[164] Kim, K., et al., *Ultra-high vacuum scanning thermal microscopy for nanometer resolution quantitative thermometry* ACS Nano. **6**, 4248-4257, (2012).
[165] Gomes, S., A. Assy, and P.O. Chapuis, *Scanning thermal microscopy: A review.* physica status solidi (a). **212**, 477-494, (2015).
[166] Jeong, W., et al., *Scanning probe microscopy for thermal transport measurements.* Nanoscale and Microscale Thermophysical Engineering. **19**, 279-302, (2015).
[167] Inoue, T., et al., *Realization of dynamic thermal emission control.* Nature materials. **13**, 928, (2014).
[168] Amick, H., et al. *Evolving criteria for research facilities: I-Vibration.* in *SPIE Conference 5933: Buildings for Nanoscale Research and Beyond*. San Diego, CA. (2005).
[169] Palik, E.D., *Handbook of optical constants of solids*. Academic Press, 1985).
[170] Ordal, M.A., et al., *Optical properties of the metals Al, Co, Cu, Au, Fe, Pb, Ni, Pd, Pt, Ag, Ti, and W in the infrared and far infrared.* Applied Optics. **22**, 1099-1119, (1983).
[171] Basu, S., J. Lee, and Z.M. Zhang, *Near-field radiation calculated with an improved dielectric function model for doped silicon.* Journal of Heat Transfer. **132**, 023302, (2009).
[172] Derjaguin, B.V., I.I. Abrikosova, and E.M. Lifshitz, *Direct measurement of molecular attraction between solids separated by a narrow gap.* Quarterly Reviews Chemical Society. **10**, 295-329, (1956).
[173] Bergman, T.L. and A. Lavine, *Fundamentals of heat and mass transfer*. 8th edition / ed., pages cm (Hoboken, NJ: John Wiley & Sons, Inc., 2017).
[174] Rakić, A.D., et al., *Optical properties of metallic films for vertical-cavity optoelectronic devices.* Applied Optics. **37**, 5271-5283, (1998).
[175] Sasihithlu, K. and A. Narayanaswamy, *Proximity effects in radiative heat transfer*. Physical Review B. **83**, 161406, (2011).